

Determination of Carbon Monoxide Mass Transfer Coefficient in Different Liquid Phases using Hybrid Optimization Strategy

by

FABIANA MARIA BASTOS COELHO

A dissertation submitted to the Engineering of Chemical and Biochemical Processes Programme (EPQB), Escola de Química, Universidade Federal do Rio de Janeiro in partial fulfilment of the requirements for the degree of MASTER OF SCIENCE (M.Sc.)

Advisors:

Priscilla Filomena Fonseca Amaral, D.Sc.

Tatiana Felix Ferreira, D.Sc.

Rio de Janeiro

March 2018

Determination of Carbon Monoxide Mass Transfer Coefficient in Different Liquid Phases using Hybrid Optimization Strategy

Fabiana Maria Bastos Coelho

A dissertation submitted to the Technology of Chemical and Biochemical Processes Programme (TPQB), Escola de Química, Universidade Federal do Rio de Janeiro in partial fulfilment of the requirements for the degree of MASTER OF SCIENCE (M.Sc)

Approval:

Prof. Andréa Medeiros Salgado, D.Sc

Prof. Argimiro Resende Secchi, D.Sc

Advisors:

Prof. Priscilla Filomena Fonseca Amaral, D.Sc.

Prof. Tatiana Felix Ferreira, D.Sc.

Rio de Janeiro, RJ – Brasil

March 2018

CIP - Catalogação na Publicação

CC672d Coelho, Fabiana Maria Bastos
Determination of Carbon Monoxide Mass Transfer
Coefficient in Different Liquid Phases using Hybrid
Optimization Strategy / Fabiana Maria Bastos
Coelho. -- Rio de Janeiro, 2018.
145 f.

Orientadora: Priscilla Filomena Fonseca Amaral.
Coorientadora: Tatiana Felix Ferreira.
Dissertação (mestrado) - Universidade Federal do
Rio de Janeiro, Escola de Química, Programa de Pós
Graduação em Engenharia de Processos Químicos e
Bioquímicos, 2018.

1. overall volumetric mass transfer coefficient.
2. myoglobin bioassay. 3. Perfluorodecalin. 4.
maximum likelihood estimation. 5. particle swarm
optimization. . I. Amaral, Priscilla Filomena
Fonseca, orient. II. Ferreira, Tatiana Felix,
coorient. III. Título.

Elaborado pelo Sistema de Geração Automática da UFRJ com os dados
fornecidos pelo(a) autor(a).

To José Álvaro Alves Penin, who was always supportive about my studies and my passion for wine and whisky.

To Alanna Botelho, my sister in science. Because, without you, this dissertation would not be possible and I would still be stuck in a black hole.

“There is no such thing as being cowardly in a fight”

“Humankind cannot gain anything without first giving something in return. To obtain, something of equal value must be lost. That is alchemy’s first law of Equivalent Exchange.”

Hagane no renkinjutsushi (Fullmetal Alchemist) – Hiromu Arakawa

“Do the scary thing first, and get scared later.”

Lemony Snicket, When Did You See Her Last?

ACKNOWLEDGEMENTS

“No man is an island, entire of itself; every man is a piece of the continent, a part of the main.”

John Donne, No Man is an Island

To my parents, Fernando and Fatima, and my beloved soul, Felipe. We share our victories and failure. You taught me that we are stronger because we have each other; that we have to look back and feel proud because we always fight our way out of anything.

To my love, Otávio, who supported many of my craziest ideas and gave me more insane ideas to deliver a work I'll forever be proud. Thank you for guiding me in overcoming my fears, being my partner in crime and sharing our stories. *Because love is the best thing we do.*

To my future-in-laws, Janne and Francisco. You taught me so much, especially how to work hard and play hard.

To my family, for always being supportive of my crazy plans and excusing my absence in many important times.

To my dearest Carolina and Cecilia, thank you for letting me grow old and not-so-wise within your loyal friendship.

To Mariana, Isis, Sarah, Rose, Rebeca and Juliana, the most improbable friendship in the most unlikely context. Obviously it resulted in the funniest stories and love.

To Tamires and Alanna, who reached a hand during the darkest hours and kept me on check, reminding who I was and where I wanted to go. Alanna, thank you for the academic and operational support through months of experimental data gathering and for believing in this crazy plan. I could not ask for a better partner, Pinky!

To Vanessa, for your friendship, believing in me, your sweet smile and Magic kingdom (our game!).

To Malú, a very pleasant surprise. Thank you for helping out during experimental data gathering. I hope you keep this thirst for knowledge and kindness because this is a recipe for success.

To my lab co-workers Deja, Fabiane, Carol, Carol Benevenuti, Adrian, Jully, Karine, Marcus, Mariel, Jonas, Luana. I can close my eyes and hear you laughing, this is the ultimate work environment. Thank you for your support.

To my lab co-workers from next door Mariana, Ariane, Veronica, Julio, Larissa, Nathália, Andressa, Bernardo, Caê, Eliane, Felipe, Fernanda, Rose. You kept your arms open for me and helped me. Thank you for your support.

To Nancy, thank you for the reinvigorating coffee. My long hours would never be possible without that 8-am (onward) sip.

To Maria Alice and Mariana for giving me my first opportunity. That interview changed my life in so many ways I'll forever be grateful.

To Roberta, for bringing me back to BIOSE, checking up on me when I was abroad and for being my friend even after we parted ways.

To my advisors and friends: Tatiana Felix Ferreira and Priscilla Filomena Fonseca Amaral. You are an inspiration to me. Thank you for believing in me even when I thought this was not going to work out. You gave me your approval to conduct this project as I thought would be better and trusted my instincts throughout the process. I am really proud to say I have worked with the best.

TABLE OF CONTENTS

ABSTRACT.....	i
NOMENCLATURE	ii
LIST OF TABLES	viii
LIST OF FIGURES	xi
Chapter I – INTRODUCTION	1
Chapter II – OBJECTIVES.....	4
Chapter III – LITERATURE REVIEW	5
III.1 – Project Overview and Background	5
III.2 – Perfluorocarbons (PFC) and Tween® 80.....	7
III.2.1 – Perfluorocarbons	7
III.2.2 – Tween® 80	9
III.3 –Stirred Tank Reactor Fundamentals.....	10
III.3.1 – Impeller design	11
III.3.2 – Power measurements.....	17
III.4 – Gas-Liquid Mass Transfer.....	19
III.5 – Parameter Estimation	26
III.5.1 – Defining an objective function	27
III.5.2 – Defining an optimization strategy	28
III.5.3 – Statistical interpretation of estimated values.....	31

Chapter IV – MATERIALS AND METHODS.....	37
IV.1 – Equipment and Software.....	37
IV.2 – Reagents and Solvents	38
IV.3 – Experimental Conditions	38
IV.3.1 – Reynolds and Froude numbers.....	40
IV.4 – Myoglobin Bioassay Technique	41
IV.4.1 – Phosphate buffer solution (0.1 M, pH 7.0).....	42
IV.4.2 – Myoglobin solution	42
IV.4.3 – Test solution.....	44
IV.4.4 – Reference solution and spectra.....	44
IV.4.5 – Sampling and sample spectra.....	45
IV.3.5 – Dissolved carbon monoxide concentration	47
IV.5 – Overall Volumetric Mass Transfer Coefficient (k_{La})	47
Chapter V. RESULTS AND DISCUSSION	53
V.1 – The Myoglobin-Protein Bioassay.....	53
V.2 – Pure Distilled Water Liquid Phase in k_{La} and $CCOs$ Estimation.....	56
V.3 – PFC Influence in Distilled Water for k_{La} and $CCOs$ Estimation	62
V.4 – Tween® 80 Influence in k_{La} and $CCOs$ Estimation for Mixtures with Distilled Water, and Distilled Water and PFC.....	64
V.5 – Statistical Analysis of Estimated Values.....	68

CONCLUSION.....	76
RECOMMENDATIONS FOR FUTURE RESEARCH.....	77
REFERENCES	78
APPENDIX.....	92
A.1 – Pure distilled water at 25 °C, 100 rpm and 0.7 vvm.....	92
A.2 – Pure distilled water at 25 °C, 100 rpm and 1.3 vvm.....	93
A.3 – Pure distilled water at 25 °C, 100 rpm and 2.7 vvm.....	94
A.4 – Pure distilled water at 25 °C, 300 rpm and 0.7 vvm.....	95
A.5 – Pure distilled water at 25 °C, 300 rpm and 1.3 vvm.....	96
A.6 – Pure distilled water at 25 °C, 300 rpm and 2.7 vvm.....	97
A.7 – Pure distilled water at 25 °C, 500 rpm and 0.7 vvm.....	98
A.8 – Pure distilled water at 25°C, 500 rpm and 1.3 vvm.....	99
A.9 – Pure distilled water at 25°C, 500 rpm and 2.0 vvm.....	100
A.10 – Pure distilled water at 25°C, 500 rpm and 2.5 vvm.....	101
A.11 – Pure distilled water at 25°C, 500 rpm and 2.7 vvm – triplicate.....	102
A.12 – Pure distilled water at 25°C, 500 rpm and 2.7 vvm – duplicate	103
A.13 – Pure distilled water at 37 °C, 300 rpm and 2.7 vvm.....	104
A.14 – Pure distilled water at 37°C, 500 rpm and 2.7 vvm.....	105
A.15 – Distilled water and PFC mixture at 25°C, 500 rpm and 2.0 vvm.....	106
A.16 – Distilled water and PFC mixture at 25°C, 500 rpm and 2.5 vvm.....	107

A.17 – Distilled water and PFC mixture at 25°C, 500 rpm and 2.7 vvm	108
A.18 – Distilled water and PFC mixture at 25°C, 300 rpm and 2.7 vvm	109
A.19 – Distilled water and Tween® 80 mixture at 25°C, 500 rpm and 2.0 vvm	110
A.20 – Distilled water and Tween® 80 mixture at 25°C, 500 rpm and 2.5 vvm	111
A.21 – Distilled water and Tween® 80 mixture at 25°C, 500 rpm and 2.7 vvm	112
A.22 – Distilled water and Tween® 80 mixture at 25°C, 300 rpm and 2.7 vvm	113
A.23 – Distilled water, PFC and Tween® 80 mixture at 25°C, 500 rpm and 2.0 vvm	114
A.24 – Distilled water, PFC and Tween® 80 mixture at 25°C, 500 rpm and 2.5 vvm	115
A.25 – Distilled water, PFC and Tween® 80 mixture at 25°C, 500 rpm and 2.7 vvm	116
A.26 – Distilled water, PFC and Tween® 80 mixture at 25°C, 300 rpm and 2.7 vvm	117

ABSTRACT

Coelho, Fabiana Maria Bastos. Determination of Carbon Monoxide Mass Transfer Coefficient in Different Liquid Phases using Hybrid Optimization Strategy. Rio de Janeiro, 2018. Dissertation (Master of Science) – Engineering of Chemical and Biochemical Processes Programme, Escola de Química, Universidade Federal do Rio de Janeiro, 2018.

Synthesis gas fermentation has been proposed in literature to decrease urban solid waste environmental impact. However, the low gas-liquid mass transfer is one of the major bottlenecks of this process. Therefore, the present work aimed to evaluate the overall volumetric mass transfer (k_{LA}) in a Stirred Tank Reactor using different compositions of liquid phases. Due to the absence of probes to determine carbon monoxide (CO) concentration in liquid phase and gas chromatography cost, a myoglobin bioassay technique was executed. k_{LA} was estimated using a hybrid optimization method (Particle Swarm Optimization - PSO, and Sequential Quadratic Programming – SQP) and Maximum Likelihood Estimation (MLE) as objective function. Pure CO (99.5%) was fed into a reactor filled with 0.75 and 1.0 L of liquid mixture. Three agitation speeds and five specific gas flow rates were tested. Four different liquid mixtures were analysed: pure distilled water; distilled water and 20% perfluorodecalin (PFC); distilled water and 0.15% Tween® 80; and distilled water, 20% PFC and 0.15% Tween® 80. A k_{LA} of 603.49 h⁻¹ in distilled water, PFC and Tween® 80 at 500 rpm and 2.7 min⁻¹. The highest k_{LA} for pure distilled water reported so far was achieved in the present work: 399.06 h⁻¹ at 500 rpm and 2.7 min⁻¹. Therefore, hybrid optimization was successfully performed and k_{LA} results were comparable to literature. PFC and Tween® 80 increased CO dispersion in the liquid phase, increasing mass transfer.

Keywords: synthesis gas; overall volumetric mass transfer coefficient; perfluorodecalin; Tween® 80; myoglobin bioassay; maximum likelihood estimation; particle swarm optimization.

NOMENCLATURE

Abbreviations

ABRELPE	Associação Brasileira de Limpeza Pública e Resíduos Especiais
BCR	Bubble Column Reactor
CHF	Composite Hollow Fiber Membrane
CSTR	Continuous Stirred Tank Reactor
FIM	Fisher's Information Matrix
GA	Genetic Algorithm
GLR	Gas-Lift Reactor
HFMBR	Hollow Fiber Membrane Bioreactor
ISMA	International Solid Waste Association
Mb	Myoglobin
MBR	Membrane Bioreactor
MLE	Maximum Likelihood Estimation
n/a	Not applicable
PBC	Packed Bubble Column
PFC	Perfluorocarbon; perfluorodecalin
PS	Polystyrene
PSO	Particle Swarm Optimization
SA	Simulated Annealing

SBR		Sulfate-reducing bacteria
SQP		Sequential Quadratic Programming
STR		Stirred Tank Bioreactor
TBR		Trickle Bed Reactor
vvm		Volume of gas in volume of media
“deoxi” spectrum		Spectrum obtained for myoglobin in spectrophotometer at a wavelength range of 400-700 nm
“carboxi” spectrum		Spectrum obtained for carbon monoxide (CO) in spectrophotometer at a wavelength range of 400-700 nm
“oxi” spectrum		Spectrum obtained for oxygen (O ₂) in spectrophotometer at a wavelength range of 400-700 nm
“oxiTS” spectrum		Spectrum obtained for oxygen (O ₂) in spectrophotometer at a wavelength range of 400-700 nm, using the test solution
Roman symbols		
Abs		Absorbance at spectra maximum peak
c ₁		Cognition parameter
c ₂		Social parameter
C _{CO}	μM	Carbon monoxide concentration in liquid phase
C _{CO} ^S	μM	Steady-state carbon monoxide concentration
CI		Confidence interval
C _p	μM	Myoglobin concentration

d		Search direction or numbers of parameters
D_i	m	Impeller diameter
DR		Dilution ratio
DF		Degrees of freedom
F		Superior limit at Fisher's distribution given NP and (NE·NY-NP) degrees of freedom considering a confidence level of (1- α).
F_{CO}	L/min	Gas flow rate
F_{Obj}		Objective function
$F_{Obj}(\theta)$		Objective function at parameter θ
Fr		Froude number
F_w	mL/min	Liquid recirculation flow rate
g	m/s^2	Gravitational acceleration
H_i	m	Impeller distance from vessel bottom
H_L	m	Liquid height in vessel
IC	m	Impeller clearance
k		Iteration number
k_G		Mass transfer coefficient at the gaseous stagnant film
k_L		Mass transfer coefficient at the liquid stagnant film
k_{La}	h^{-1}	Overall Volumetric mass transfer coefficient
$\min(F_{Obj}(\theta))$		Objective function at the minimum

N	<i>rpm</i>	Impeller speed
NA		Number of assays
NE		Number of Experiments
N _{iter}		Number of iterations
NP		Number of parameters
N _p		Gassed power number
N _{po}		Ungassed power number
NQ		Agitator flow number
NX		Total number of independent variables
NY		Number of dependent variables
p or N _p		Number of particles
P	<i>W</i>	Impeller power input into the liquid when gas is sparged in the tank
P _o	<i>W</i>	Impeller power input into liquid without sparged gas
Q _{CO}	<i>min⁻¹</i>	Specific gas flow rate
Q _L	<i>L/min</i>	Gas volumetric flow
r ₁ and r ₂		Random numbers with uniform distribution in the range [0,1]
Re		Reynolds number
SS		Percentage of steady-state concentration
t		Probability using t-student distribution for a certain degree of freedom and confidence level

t	s	Sampling time
T	m	Tank diameter
V		Velocity/pseudo velocity
V_{Mb}	μl	Volume of myoglobin solution added to cuvette
V_B	ml	Volume of buffer added to cuvette
V_S	μl	Sample volume in the cuvette ($10 \mu l$)
V_T	μl	Total volume in the cuvette
V_X		Covariance matrix
V_θ		Parameter covariance matrix
w		Inertial weight
w_i	m	Impeller width
X		Independent variable
x		Particle's position
X_{glo}		Search space where F_{Obj} reaches an optimum value for the whole swarm
X_{ind}		Search space where F_{Obj} reaches an optimum value for each particle
Y_e or y_{eij}		Experimental values matrix for NE experiments and NY measurements
y_e		Experimental value for dependent variable

\mathbf{Y}_m or y_{mij}		Predicted values matrix for NE experiments and NY measurements
y_m		Predicted value for dependent variable
Greek symbols		
α	%	Confidence level
ε_m	$(\mu M.cm)^{-1}$	Molar attenuation coefficient
θ		Parameter
θ'_i		Parameter estimated value
θ_h		Upper bound parameter vector
θ_l		Lower bound parameter vector
λ	cm	Cuvette optical path
μ	$N.s/m^2$	Dynamic viscosity
μ_x		Mean value for variable x; sample mean
ν_{xi}		Variance for x_i
ν_{xj}		Variance for x_j
ρ	kg/m^3	Fluid density
$\sigma_{y_{i,j}}^2$		Experimental variance
σ_{θ_i}		Parameter standard deviation
$\sigma_{k_L a} / k_L a$		$k_L a$ relative variance
$\sigma_{C_{CO}^s} / C_{CO}^s$		C_{CO}^s relative variance

LIST OF TABLES

Tables in Chapter III

Table III.1 Carbon monoxide overall volumetric mass transfer coefficient for different reactors and hydrodynamics.	23
---	----

Tables in Chapter IV

Table IV.1 Experimental conditions for overall volumetric mass transfer coefficient estimation.	39
Table IV.2 Upper and Lower Bound limits for optimization based on operational conditions, liquid phase and temperature (T, °C).....	49

Tables in Chapter V

Table V.1 Results of Re, Fr, k_{LA} , $CCOs$, and its confidence intervals (CI) obtained at different agitation speed (N) and specific gas flow rate (Q_{CO}) for carbon monoxide in 0.75 L of pure distilled water at 25 °C and 65.26 mL/min recirculated liquid flow.....	57
Table V.2 Results of Re, Fr, k_{LA} , $CCOs$, and its confidence intervals (CI) obtained at different specific gas flow rate (Q_{CO}) for carbon monoxide in 1.0 L of pure distilled water at 25 °C, 500 rpm and 65.26 mL/min recirculated liquid flow.	60
Table V.3 Results of Re, Fr, k_{LA} , $CCOs$, and its confidence interval (CI) obtained at different agitation speed (N) for carbon monoxide in 0.75 L of pure distilled water at 37 °C, 2.7 vvm specific gas flow rate and 65.26 mL/min recirculated liquid flow.....	61
Table V.4 Results of k_{LA} , $CCOs$ and its confidence interval (CI) obtained for different reactor volume (V), agitation speed (N) and specific gas flow rate (Q_{CO}) for carbon monoxide in a liquid mixture distilled water and PFC at 25 °C and 65.26 mL/min recirculated liquid flow.	63

Table V.5 Results of k_{LA} , $CCOs$ and its confidence interval (CI) obtained at different reactor volume (V), agitation speed (N) and specific gas flow rate (Q_{CO}) for carbon monoxide in a mixture of distilled water and Tween® 80 at 25 °C and 65.26 mL/min recirculated liquid flow..... 65

Table V.6 Results of k_{LA} , $CCOs$ and its confidence interval (CI) obtained at different reactor volume (V), agitation speed (N) and specific gas flow rate (Q_{CO}) for carbon monoxide in a liquid mixture composed of distilled water, PFC and Tween® 80 liquid mixture at 25 °C and 65.26 mL/min recirculated liquid flow, 67

Table V.7 Results of k_{LA} and $CCOs$ alongside its confidence intervals, parametric correlation and objective function values at different agitation speed (N) and specific gas flow rate (Q_{CO}) for carbon monoxide in 0.75 L and 1.0 L of pure distilled water at 25 °C and 65.26 mL/min recirculated liquid flow. 69

Table V.8 Results of k_{LA} and $CCOs$ alongside its confidence intervals, parametric correlation and objective function values at different agitation speed (N) for carbon monoxide in 0.75 L pure distilled water at 37 °C, 2.7 vvm specific gas flow rate and 65.26 mL/min recirculated liquid flow. 70

Table V.9 Results of k_{LA} and $CCOs$ alongside its confidence intervals, parametric correlation and objective function values at different agitation speed (N) and specific gas flow rate (Q_{CO}) for carbon monoxide in liquid mixture composed of distilled water and PFC at 25 °C and 65.26 mL/min recirculated liquid flow. 70

Table V.10 Results of k_{LA} and $CCOs$ alongside its confidence intervals, as well as parametric correlation and objective function values at different agitation speed (N) and specific gas flow rate (Q_{CO}) for carbon monoxide in a liquid mixture composed of distilled water and Tween® 80 at 25 °C and 65.26 mL/min recirculated liquid flow. 71

Table V.11 Results of k_{La} and $CCOs$ alongside its confidence intervals, as well as parametric correlation and objective function values at different agitation speed (N) and specific gas flow rate (Q_{Co}) for carbon monoxide in a liquid mixture composed of distilled water, PFC and Tween® 80 at 25 °C and 65.26 mL/min recirculated liquid flow..... 71

Table V.12 Comparison between experiments conducted in triplicate and duplicate for pure distilled water at 500 rpm and 2.7 vvm..... 72

LIST OF FIGURES

Figures in Chapter III

Figure III.1 Perfluorodecalin structure (SIGMA-ALDRICH).....	7
Figure III.2 Polysorbate 80 (Tween® 80) structure, where sum of w, x, y and z has to be 20 (SIGMA-ALDRICH).....	9
Figure III.3 Cavity formation in a radial flow impeller at constant agitation speed but gas flow rate increase; where (i), (ii) and (iii) represent the vortex, clinging and large cavities, respectively (adapted from WARMOESKERKEN et al., 1984).	12
Figure III.4 Radial flow impeller scheme forming a ‘3-3’ structure with 3 clinging and 3 large cavities (a) and with large cavities (b).	13
Figure III.5 Bulk flow regimes for a single radial flow impeller in a gas-liquid system (adapted from KADIC and HEINDEL, 2014).....	14
Figure III.6 Schematic Stirred Tank Bioreactor representing tank diameter (T), liquid height in vessel (H_L), impeller speed (N), impeller width (w_i), distance from the tank bottom (H_i), impeller diameter (D_i) and clearance between top and bottom impellers (ID).	15
Figure III.7 Illustration of gas route to micro-organism presenting all eight mass transfer resistances, where A is the gas bubble, B is the gas-liquid interface, C are the stagnant films, D is the cell and E is the site of the biochemical reaction. Numbers 1 to 8 represent the resistances. Adapted from BORZANI et al. (2001).	20
Figure III.8 Parametric uncertainty shapes for a linear model, showing parametric correlation between parameters θ_1 and θ_2 . Region A represents a confidence interval; B represents an ellipsoid confidence region; and C a steep ellipsoid confidence region (adapted from ALBERTON, 2013).	36

Figures in Chapter IV

Figure IV.1 “Oxi” spectrum scanned using spectrophotometer at 400-700 nm wavelength.....	43
Figure IV.2 Reference or base-spectra used in the present work: deoxi (Mb), oxi (MbO ₂), and carboxi (MbCO).....	45
Figure IV.3 Equipment set-up used during mass transfer coefficient determination, representing sampling port, and recirculation line and gas inlet.	46
Figure IV.4 Sample and reference spectra obtained in spectrophotometer to determine dissolved carbon monoxide concentration.....	46

Figures in Chapter V

Figure V.1 Difference between two myoglobin-oxygen spectra: “oxi” (A) and “oxiTS” (B).	55
Figure V.2 Model prediction for pure distilled water at 25 °C, 100 rpm and 1.3 vvm.	59
Figure V.3 Water, PFC and Tween® 80 emulsion prepared with ULTRA-TURRAX® (left) and in the STR (right).	66
Figure V.4 Model prediction for pure distilled water at 500 rpm and 2.7 vvm performed in triplicate (A) and duplicate (B).◇ represents the experimental data and * represents the sample mean.....	72
Figure V.5 Likelihood regions ($\alpha = 90\%$) for pure distilled water 500 rpm and 2.7 vvm performed in triplicate (A) and duplicate (B).....	74
Figure V.6 Likelihood region ($\alpha = 90\%$) for pure distilled water at 500 rpm and 0.7 vvm.	75
Figure V.7 Model prediction (A) and likelihood region ($\alpha=90\%$), (B) for distilled water, PFC and Tween® 80 mixture at 500 rpm and 2.7 vvm.◇ represents the experimental data and * represents the sample mean.....	75

Figures in Appendix

Figure A.1 Model prediction for pure distilled water at 25 °C, 100 rpm and 0.7 vvm.	92
--	----

Figure A.2 Confidence region ($\alpha=90\%$) for pure distilled water at 25 °C, 100 rpm and 0.7 vvm.	92
Figure A.3 Model prediction for pure distilled water at 25 °C, 100 rpm and 1.3 vvm.	93
Figure A.4 Confidence region ($\alpha=90\%$) for pure distilled water at 25 °C, 100 rpm and 1.3 vvm.	93
Figure A.5 Model prediction for pure distilled water at 25 °C, 100 rpm and 2.7 vvm.	94
Figure A.6 Confidence region ($\alpha=90\%$) for pure distilled water at 25 °C, 100 rpm and 2.7 vvm.	94
Figure A.7 Model prediction for pure distilled water at 25 °C, 300 rpm and 0.7 vvm.	95
Figure A.8 Confidence region ($\alpha=90\%$) for pure distilled water at 25 °C, 300 rpm and 0.7 vvm.	95
Figure A.9 Experimental data for pure distilled water at 25 °C, 300 rpm and 1.3 vvm.	96
Figure A.10 Confidence region ($\alpha=90\%$) for pure distilled water at 25 °C, 300 rpm and 1.3 vvm.	96
Figure A.11 Model prediction for pure distilled water at 25 °C, 300 rpm and 2.7 vvm.	97
Figure A.12 Confidence region ($\alpha=90\%$) for pure distilled water at 25 °C, 300 rpm and 2.7 vvm.	97
Figure A.13 Model prediction for pure distilled water at 25 °C, 500 rpm and 0.7 vvm.	98
Figure A.14 Confidence region ($\alpha=90\%$) for pure distilled water at 25 °C, 500 rpm and 0.7 vvm.	98
Figure A.15 Model prediction for pure distilled water at 25 °C, 500 rpm and 1.3 vvm.	99
Figure A.16 Confidence region ($\alpha=90\%$) for pure distilled water at 25 °C, 500 rpm and 1.3 vvm.	99

Figure A.17 Model prediction for pure distilled water at 25 °C, 500 rpm and 2.0 vvm.	100
Figure A.18 Confidence region ($\alpha=90\%$) for pure distilled water at 25 °C, 500 rpm and 2.0 vvm.	100
Figure A.19 Model prediction for pure distilled water at 25 °C, 500 rpm and 2.5 vvm.	101
Figure A.20 Confidence region ($\alpha=90\%$) for pure distilled water at 25 °C, 500 rpm and 2.5 vvm.	101
Figure A.21 Model prediction for pure distilled water at 25 °C, 100 rpm and 2.7 vvm, triplicate.	102
Figure A.22 Confidence region ($\alpha=90\%$) for pure distilled water at 25 °C, 100 rpm and 2.7 vvm, triplicate.	102
Figure A.23 Model prediction for pure distilled water at 25 °C, 100 rpm and 2.7 vvm, duplicate.	103
Figure A.24 Confidence region ($\alpha=90\%$) for pure distilled water at 25 °C, 100 rpm and 2.7 vvm, duplicate.	103
Figure A.25 Model prediction for pure distilled water at 37 °C, 300 rpm and 2.7 vvm.	104
Figure A.26 Confidence region ($\alpha=90\%$) for pure distilled water at 37 °C, 300 rpm and 2.7 vvm.	104
Figure A.27 Model prediction for pure distilled water at 37 °C, 500 rpm and 2.7 vvm.	105
Figure A.28 Confidence region ($\alpha=90\%$) for pure distilled water at 37 °C, 500 rpm and 2.7 vvm.	105
Figure A.29 Model prediction for distilled water and PFC mixture at 25 °C, 500 rpm and 2.0 vvm.	106

Figure A.30 Confidence region ($\alpha=90\%$) for distilled water and PFC mixture at 25 °C, 500 rpm and 2.0 vvm.....	106
Figure A.31 Model prediction for distilled water and PFC mixture at 25 °C, 500 rpm and 2.5 vvm.	107
Figure A.32 Confidence region ($\alpha=90\%$) for distilled water and PFC mixture at 25 °C, 500 rpm and 2.5 vvm.....	107
Figure A.33 Model prediction for distilled water and PFC mixture at 25 °C, 500 rpm and 2.7 vvm.	108
Figure A.34 Confidence region ($\alpha=90\%$) for distilled water and PFC mixture at 25 °C, 500 rpm and 2.7 vvm.....	108
Figure A.35 Model prediction for distilled water and PFC mixture at 25 °C, 300 rpm and 2.7 vvm.	109
Figure A.36 Confidence region ($\alpha=90\%$) for distilled water and PFC mixture at 25 °C, 300 rpm and 2.7 vvm.....	109
Figure A.37 Model prediction for distilled water and Tween® 80 mixture at 25 °C, 500 rpm and 2.0 vvm.	110
Figure A.38 Confidence region ($\alpha=90\%$) for distilled water and Tween® 80 mixture at 25 °C, 500 rpm and 2.0 vvm.	110
Figure A.39 Model prediction for distilled water and Tween® 80 mixture at 25 °C, 500 rpm and 2.5 vvm.	111
Figure A.40 Confidence region ($\alpha=90\%$) for distilled water and Tween® 80 mixture at 25 °C, 500 rpm and 2.5 vvm.	111

Figure A.41 Model prediction for distilled water and Tween® 80 mixture at 25 °C, 500 rpm and 2.7 vvm.	112
Figure A.42 Confidence region ($\alpha=90\%$) for distilled water and Tween® 80 mixture at 25 °C, 500 rpm and 2.7 vvm.	112
Figure A.43 Model prediction for distilled water and Tween® 80 mixture at 25 °C, 300 rpm and 2.7 vvm.	113
Figure A.44 Confidence region ($\alpha=90\%$) for distilled water and Tween® 80 mixture at 25 °C, 300 rpm and 2.7 vvm.	113
Figure A.45 Model prediction for distilled water, PFC and Tween® 80 mixture at 25 °C, 500 rpm and 2.0 vvm.....	114
Figure A.46 Confidence region ($\alpha=90\%$) for distilled water, PFC and Tween® 80 mixture at 25 °C, 500 rpm and 2.0 vvm.	114
Figure A.47 Model prediction for distilled water, PFC and Tween® 80 mixture at 25 °C, 500 rpm and 2.5 vvm.....	115
Figure A.48 Confidence region ($\alpha=90\%$) for distilled water, PFC and Tween® 80 mixture at 25 °C, 500 rpm and 2.5 vvm.	115
Figure A.49 Model prediction for distilled water, PFC and Tween® 80 mixture at 25 °C, 500 rpm and 2.7 vvm.....	116
Figure A.50 Confidence region ($\alpha=90\%$) for distilled water, PFC and Tween® 80 mixture at 25 °C, 500 rpm and 2.7 vvm.	116
Figure A.51 Model prediction for distilled water, PFC and Tween® 80 mixture at 25 °C, 300 rpm and 2.7 vvm.....	117

Figure A.52 Confidence region ($\alpha=90\%$) for distilled water, PFC and Tween® 80 mixture at 25 °C, 300 rpm and 2.7 vvm. 117

Chapter I – INTRODUCTION

Fermentation is a very complex process in biotechnological industry. It can be described as a bioreaction in which components (substrate and nutrients) are converted biologically using a biological catalyst (microorganism) into another component (bioproducts). The process is separated in two types: aerobic fermentation, in which oxygen supply is required (mainly air since it is a cheap source); and anaerobic fermentation, which occurs in absence of oxygen. Some anaerobic fermentations present gas mixtures as substrate and carbon monoxide as carbon source (SHEN et al., 2015). Due to its importance to the field and complexity, many studies have been developed in this area, especially regarding bioreactor hydrodynamics and gas-liquid systems.

Residues are an interesting and cheap source of nutrients that can be converted to biofuels and biochemicals through a hybrid thermochemical-biochemical process. Industrial, urban solid waste, lignocellulosic and other residual biomass can be converted to synthesis gas through pyrolysis. Synthesis gas, also called syngas, is an important building block in chemical industry, and its composition will depend upon pyrolysis conditions. Hydrogen, carbon monoxide and carbon dioxide ratio can vary depending on particle size, moisture, ash, temperature, reactor type, biomass composition and more (MOHAMMADI et al., 2011).

The resulting gas can be fermented by some *Clostridium* bacteria, capable of converting synthesis gas into ethanol, butanol, lactic acid, acetic acid, butyric acid and other chemicals (BREDWELL et al., 1999). The resulting process is a hybrid route based in thermochemical (residue pyrolysis) and biochemical (fermentation) conversion of all components present in residual biomass (MOHAMMADI et al., 2012). Commercially, LanzaTech collaborated with Concord BlueEnergy to produce ethanol and 2,3-butanediol from the fermentation of high quality synthesis gas obtained via gasified municipal solid wastes and agricultural residues. INEOS New

Planet Bioenergy also produce ethanol from syngas obtained through the gasification of vegetative waste and agricultural biomass (SHEN et al., 2015).

However, one of the major bottlenecks in this process, especially concerning commercialization, is the mass transfer between gas and liquid phases due to the low solubility of synthesis gas (BREDWELL and WORDEN, 1998; BREDWELL et al., 1999; KLASSON et al., 1991; WORDEN and BREDWELL, 1998). The increase of gas solubility in culture media may enhance the availability of gaseous substrate to cells, improving both cell's autotrophic growth and product conversion (BREDWELL and WORDEN, 1998; VEGA et al., 1989).

Many approaches have been proposed in literature in order to increase mass transfer in gas-liquid systems, such as increasing gas and liquid flow rates, larger specific gas-liquid interfacial areas, different reactor configurations, innovative impeller designs and more (MUNASINGHE and KHANAL, 2010; MUNASINGHE and KHANAL, 2012; SHEN et al., 2014a; UNGERMAN and HEINDEL, 2007; YASIN et al., 2014). However, as far as we know, none have used liquid mixtures in order to increase CO mass transfer to liquid phase. Perfluorochemicals or perfluorocarbons (PFC) have been used in aerobic systems to increase the volumetric mass transfer of oxygen into liquid phase, without damaging cells (CHO and WANG, 1988; ELIBOL and MAVITUNA, 1995).

However, as observed in the present work, the immiscibility of PFC in water can compromise the gas-liquid system and affect negatively the overall volumetric mass transfer coefficient. Due to carbon monoxide affinity to organic phase, its transfer to aqueous phase is impaired and, therefore, k_{La} values for these systems were comparatively low. Surfactant Tween® 80 was used in order to bypass this situation.

Another issue faced was the experimental uncertainty due to the bioassay method, which is extremely delicate and care must be taken in many steps during solution preparation and sampling. For that reason, this work proposes two different optimization strategies, non-deterministic (Particle Swarm Optimization – PSO) and deterministic, using Maximum Likelihood Estimation (MLE) in order to estimate carbon monoxide saturation and k_{La} , comparing both of them.

Therefore, the main goal of this work is to evaluate the overall volumetric mass transfer coefficient for carbon monoxide in a stirred tank reactor using different liquid phases compositions: pure distilled water; distilled water and 20% PFC; distilled water and 0.15% Tween® 80; and distilled water, 20% PFC and 0.15% Tween® 80; as well as different gas flow rates, agitations speeds and liquid volumes.

The present dissertation was divided in nine chapters in order to easy reading and comprehension, including this introductory chapter. The following chapter presents the main objective and aims of this work while Chapter III summarize important and base concepts in a Literature Review. Chapter IV details the methodology implemented during experimental and analysis phase, including the myoglobin bioassay method, optimization techniques and materials used. Chapter V display experimental results and discussion in order to express how the difference in the gas-liquid system affected bioreactor hydrodynamic and k_{La} . Concluding marks, recommendation for future work, and references used in the elaboration of this work are presented subsequently. Appendix assemble all plots created in MATLAB during k_{La} estimation, including CO concentration through time in all experiments (data and uncertainties), model fitting to optimized overall mass transfer coefficient and confidence regions for all experiments and levels of confidence.

Chapter II – OBJECTIVES

The main objective of this work was to estimate the overall volumetric mass transfer coefficient ($k_{L,a}$) in a multiphase stirred tank reactor using different liquid phase compositions. For that purpose, the following aims were set:

- Identify the best conditions of agitation speed, carbon monoxide flow rate and liquid phase composition regarding $k_{L,a}$ in the stirred tank bioreactor used.
- Evaluate the carbon monoxide concentration in the liquid phase by elaborating a script to transform the data obtained in spectrophotometer in mathematical values.
- Estimate overall volumetric mass transfer coefficient and carbon monoxide saturation through Maximum Likelihood in MATLAB using a hybrid optimization technique.
- Obtain likelihood confidence regions by selecting objective function values evaluated with Particle Swarm Optimization strategy.

Chapter III – LITERATURE REVIEW

III.1 – Project Overview and Background

Urban and industrial solid waste are a very complex problem for the environment. Comparing to past years, constant progress and population growth enhanced the amount of residues generated. According to ABRELPE (2016), a Brazilian representative at the International Solid Waste Association (ISWA), 78.3 million tons of urban solid waste were produced in Brazil in 2016. Although it represents a 2% decrease referring to 2015, 9% of this solid waste was improperly disposed. Moreover, 41.7 million tons were destined for sanitary landfill and 29.7 million tons were designated to controlled landfills or dumps. Also, due to Brazilian's economic crises, 5.7% less jobs were offered and 17,700 formal posts for public cleaning services were shut down. Cities had to spend approximately R\$ 2,067,696,000.00 in urban solid waste collection, which represents approximately US\$ 650 million (ABRELPE, 2016).

Urban solid waste can impact the environment and public health since it contaminates soil, water and air if not treated or disposed properly (CHERUBINI, 2010; DEVARAPALLI and ATIYEH, 2015). Moreover, collecting and disposing urban solid waste correspond to a public expenditure of \$ 650 million and part of this amount could be transformed into revenue for the government and companies. Residue thermal conversion is already a reality all over the world. In Brazil, sugar cane residues like straw and bagasse are burned to generate electric energy for biorefinery plants (CONAB, 2011). In many countries in Europe, residues are combusted in order to generate heating and electrical energy for rural and urban areas (KOKALJ and SAMEC, 2013; REDDY, 2006; WORLD ENERGY COUNCIL, 2016). In Florida, waste-to-energy plants cut landfilled waste by 90% (WORLD ENERGY COUNCIL, 2016).

Residue pyrolysis result in synthesis gas, which is a building block in chemical industry and can be converted by anaerobic bacteria into very important biochemicals and biofuels, such as ethanol, butanol, butyric acid, 2,3–butanediol, acetic acid and more (LIOU et al., 2005; LATIF et al., 2014; MOHAMMADI et al., 2011; ORGILL et al., 2013; PANTALÉON et al., 2014). This hybrid thermochemical-biochemical process, however, has a major technological drawback, which is the low mass transfer between gas and liquid phases due to gas low solubility (KLASSON et al., 1991). Therefore, much have been discussed in literature to enhance mass-transfer, such as using a hollow fiber membrane bioreactor (MUNASINGHE e KHANAL, 2012; SHEN et al., 2014; YASIN et al., 2014) and a dual-impeller stirred tank bioreactor (UNGERMAN and HEINDEL, 2007).

Synthesis gas fermentation have also other advantages in relation to well-established processes in chemical industry. This fermentation presents a higher tolerance to sulphur compounds; a higher variety of CO, H₂ and CO₂ composition in synthesis gas due to biomass composition; lower operational pressure and temperature, which decreases operational costs; and high productivity and product uniformity when compared to Fischer-Tropsch process (LATIF et al., 2014). Regarding other biotechnological conversion of lignocellulosic biomass, synthesis gas fermentation eliminates a complex pre-treatment stage, which would enhance operational cost due to enzyme acquisition. Moreover, all components of lignocellulosic biomass are converted and thermodynamic equilibrium relationships are avoided. Biomass composition does not interfere in the gas composition obtained through pyrolysis or gasification, and the resulting H₂:CO:CO₂ ratio does not affect fermentation (KLASSON et al., 1991; SHEN et al., 2014).

III.2 – Perfluorocarbons (PFC) and Tween® 80

In the present dissertation, perfluorodecalin (PFC) and Polysorbate-80 (Tween® 80) are two chemicals used to increase mass transfer in gas-liquid systems. Both have been extensively applied in industry for many purposes. PFCs were first synthesized during II World War due to its resistance to uranium based compounds (LOWE et al., 1998). Tween® 80 is a non-ionic surfactant and emulsifier often used in foods and cosmetics (GOFF, 1997; MADIC et al., 2013).

III.2.1 – Perfluorocarbons

Perfluorocarbons are molecules in which all hydrogen atoms were replaced by fluorine, resulting in molecules with higher molecular weight and density than water. The most common compound among perfluorocarbons is Perfluorodecalin, which is a cyclic alkane with 18 fluorine. Perfluorodecalin has a density of 1.908 g/cm^3 and kinematic viscosity of $2.66 \text{ mm}^2/\text{s}$ and its structure is represented in Figure III.1 (LOWE et al., 1998).

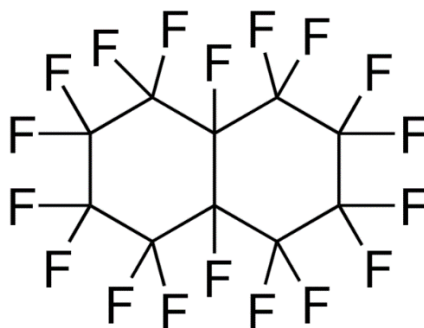


Figure III.1 Perfluorodecalin structure (SIGMA-ALDRICH).

PFCs have a high chemical and thermal stability due to carbon-fluorine strong bond. Moreover, fluorine present in the structure encompasses completely the molecule providing an electronic and steric protection. Although immiscible in aqueous systems, PFCs have been used in biotechnological processes due to its biological inertness and high gas solubility, which facilitate

respiratory-gas delivery to cells (AMARAL, 2007; AMARAL et al., 2008; LOWE, 2002). These molecules can dissolve large quantities of oxygen and carbon dioxide without chemical reactions. Also, oxygen dissociation from the PFC molecule is faster than the dissociation from hemoglobin, increasing the mass transfer coefficient (LOWE et al., 1998). The solubility is related to molar volume of dissolved gas, being carbon dioxide the most soluble gas (200 mmol.L^{-1}), followed by oxygen, carbon monoxide and nitrogen, which is the less soluble (LOWE, 2002).

The first work in the area was performed with lab rats, which were capable of “breathing” when submerged in PFC (CLARK and GOLLAN, 1966). Perfluorocarbons were responsible for enhancing oxygen uptake and mass transfer (CHO and WANG, 1988; ELIBOL, 1996; ELIBOL, 1997; ELIBOL AND MAVITUNA, 1995; JU and LEE, 1991; JUNKER et al., 1990; MCMILLAN and WANG, 1987; TURICK and BULMER, 1998; WASANASATHIAN and PENG, 2001) and increase cell density or exponential growth phase (ELIBOL, 1996; ELIBOL, 1997; JUNKER et al., 1990; WASANASATHIAN and PENG, 2001). Cho and Wang (1988) reported that PFC did not harm cells and improved overall volumetric mass transfer coefficient (k_{LA}) of oxygen.

The main advantage of using PFC in bioprocess engineering is related to gas-liquid mass transfer. It has been proved that PFCs can regulate air or oxygen intake, increasing cell growth in these systems and consequently productivity. In this way, PFC would decrease shear stress in cells due to conventional aeration and agitation (AMARAL, 2007). Moreover, PFC recoverability is commercially favourable and easy, since PFC tends to decant after reposing due to its high density and immiscibility in aqueous media. Easy recovery, re-sterilization, re-gassed and return to bioreactor makes this expensive chemical a commercially attractive one (LOWE, 2002).

III.2.2 – Tween® 80

Tween® is a commercial name for a series of non-ionic surfactants derived from polyethoxy sorbitan esters, which are mainly used as emulsifiers, defoamers, dispersants and stabilizers in food, cosmetics and biodegradation media (AYORINDE et al., 2000). Tween® 80, or polysorbate 80, is a viscous yellow liquid of density 1.06 g/cm³ and kinematic viscosity between 300 and 500 mm²/s. Its structure is represented in Figure III.2. Figure III.2 Polysorbate 80 (Tween® 80) structure, where sum of w, x, y and z has to be 20 (SIGMA-ALDRICH).

. It has a high potential in thermo-regulated ion-separation technologies and is present in ice-creams as an emulsifier to make the product smoother, easier to handle and more resistant to melting (GOFF, 1997; MADIC et al., 2003). It also acts as surfactant in soaps and cosmetics. Another non-ionic polysorbate-type surfactant used in bioprocess is Tween® 20, or polysorbate 20, which is also an emulsifier. The difference between Tween® 80 and 20 are its commercial polysorbate formulations. Tween® 20 is made with a mixture of stearic, palmitic, myristic, and lauric acids, whereas Tween® 80 is made of stearic, oleic and linoleic acids (AYORINDE et al., 2000).

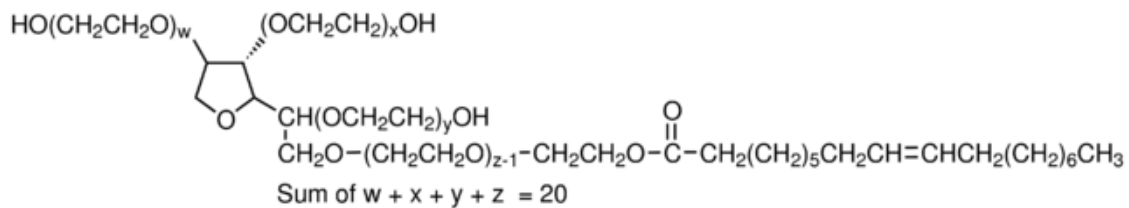


Figure III.2 Polysorbate 80 (Tween® 80) structure, where sum of w, x, y and z has to be 20 (SIGMA-ALDRICH).

Many studies, however, have been done to improve polysorbate 80 and 20 usage towards gas-liquid mass transfer due to enhanced knowledge about surface-active substances in absorption processes (BELO et al., 2011). Low concentrations of surface agents can affect gas-liquid mass transfer parameters and bioreactor hydrodynamics, such as gas holdup, bubble diameters, gas

liquid interfacial area, turbulence and more (KIM et al., 2006; LOUBIÈRE and HÉBRAND, 2004; PAINMANAKUL et al., 2005; RUZICKA et al., 2008; SARDENING et al., 2006; VASCONCELOS et al., 2003). Bredwell and Worden (1998) used Tween® 20 to measure microbubble in a dispersion reactor in order to evaluate bioreactor hydrodynamics and gas-liquid mass transfer. Belo et al. (2011) stated that Tween® 80 promoted a strong decrease in carbon dioxide mass transfer coefficient to liquid at low gas flow rate in a bubble column but increased gas holdup and bubble interfacial area.

III.3 –Stirred Tank Reactor Fundamentals

Stirred Tank Reactors or Stirred Tank Bioreactors (STR) are a standard reactor in chemical industry due to its low installation and operational costs (OLDSHUE, 1983). It is present in a variety of processes, such as fermentations, wastewater treatment and dissolution. Besides, a well-mixed state can be easily achieved, which offers substrate contact, pH and temperature controls, removal of toxic by-products, uniform cell distribution and more (HOFFMAN et al., 2008). Usually, STRs are made of stainless steel or glass. Although most STR have cylindrical shape with flat bottom, other designs are possible including conical, dished and curved bottoms (OLDSHUE, 1983).

Multiphase bioreactors are a reality in fermentation industry, although mass transfer in these systems can be complicated. According to Oldshue (1997), mixing systems for gas-liquid reactors should have two processes, dispersion and absorption. Dispersion is not a critical system constraint and will be achieved if the entire bioreactor volume is used to mix gas into the liquid (OLDSHUE, 1997). However, the adsorption process can be tough due to gas low solubility in liquid, which is the case for carbon monoxide and oxygen in water or culture media (BREDWELL

and WORDEN, 1998; BREDWELL et al., 1999; KLASSON et al., 1991; WORDEN and BREDWELL, 1998).

Concerning stirred tank flow regimes, superficial gas flow regime influences directly gas-liquid mass transfer through gas-filled cavities and gas holdup. Gas holdup is the volumetric fraction occupied by the gas phase in the total volume of a two or three phase mixture. The impeller sweeping action creates a low pressure void that is filled with sparged gas. These cavities filled with gas are a mechanism responsible for gas dispersion and gassed power reduction, influencing impeller loading, gas dispersion and liquid recirculation and creating a specific flow regime. A turbulent flow would force the gas to break away from the cavity and exit impeller zone, flowing through the liquid fluid (KADIC and HEINDEL, 2014).

III.3.1 – Impeller design

Fluid mixing is extremely important in fermentation process and many impellers have been developed in order to optimize this process in terms of energy and mass transfer. Impellers are responsible for mechanical agitation, gas dispersion and bubble breakage in gas-dispersed STRs (KADIC and HEINDEL, 2014). Propellers, turbines (radial flow, axial flow, flat blade and disc turbine) and paddles are the three most common impellers used for low viscosity Newtonian fluid (OGUT and HATCH, 1988; OLDSHUE, 1997). Propellers usually operates in faster speed than turbines and standard three bladed propeller has poor gas-liquid dispersion, while paddles operate in lower speed than turbines (OLDSHUE, 1997).

The most common impeller classification is by flow leaving impeller zone, which can be radial or axial. Fluid dispersion in radial flow impeller occurs in radial direction while in axial flow impellers it flow along the rotating shaft (KADIC and HEINDEL, 2014; OLDSHUE, 1997).

Some examples of radial flow impellers are Narcissus impeller (NS), concave blade disc turbine (Chemineer, Smith – present work), SABA 6SRGT and Rushton type turbine (present work) (COOKE and HEGGS, 2005; KADIC and HEINDEL, 2014; UNGERMAN and HEINDEL, 2007). Some example of axial flow impellers are Lightnin A-310, Lightnin A-315, pitched blade turbine and more (COOKE and HEGGS, 2005; KADIC and HEINDEL, 2014; UNGERMAN and HEINDEL, 2007). This review will focus on radial flow impellers due to its importance to the present dissertation.

There are three stable cavity groups created by radial flow impeller, which are illustrated in Figure III.3. A vortex cavity (i) is formed at constant impeller speed and small gas flow rates, and is defined by two rolling vortices flowing at the top and at the bottom of the blade. Increasing gas flow rate will form clinging cavities (ii) and further increase will lead to large cavities (iii). The first has a gas flow clinging to the blade backside still producing vortices at the gas end, while the second is larger, smooth (DORAN, 2013; KADIC and HEINDEL, 2014; WARMOESKERKEN et al., 1984).

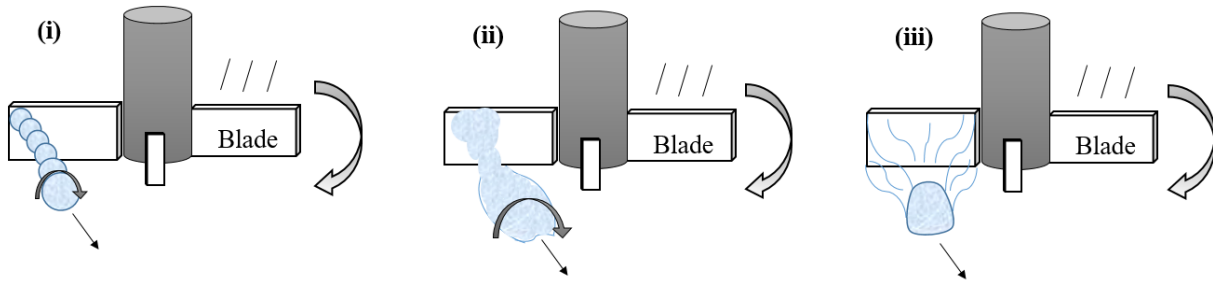


Figure III.3 Cavity formation in a radial flow impeller at constant agitation speed but gas flow rate increase; where (i), (ii) and (iii) represent the vortex, clinging and large cavities, respectively (adapted from WARMOESKERKEN et al., 1984).

Although it is logical to think that increasing gas flow rate and impeller agitation speed would benefit gas-liquid mass transfer, there is a turning point. Large cavities can sustain a higher

gas dispersion rate but when a large cavity becomes too large it hampers gas liquid mass transfer decreasing gas dispersion (KADIC and HEINDEL, 2014). This can also impact energy transfer efficiency. Although cavities reduce energy transfer between impeller and liquid due to higher superficial gas velocity, too much gas and too large cavities would reduce energy transmission and hamper mixing (OGUT and HATCH, 1988).

Considering a Rushton-type turbine, a change in the cavity structure would affect directly mass transfer, and not all cavity structures are considered the best for gas-liquid mass transfer. Even if vortex and clinging cavities are good for energy transfer, gas dispersion is lower comparing to other cavities (KADIC and HEINDEL, 2014). As gas flow is increased, a “3-3 structure” (illustrated in Figure III.4) is formed, which is a cavity structure between clinging and large cavity and is important for gas-liquid mass transfer especially due to its stability and gas-handling capacity offering optimal gas dispersion at lower power input (high superficial gas velocity) (DORAN, 2013). Further increasing gas flow rate would be inefficient, leading to impeller flooding, forming an unstable ragged cavity which affects gas dispersion and can even lead to power drawn variation in the impeller, which could damage the motor and gearbox system (KADIC and HEINDEL, 2014; NIENOW et al., 1977).

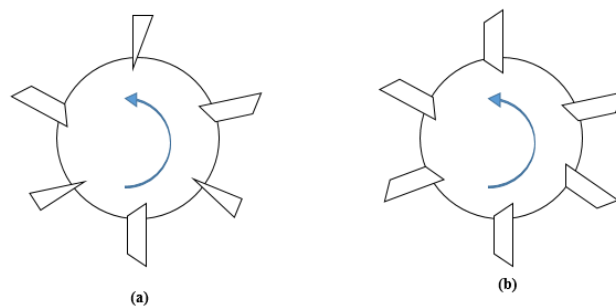


Figure III.4 Radial flow impeller scheme forming a ‘3-3’ structure with 3 clinging and 3 large cavities (a) and with large cavities (b).

Nienow et al. (1977) defined five bulk flow regimes for a single radial flow impeller, observing its influence in gas dispersion and bulk flow regime. Figure III.5 graphically illustrate the following explanation. At constant gas flow rate, it was observed that increasing impeller speed would increase gas dispersion up to a certain point where gas would become entrapped due to high turbulence and circulation and recirculation loops (Figure III.5-E). At low agitation speed, power input is very small and gas dispersion is negligible (Figure III.5-A) and, therefore, impeller type, location or separation are not relevant for the reactor hydrodynamics or mass transfer (NISHIKAWA et al., 1984). Consequently, it can be said that at these conditions, mixing in STR would approximate to a bubble column because the mixing is dominated by the sparged gas (KADIC and HEINDEL, 2014). According to Jade et al. (2006), flow regime transitions occur between three phases: flooding (Figure III.5-B), loading (Figure III.5-C) and fully dispersed (Figure III.5-D). The best operation phase for gas-liquid mass transfer would be after fully dispersed but impeller speed should not be too high in order to avoid recirculation loops (KADIC and HEINDEL, 2014).

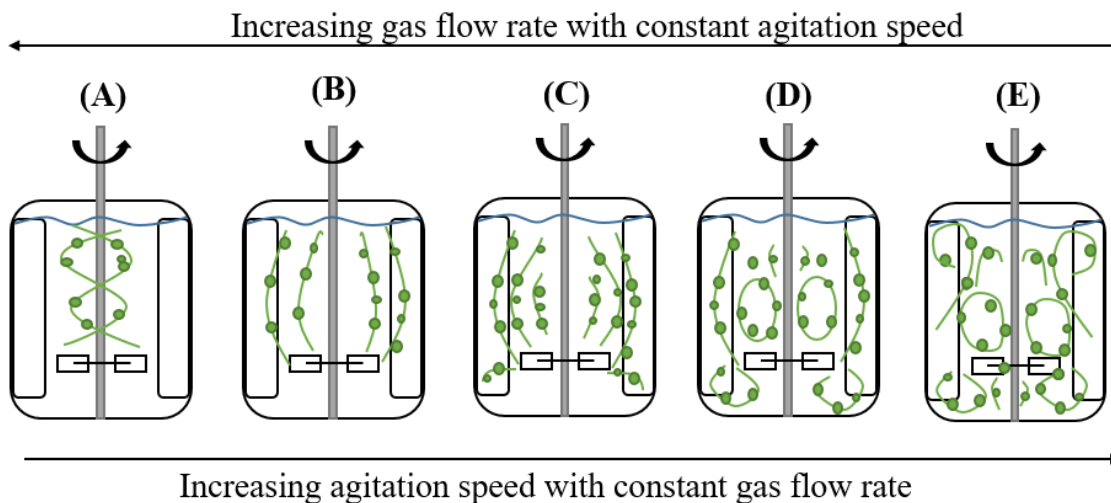


Figure III.5 Bulk flow regimes for a single radial flow impeller in a gas-liquid system (adapted from KADIC and HEINDEL, 2014).

Not only hydrodynamics phenomena are important in order to choose an impeller that would fit properly the process in mind. It is essential to correlate impeller selection with reactor geometry (UNGERMAN and HEINDEL, 2007). Figure III.6 illustrate STR measurements for the following explanation. Impeller to tank diameter (D_i/T) is typically between 1/4 and 2/3 and standardly 1/3, a configuration that minimizes cost while providing well-mixed state for liquid phase and complete gas dispersion (BORZANI et al., 2001; KADIC and HEINDEL, 2014). Impeller power draw is proportional to impeller speed to third power (N^3) and impeller diameter to the fifth power (D_i^5), which means it is cheaper to operate at higher speed than higher diameter concerning gas dispersion or mixing (KADIC and HEINDEL, 2014). Impeller clearance, which is the distance between impeller and tank bottom (H_i), should be between $T/6$ and $T/2$ depending on liquid viscosity, impeller type, sparger-impeller separation, and number of impellers (COOKE and HEGGS, 2005; KADIC and HEINDEL, 2014).

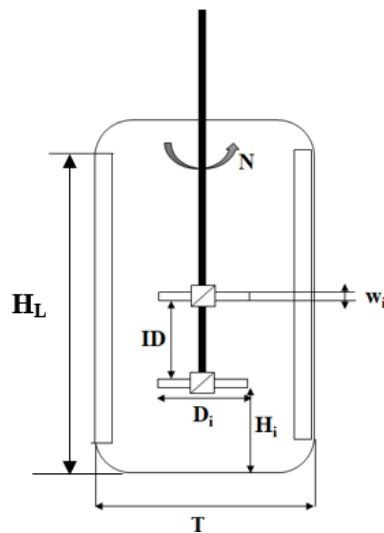


Figure III.6 Schematic Stirred Tank Bioreactor representing tank diameter (T), liquid height in vessel (H_L), impeller speed (N), impeller width (w_i), distance from the tank bottom (H_i), impeller diameter (D_i) and clearance between top and bottom impellers (ID).

Concerning gas-liquid mass transfer, Rushton-type turbines are the most used for gas-liquid dispersion because it has good mass transfer characteristics due to its good breakup and gas dispersion capabilities (CABARET et al., 2008). Its high power number produces a higher maximum shear zone near turbines producing smaller bubbles, which increases gas mass transfer (KADIC and HEINDEL, 2014). However, this same reason is a disadvantage to mixing purposes.

Moreover, Rushton-type turbines present a power draw drop of 50-65% upon gassing, which increases operational and maintenances costs. An alternative is to use concave blades disc turbines (such as CD6 Smith), which have smoother power curves and less variation in power draw drop upon gassing (UNGERMAN and HEINDEL, 2007). Also, concave turbines can handle more gas than Rushton-type turbines before flooding, improving gas-liquid dispersion, and have similar mass transfer (SMITH et al., 1977). Comparing to Rushton-type impellers, axial flow impeller have a much lower power number, which is ideal for mixing and represents lower cost. However, axial flow impellers have lower mass transfer (KADIC and HEINDEL, 2014).

Depending on the impeller there can be some disadvantages, either in mass transfer or mixing or even power draw drop. A single impeller may not provide proper agitation and gas dispersion in large reactors, and large cavities on the back of single impellers limit the amount of gas that can be properly dispersed (DORAN, 2013; KADIC and HEINDEL, 2014; NIENOW et al., 1977; OGUT and HATCH, 1988). Multiple impeller systems, which are preferred for viscous or non-Newtonian fluids, can also distribute energy throughout reactor more efficiently, proving homogenous shear rate distribution. This impeller configuration can also improve liquid recirculation and gas dispersion providing large gas-phase residence times (KADIC and HEINDEL, 2014; UNGERMAN and HEINDEL, 2007).

In order for most multiple impeller systems to work properly, impellers should have a bottom clearance of $T/4$ to $T/3$ and the distance between impellers should be at least $1 D_i$ (KADIC and HEINDEL, 2014; UNGERMAN and HEINDEL, 2007). Nishikawa et al. (1984) acquire a 74% increase in k_{LA} using a second Rushton-type impeller stating that the incorrect position of impellers could limit mass transfer increase and lead to an inefficient operation without enhancing efficiency and increasing cost. Interference also impacts power draw which can decrease up to 70% of its initial value and remain at this level throughout the process (KADIC and HEINDEL, 2014).

Moucha et al. (2003) analysed different mixed impeller configurations in terms of power density (W/m^3) and k_{LA} (s^{-1}) for low viscosity Newtonian fluid using Techmix 335 up pumping (axial), Techmix 335 down pumping (axial), pitched blade impeller down pumping (axial) and Rushton-type turbine (radial). Although the highest k_{LA} was observed using a combination of two or three Rushton-type turbines, its power concentration was also elevated. A mixed configuration of axial and radial impellers seemed more efficient for gas dispersion and mixing because its efficiency was considered by maximizing gas-liquid mass transfer at minimized power input (MOUCHA et al., 2003). According to Kadic and Heindel (2014) is usually better to use a Rushton-type or concave blade turbine on the bottom in order to achieve optimal bubble breakage, and a down-pumping axial flow impeller at the top to enhance gas liquid circulation.

III.3.2 – Power measurements

As stated by Kadic and Heindel (2014), power dissipation has a direct impact on gas-liquid mass transfer in STRs since its increase leads to bubble diameter decrease and bubble interfacial surface area increase. Moreover, an equilibrium in coalescence is reached because as bubbles break

apart due to a higher power density overcoming the surface tension force, its power density also increases the collision force, bringing the bubbles together. There are four main techniques to measure power consumption in STRs: electric, calorimetric, torque and strain measurements (KADIC and HEINDEL, 2014).

The turbine power capacity depends on impeller type, impeller diameter, impeller speed, tank diameter, tank liquid height, liquid physical properties (density, viscosity) and many other factors (BORZANI et al., 2001). Rushton et al. (1950a,b) proposed a dimensionless strategy to determine turbine power capacity in which the ungassed power number was related to Reynolds number, Froude number, liquid height to impeller diameter ratio, tank to impeller diameter ratio and more. Rushton et al. (1950a,b) conducted many experiments with different impellers, correlating ungassed power number with Reynolds number.

Power consumption is an important parameter in STR's hydrodynamics and is quantified through two dimensionless numbers, the ungassed and gassed power numbers. The ungassed power number (N_{po}) is analogous to the friction factor in pipe flow and represents the ratio of the pressure differences producing flow to inertial forces. The gassed power number (N_p) represents the ratio of the pressure differences producing flow to the inertial forces of gas-liquid dispersion and therefore measure power requirements for impellers in gas-liquid systems. Agitator flow number (N_Q) is a dimensionless number that represents the discharge coefficient used to define the volumetric flow from the impeller blade related to impeller speed and diameter (BORZANI et al., 2001; COOKE and HEGGS, 2005; KADIC and HEINDEL, 2014; OHYAMA and ENDOH, 1955). All mathematical relationship explained for N_{po} , N_p and N_Q are listed in Equations (1) to (3). Ohyama and Endoh (1955) defined the agitator flow number in order to better study the influence of aeration in system density drop, which leads to a power drop related to ungassed

systems. Therefore, graphs were proposed to correlate a ratio of impeller power input in liquid without sparged gas and with sparged gas (P/P_o) with an agitator flow number (N_Q) for various impellers configuration.

$$N_{po} = \frac{P_o}{\rho N^3 D_i^5} \quad (1)$$

$$N_p = \frac{P}{\rho N^3 D_i^5} \quad (2)$$

$$N_Q = \frac{Q_L}{N D_i} \quad (3)$$

Where, N_{po} is the ungasged power number; P_o is the impeller power input in to liquid without sparged gas; ρ is the fluid density; N is the impeller speed; D_i is the impeller diameter; N_p is the gassed power number; P is the impeller power input into the liquid when gas is sparged in the tank; N_Q is the agitator flow number; Q_L is the gas volumetric flow.

III.4 – Gas-Liquid Mass Transfer

For micro-organisms to convert the gaseous substrate into biochemicals, it is important that the nutrient is internalized by the cell. However, according to Christi (1989), transfer from gas bulk to micro-organism cytoplasm must occur in a certain pathway, and this route have eight resistances. Figure III.7 illustrates this route and resistances, which are present in the gas stagnant film inside bubble (1), at the gas-liquid interface (2), in the liquid stagnant film near gas-liquid interface (3), in the liquid bulk (4), in the liquid stagnant film closer to the cell surface (5), at the liquid-cell surface (6), in the cell cytoplasm (7) and at the site of the biochemical reaction (8) (BORZANI et al., 2001). Although mass transfer can present many resistances, most of them may be neglected in most bioreactors except for the resistance near the gas-liquid interface, which is a function of oxygen diffusivity in the liquid phase as well as the film thickness (BORZANI et al., 2001; KADIC and HEINDEL, 2014).

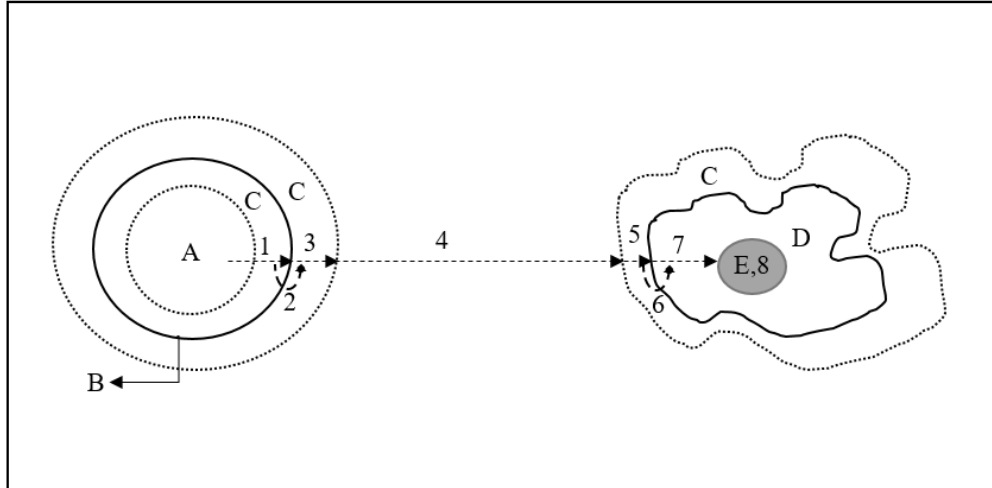


Figure III.7 Illustration of gas route to micro-organism presenting all eight mass transfer resistances, where A is the gas bubble, B is the gas-liquid interface, C are the stagnant films, D is the cell and E is the site of the biochemical reaction. Numbers 1 to 8 represent the resistances. Adapted from BORZANI et al. (2001).

The first resistance is present in the gas stagnant film where the gas will diffuse and can be neglected due to the intense movement of gas molecules. The gas-liquid interface resistance (2) will increase if some substance would adhere in the surface, like antifoams. Therefore, most of the time, the second resistance is also neglected. If the liquid is well-mixed (turbulent flow) and fluid is non-viscous, the convective flow will occur and the fourth resistance can be neglected. Concerning the resistances close to the cell, all four (5 to 8) can be neglected since cells are very small and, consequently, have a higher superficial area, which would be exposed to the liquid and resistance in the liquid stagnant film (5) would be negligible. Moreover, cell surface should not oppose to the gas permeation due to diffusive flow to cell interior and cell size being very small comparing to the gas in its exterior. Considering bacteria cells, the metabolic reactions occurs in the cytoplasm, and therefore a resistance in the cytoplasm would not be considered (BORZANI et al., 2001).

Considering a gas bubble immersed in a liquid, it can be considered that two stagnant films are present in both sides of the gas-liquid interface. At the gaseous stagnant film, mass transfer resistance is given by $(1/k_g)$, while at the liquid stagnant film mass transfer resistance is given by $(1/k_L)$. The mass flow in both stagnant films will also depend on partial pressure gradient (gas phase) and gas concentration in liquid (liquid phase). Since resistance at gaseous stagnant film can be neglected, the overall volumetric mass transfer coefficient will be given by k_L (BORZANI et al., 2001). The specific gas-liquid interfacial area is responsible for modulating this coefficient, and as the driving force is the gas concentration gradient, a model for gas-liquid mass transfer is represented in Equation (4). However, since is very difficult to measure k_L or a independently, most works choose to report the product $k_{L,a}$, known as the overall volumetric mass transfer coefficient and has units of T^{-1} (h^{-1} , s^{-1}) (KADIC and HEINDEL, 2014).

$$\frac{dC}{dt} = k_L a \cdot (C^* - C) \quad (4)$$

Where, C^* is the carbon monoxide steady-state concentration; C is the liquid phase carbon monoxide concentration; t is time; and $k_{L,a}$ is the overall volumetric mass transfer coefficient.

Therefore, considering that the gas adsorption in the liquid phase is a limiting step for gas-liquid mass transfer, improving the overall volumetric mass transfer coefficient ($k_{L,a}$) would increase gas mass transfer to liquid (KADIC and HEINDEL, 2014). Consequently, productivity would increase in systems where gas is priority for production (as a substrate or final electron acceptor). In this way, most works about synthesis gas fermentation have been improving $k_{L,a}$ using different reactor configurations or gas mixtures or even gas flow rates and agitation speeds in order to improve bioproduct formation and process commercialization (MUNASINGHE and KHANAL, 2012; RIGGS and HEINDEL, 2006; SHEN et al., 2014; UNGERMAN and HEINDEL, 2007).

However, how to measure gas concentration in the liquid phase? For dissolved oxygen measurement, several techniques have been proposed such as chemical, volumetric, tubing, optode and electrochemical electrode methods (KADIC and HEINDEL, 2014). Measurements for dissolved carbon monoxide (CO) are more complicated due to the absence of probes to measure CO concentrations (KADIC and HEINDEL, 2014). Moreover, the low solubility of the gas in water increases the uncertainty of the measure (RIGGS and HEINDEL, 2006). Measurement of CO concentration can be done by using gas chromatography (GC) or a myoglobin bioassay, which is based in the reversible bound between CO and the protein (KADIC and HEINDEL, 2014; KUNDU et al., 2003). Myoglobin's binding site consists of only one porphyrin containing iron(II) known as heme, differently from hemoglobin, which has four (LIM et al., 1995). Therefore, each myoglobin binds to one molecule of carbon monoxide. The bioassay is a simpler, faster and cheaper method when comparing to GC and results were comparable between the two methods (MUNASINGHE and KHANAL, 2014).

Table III.1 summarizes some overall volumetric mass transfer coefficient present in literature for carbon monoxide transfer in water. For the past years, different bioreactor configurations such as stirred tank reactor with microbubble sparger, hollow fiber membrane reactors and bubble columns were considered in order to enhance mass transfer in synthesis gas fermentation. Shen et al. (2014a) achieved a k_{La} of 1096.2 h^{-1} operating a hollow fiber membrane bioreactor (HFMBR), which consisted of a hollow fiber membrane contactor connected to an 8L working volume reservoir. HFMBR homogenization was performed by water recirculation (1.14 cm/s) and specific gas flow rate used was 0.625 vvm. So far, this is the highest mass transfer coefficient for carbon monoxide in water present in literature.

Table III.1 Carbon monoxide overall volumetric mass transfer coefficient for different reactors and hydrodynamics.

Reactor	N (rpm)	Q _{co} (vvm)	Microorganism	Gas	k _{La} (h ⁻¹)	Ref.
BCR	n/a	0.4	n/a	CO	72.0	(8)
CHF	n/a	n/a	n/a	CO	85.7 – 946.6	(7)
CSTR	300	n/a	<i>C. ljungdahlii</i>	CO	14.9	(4)
CSTR	400	n/a	<i>C. ljungdahlii</i>	CO	21.5	(4)
CSTR	400	0 – 0.32	n/a	Syngas	38.0	(9)
CSTR	500	n/a	<i>C. ljungdahlii</i>	CO	22.8	(4)
CSTR	600	n/a	<i>C. ljungdahlii</i>	CO	23.8	(4)
CSTR	700	n/a	<i>C. ljungdahlii</i>	CO	35.5	(4)
GLR	n/a	1.67	n/a	CO	129.6	(12)
HFMBR	n/a	0.625	n/a	CO	1096.2	(5)
HFMBR	n/a	0.029	n/a	CO	385.0	(10)
MBR	n/a	0.00625 – 0.0625	n/a	Syngas	450.0	(7)
PBC with microbubble sparger	n/a	0 – 0.021	<i>R. rubrum</i>	Syngas	2.1 for CO	(1)
STR	300	0 – 0.032	<i>C. ljungdahlii</i>	Syngas	35.0 for CO	(1)
STR	300	0 – 0.032	<i>R. rubrum</i>	Syngas	28.1 for CO	(1)
STR	300	0 – 0.032	SBR mixed culture	Syngas	31.0 for CO	(1)
STR	400	0.14 – 0.86	n/a	CO	10.8 – 155.0	(2)
STR	400	0.70 – 2.14	n/a	CO	72.0 – 153.0	(3)
STR	400	0.36 – 1.07	n/a	CO	72.0 – 122.4	(11)
STR	400	0 – 0.032	<i>R. rubrum</i>	Syngas	101.0 for CO	(1)
STR	450	0 – 0.032	<i>R. rubrum</i>	Syngas	101.0 for CO	(1)
STR	500	0.36 – 1.07	n/a	CO	129.6 – 144.0	(11)
STR	600	0.36 – 1.07	n/a	CO	147.6 – 208.8	(11)
STR	650	0.36 – 1.07	n/a	CO	172.8 – 252.0	(11)
STR	700	0.36 – 1.07	n/a	CO	187.2 – 288.0	(11)
STR with microbubble sparger	300	n/a	SBR mixed culture	Syngas	104.0 for CO	(1)
TBR	n/a	0 – 0.021	n/a	Syngas	22.0	(9)
TBR	n/a	0 – 0.021	<i>C. ljungdahlii</i>	Syngas	137.0 for CO	(1)
TBR	n/a	0 – 0.021	<i>R. rubrum</i>	Syngas	55.5 for CO	(1)
TBR	n/a	0 – 0.021	SBR mixed culture	Syngas	121 for CO	(1)

Where, n/a – not applicable; SBR – Sulfate reducing bacteria; N – impeller speed; Q_{co} – specific gas flow rate; k_{La} – overall volumetric mass transfer coefficient; BCR – Bubble Column Reactor; STR – Stirred Tank Bioreactor; CSTR – Continuous Stirred Tank Bioreactor; HFMBR – Hollow Fiber Membrane Bioreactor; CHF – Composite Hollow Fiber Membrane; MBR – Membrane Bioreactor; PBC – Packed Bubble Column; TBR – Trickle Bed Reactor/ GLR – Gas-Lift Reactor. References are Bredwell et al. (1999), 1; Riggs and Heindel (2006), 2; Ungerman and Heindel (2007), 3; Klasson et al. (1993), 4; Shen et

al. (2014a), 5; Shen et al., (2014b), 6; Munasinghe and Khanal (2012), 7; Chang et al. (2001), 8; Cowger et al. (1992), 9; Lee et al. (2012), 10; Kapic et al. (2006), 11; Munasinghe and Khanal (2014), 12.

Bredwell et al. (1999) determined carbon monoxide and hydrogen gas mass transfer to liquid phase in three different fermentations using synthesis gas as gaseous substrate. The work also compared different reactor configuration such as stirred tank reactor (STR), stirred tank reactor (STR) with microbubble sparger, packed bubble column (PBC) with microbubble sparger, and trickle bed reactor (TBR). Synthesis gas were fermented by acetogenic bacteria *Clostridium ljungdahlii*; by a triculture composed of *Rhodospirillum rubrum* and two methanogenic bacteria *Methanobacterium formicum* and *Methanosarcina barkeri*; and by a sulfate-reducing bacteria mixed culture (SBR). The results for carbon monoxide mass transfer are gathered in Table III.1. It is possible to understand that reactor configuration is extremely important for mass transfer in gas-liquid systems, especially due to hydrodynamic change in the bioreactor (KADIC and HEINDEL, 2014; OLDSHUE, 1997). The addition of a microbubble sparger in the fermentation conducted by SBR mixed culture at 300 rpm promoted a 3.7 time increase in k_{LA} for carbon monoxide. The use of a TBR instead of a STR in a fermentation using *C. ljungdalii* also increased k_{LA} significantly (4 time increase).

Most of experiments concerning carbon monoxide concentration implemented the bioassay developed by Kundu et al. (2003) in order to measure CO concentration at the liquid phase. The assay is based in the affinity between CO and myoglobin forming a carboxy-myoglobin complex, which is detected in spectrophotometer (KADIC and HEINDEL, 2014). Works presented in Table III.1, except for Bredwell et al. (1999), Klasson et al. (1993), Cowger et al. (1992) and Chang et al. (2001), determined carbon monoxide concentration in tap water (at 25 °C) using myoglobin bioassay.

Klasson et al. (1993) used the same method developed by Cowger et al. (1992) to determine k_{LA} in TBR and STR systems based in the carbon monoxide consumption and mass balance, which is similar to the one used by Bredwell et al. (1999). Chang et al. (2001) measured carbon monoxide and carbon dioxide concentration at liquid phase using gas chromatography (GC). Munasinghe and Khanal (2014) evaluated hydrogen and carbon monoxide mass transfer comparing myoglobin bioassay technique with gas chromatography determination. It was confirmed that myoglobin-protein bioassay can be used as a reliable method to determine carbon monoxide k_{LA} in synthesis gas fermentation studies. Moreover, the method is much simpler, faster and cheaper when comparing to GC (MUNASINGHE and KHANAL, 2014).

Comparing to Bredwell et al. (1999) and Klasson et al. (1993), k_{LA} obtained in systems without microorganism are higher. Microbial cells offer an additional resistance to mass transfer, which impacts especially membrane bioreactors where a biofilm surface is formed during fermentation (MUNASINGHE and KHANAL, 2010). In recent articles, k_{LA} is determine separately from fermentation, using only tap water and a pure gas or syngas mixture, even when CO concentration was measured using GC (MUNASINGHE and KHANAL, 2012; MUNASINGHE and KHANAL, 2014; RIGGS and HEINDEL, 2006; SHEN et al., 2014a; SHEN et al., 2014b; UNGERMAN and HEINDEL, 2007). Therefore, Equation (4) can be used in the absence of micro-organisms at liquid phase, which implies that the only resistance to mass transfer is present at the stagnant liquid film (BORZANI et al., 2001; CHRISTI, 1989; KADIC and HEINDEL, 2014)

III.5 – Parameter Estimation

Mathematical model is a structure that aims to describe real-life phenomena based on experimental observation. It establishes a relationship between independent variables ($x \in X \subseteq \mathbb{R}^{N_X}$) and dependent variables ($y \in Y \subseteq \mathbb{R}^{N_Y}$) in order to explain the system's behaviour. The model structure also contains parameters ($\theta \in \Theta \subseteq \mathbb{R}^{N_P}$), which are constant values that contains inherent properties of the process or problem nature (ALBERTON, 2013). Most of the time, parameters cannot be measured and have to be estimated through experimental data. This process is called Parameter Estimation and is based on adjusting parameter values so the dependent variables predicted through the model are as close as possible to experimental data, considering measurement uncertainty. This adjustment is conducted by an objective function, which measures the distance between experimental values and predicted values. The parameter is obtained by optimizing this objective function (ALBERTON, 2013; SCHWAAB and PINTO, 2007)

Experimental deviations in procedures like sampling and dilution lead at some extent to uncertainties in the experimental data acquired. Therefore, it is important to proper characterize this uncertainty in order to evaluate the final result in statistical terms (SCHWAAB et al., 2008). In this way, parameter estimation is very important and can be divided in three steps (SCHWAAB and PINTO, 2007):

- 1) Definition of an objective function.
- 2) Optimization of this objective function in order to find and optimum point (minimum or maximum depending on the problem). Usually, numerical techniques are required for this step.
- 3) Precise statistical interpretation of the parameter values estimated and the model prediction quality using these parameters.

These steps will be discussed briefly in the following sections. Important algorithm and functions will be detailed in Chapter IV. For more details about parameter estimation and optimization methods works from Schwaab (2005), Schwaab and Pinto (2007) and Schwaab et al. (2008) are suggested.

III.5.1 – Defining an objective function

In order to introduce the idea of distance or proximity between predicted and experimental values, it is necessary to define a metric, the objective function, which can be challenging. A distance function is defined as a positive real number and in order to be used as an objective function it needs to have statistical significance. Therefore, two hypotheses must be made: that the model is perfect and that the experiment was well performed. The first assumes that the model structure is correct and that any eventual deviation between experimental data and predicted value is due only and exclusively to experimental uncertainty. The second assumes that measurement deviation is so small that it is possible to admit that the probability to find experimental data is maximum (SCHWAAB and PINTO, 2007).

Although least squares is the most common choice for objective function, this method is very limited because it admits all variables can be obtained with same precision in any experimental condition (ALBERTON, 2013). However, measurement deviations can occur at any time during experiments and experimental measurement are not necessarily independent. Maximum likelihood estimation (MLE) is another common way to estimate parameters and is a method based on very simple premises allowing a strict analysis of any experimental problem (SCHWAAB and PINTO, 2007). These premises are admitting that experimental uncertainty

distribution is known; and admitting that perfect model hypothesis and well performed experiment hypothesis are valid (ALBERTON, 2013; SCHWAAB and PINTO, 2007).

According to the maximum likelihood principle (detailed in SCHWAAB and PINTO, 2007), assuming that variables have a normal probability distribution and are not correlated, and that independent variables are deviation-free, objective function can be described mathematically as in Equation (5) (SCHWAAB and PINTO, 2007). Parameter reliability is directly influenced by experimental accuracy and precision, therefore a suitable definition of the experimental uncertainties is highly desirable (ALBERTON, 2013).

$$F_{obj} = \sum_{i=1}^{NE} \sum_{j=1}^{NY} \frac{(y_{i,j}^e - y_{i,j}^m(x_i, \theta))^2}{\sigma_{y_{i,j}}^2} \quad (5)$$

Where, F_{obj} represents the objective function; NE the number of experiments; NY the number of dependent variables; x the independent variables; θ the parameters; y^e are the experimental values and y^m are the predicted values; and $\sigma_{y_{i,j}}^2$ experimental variance.

III.5.2 – Defining an optimization strategy

The optimization strategy depends on the model chosen for the parameter estimation. If the model is linear, minimization will have analytical solutions. If the model is linear and assuming a normal distribution for deviations between predicted and experimental values, confidence region for the estimated parameter will be a hyper-ellipsoid in a parametric space with a centre point representing the estimated parameter (DRAPER and SMITH, 1998; SCHWAAB and PINTO, 2007). However, when a model is non-linear, iterative processes are needed to minimize the objective function and to obtain the confidence region. For this minimization it is important to

consider the parameter space size, the existence of a local minima, the continuity of the objective function and the sensitivity of the objective function for each model parameters (HIBBERT, 1993).

Many methods can be used in order to optimize the objective function but most are based on derivatives, a deterministic method in which minimization is performed along a direction that combines gradient vector ($\partial F_{Obj}/\partial\theta$) and Hessian matrix ($\partial^2 F_{Obj}/\partial\theta^2$). Direct search methods are based only on calculating the objective function without derivatives (SCHWAAB et al., 2008). However, derivative methods are preferred because convergence velocity and reliability are better than direct search (BARD, 1974). Both methods may be known as search methods since both searches starts from an initial parameter guess and optimization evolves to a minimum (SCHWAAB et al., 2008).

However, not all parameter estimation run smoothly and some minimization can lead to numerical problems associated with a large number of model parameters, high model parameter correlation and multimodal nature of the objective function (SCHWAAB et al., 2008). Non-deterministic methods, such as Genetic Algorithm – GA (GOLBERG, 1989), Simulated Annealing – SA (KIRKPATRICK et al., 1983) and Particle Swarm Optimization – PSO (KENNEDY and EBERHART, 1995), can overcome these numerical problems.

Non-deterministic optimization methods are methods bases on empirical evolutionary rules that frequently mimic successful optimization strategies found in nature. They are characterized by a large number of function evaluations and a random search character, which assumes high probability of finding a global minima (SCHWAAB and PINTO, 2007). Usually, these methods are flexible and can be used for many objective functions and constraints. Also they can be implemented in problems that have many model parameters. Moreover, non-deterministic methods are not sensitive to initial guess parameter, do not need objective function derivatives and can

perform global optimization through extensive calculation of objective functions in the parametric space (SCHWAAB et al., 2008). According to Schwaab (2005), as a non-deterministic method, PSO allow an improved parameter estimation performance with less computational effort when compared to GA and SA.

Particle Swarm Optimization method is based on swarm behaviour and was proposed by Kennedy and Eberhart (1995). Each individual of the swarm (particle) remembers the best solution found by itself and by the whole swarm along the search path. Particles will move along the search and exchange information with other particles. The algorithm will be detailed in Chapter IV. The method is conducted in two stages: exploration and exploitation. Exploration stage is characterized by the random search in which particles conduct a global search over the searching area. Exploitation stage is characterized by concentrating the search around the more promising regions, leading to an improvement in solution. Therefore, a proper balance between both stages is fundamental to guarantee the search success and finding a minimal value for the objective function. The main disadvantage of PSO is the high number of objective functions evaluations, which may require longer computational times (SCHWAAB et al., 2008).

It is also possible to combine derivative-based methods with non-deterministic optimization methods. This approach usually starts with the non-deterministic optimization method in order to search the parametric space globally and obtain a good estimative for parameters values. Then, a deterministic method is performed (derivative-based, for example Newton-Raphson) which accelerate final convergence and allows parameter estimation with high accuracy (SCHWAAB and PINTO, 2007).

III.5.3 – Statistical interpretation of estimated values

After minimizing the objective function, statistical analysis of the values obtained is necessary in order to achieve valid and high quality results. This step would depend on the objective function and optimization method used for parameter estimation. As stated before, this step is important, especially due to experimental uncertainty that are included in the estimated parameter.

Experimental uncertainty is represented by the experimental covariance. However, this matrix can be partially or totally unknown (ROMAGNOLI and SÁNCHEZ, 1999). Therefore, it is assumed that experimental uncertainties are independent, so experimental covariance matrix is diagonal and its elements are originated from the experimental variance matrix. Equations (6) to (8) result in experimental covariance and mean for NE experiments considering two variables x_i and $x_j \in X \subseteq \mathbb{R}^{NX}$.

$$\mu_x = \frac{1}{NE} \sum_{k=1}^{NE} x_k \quad (6)$$

$$v_{x_i, x_j} = \frac{1}{(NE - 1)} \sum_{k=1}^{NE} (x_{i,k} - \mu_{x,i})(x_{j,k} - \mu_{x,j}) \quad (7)$$

$$V_x = [v_{x_i}, v_{x_i}] \quad (8)$$

Where, μ_x is the mean value for variables; NE is the number of experiments; v_{x_i} and v_{x_j} are variances for x_i and x_j , respectively; V_x is the covariance matrix.

It is important to understand that if uncertainties are dependent values this can lead to a bad conditioned covariance matrix due to singularity proximity and it means the matrix cannot be inverted. This matter is extremely sensible when the inverted covariance matrix is used to analyse variables in the objective function and parametric uncertainty. This leads to problems in

minimizing objective function and parameters with estimated values that do not have any physical or statistical meaning (SANTOS and PINTO, 1998).

The quality of the parameter estimated value is evaluated through a parameter covariance matrix (V_{θ}). This matrix is not known accurately because it is based on a limited quantity of experimental data that should represent all possible experiments (SCHWAAB, 2007). Covariance matrix can be obtained using sensitivity matrix (B) through Equation (9) (BARD, 1974; SCHWAAB and PINTO, 2007).

$$V_{\theta} = (B^T V_x^{-1} B)^{-1} \quad (9)$$

Where, V_{θ} is the parameter covariance matrix; B is the sensitivity matrix ($\partial X / \partial \Theta$ and $\partial Y / \partial \Theta$); and V_x is the experimental covariance matrix.

Considering there is no deviation in the independent variable, Equation (9) can be reduced to Equation (10). Parametric covariance matrix can be inverted in what is called Fisher's Information Matrix (FIM), which the direct use could avoid inversion proceedings. However, elements from FIM matrix can provide an inadequate information about parameters due to a possible linear dependence between parameters. The parametric covariance matrix is really important because it can be used to define confidence interval, significance level and correlation between parameters.

$$V_{\theta} = \left(\left(\frac{\partial Y}{\partial \Theta} \right)^T V_y^{-1} \frac{\partial Y}{\partial \Theta} \right)^{-1} \quad (10)$$

Confidence interval can be obtained admitting that parametric uncertainty has normal probability distribution as well as experimental uncertainty. Although only valid for linear models, it is a good approximation for non-linear model when experimental deviation is low. Therefore, assuming a t-student distribution according to the estimation degree of freedom and the confidence

level chosen, confidence interval can be determined as Equation (11). In case the parameter presents no significance, confidence interval will have positive and negative values, even zero (SCHWAAB and PINTO, 2007).

$$\theta'_i - t \cdot \sigma_{\theta_i} < \theta_i < \theta'_i + t \cdot \sigma_{\theta_i} \quad (11)$$

Where, θ'_i is the parameter estimated value; t is the probability using a t-student distribution for a certain degree of freedom and confidence level; and σ_{θ_i} is the parameter standard deviation.

However, confidence interval does not have any information about parametric correlation, which statistically express parameter interaction. Parametric correlation (Equation (12)) express how one parameter depends on other parameter values and can cause many problems to parameter estimation, such as an inefficiency in minimizing the objective function, resulting in a parameter estimated values with low statistical significance (ALBERTON, 2013; SCHWAAB and PINTO, 2007; WATTS, 1994). It can be caused bad experimental planning and inappropriate model structure, which can be avoided using statistical planning and techniques to change the present model parameters (ALBERTON, 2013). Nonetheless, sometimes is not possible to avoid parametric correlation due to model non-linearity (SCHWAAB, 2007).

$$\rho_{ij} = \frac{\sigma_{ij}^2}{\sigma_i \sigma_j} \quad (12)$$

Where, ρ_{ij} is the parametric correlation coefficient; σ_{ij}^2 is the covariance matrix; and σ_i and σ_j are the standard deviations.

In order to consider the parametric correlation in the statistical analysis of the parameter estimated values, a confidence region can be calculated. Since experimental data are only part of a phenomenon which has uncertainties, it is not possible to determine a parameter exact value but a region of possible parameter values. This is named confidence region, a set of parameter values that describe experimental data with some statistic precision (BARD, 1974; SCHWAAB and

PINTO, 2007). In order to establish a confidence region, it can be assumed that parametric uncertainty has a normal probability distribution and that a linear approximation for the model is considered valid. Confidence regions for linear models tend to have an ellipsoid shape and this can also be valid in very restricted cases for non-linear models, which normally have many different shapes (SCHWAAB et al., 2008). Three methods are normally used for accurate descriptions of confidence regions: profiling t-plot (BATES and WATTS, 1988; WATTS, 1994), lack-of-fit method (HALPERIN, 1963; HARTLEY, 1964; WILLIAMS, 1962) and likelihood method (BEALE, 1960). Profiling t-plots were designed to calculate confidence interval and an interpolation is needed in order to obtain a confidence region. Likelihood method is exact only for linear models but confidence region obtained for non-linear models can be close to exact depending on the model structure. Exact confidence region can also be obtained with lack-of-fit method, however computational effort is higher because it needs model derivatives to work. Likelihood is preferred since lack-of-fit and profiling t-plots produce very similar confidence regions (SCHWAAB et al., 2008).

Beale (1960) proposed a mathematical expression, Equation (13), to determine confidence regions, which is exact for linear models with experimental deviation following a normal probability distribution with a confidence level of $(1-\alpha)$. If model is non-linear and experimental deviation follows an arbitrary distribution, the term accounting for Fisher's distribution is substituted by a constant c , which depends on the required confidence level and on the defined objective function.

$$F_{Obj}(\theta) \leq \min(F_{Obj}(\theta)) \left(1 + \frac{NP}{(NE \cdot NY - NP)} F_{NP, NE \cdot NY - NP}^{(1-\alpha)} \right) \quad (13)$$

Where, $F_{Obj}(\theta)$ is the objective function at parameter θ ; $\min(F_{Obj}(\theta))$ is the objective function at the minimum; NP is number of parameters; NE is the number of experiments; NY is the number of

dependent variables; F is the superior limit in Fisher's distribution given NP and $(NE \cdot NY - NP)$ degrees of freedom considering a confidence level of $(1-\alpha)$.

Confidence regions obtained through Equation (13) are called likelihood regions and can be disjoint and unbounded due to the contours of complex non-linear functions (SCHWAAB et al., 2008). For cases such as the present work, when two parameters are being estimated, likelihood regions can be determined with standard contouring methods (BATES and WATTS, 1988). For more parameters, PSO would facilitate the process because it is required an evaluation of a large number of points to produce a satisfactory contour (SCHWAAB et al., 2008). Using Particle Swarm Optimization in parameter estimation would allow a high number of objective function evaluations. Using the selection expressed in Equation (13), a set of parameters can be properly selected and a likelihood confidence region can be determined. The only additional computational efforts to PSO algorithm is selecting the points that satisfy Beale's Equation (13).

Confidence regions can lead to very good conclusions about estimated parameter values and its statistical significance. However this depends on the model linear approximation and, therefore, on the objective function quadratic approximation (ALBERTON, 2013). Figure III.8 is based on Alberton (2013) and represents some shapes that can appear when parametric uncertainty is analysed using a linear model.

Although Figure III.8 considers a linear model, some visual concepts are very important. Region A represents a confidence interval, which broad area states there is no information about parametric correlation. Region B and C represents confidence regions with low or absent parametric correlation and high parametric correlation, respectively. Regarding confidence region in non-linear models, even when experimental deviations are normally distributed sometimes the same cannot be said to parameter deviations. Therefore, an elliptical shape confidence region for

a non-linear model can be a poor approximation (SCHWAAB et al., 2008). However, elliptical approximations for confidence regions are widely used due to its simplicity. Moreover, in this case parameter estimated values are assumed to follow normal distribution, so only estimated point and covariance matrix are necessary (BARD, 1974).

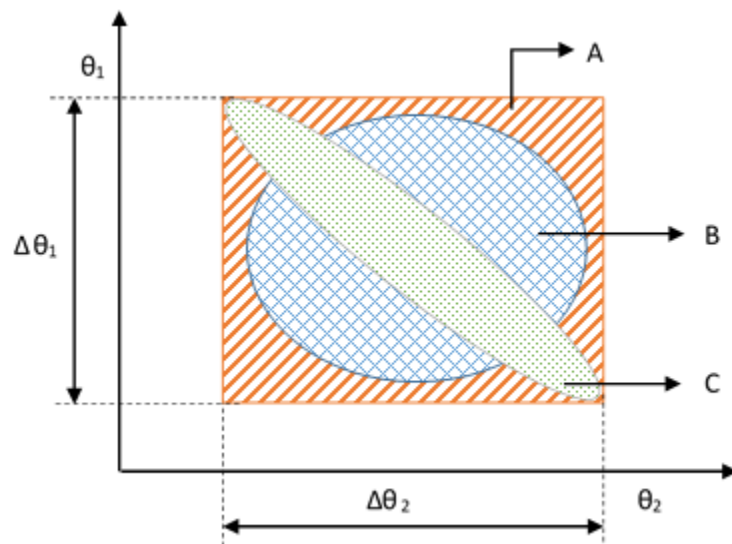


Figure III.8 Parametric uncertainty shapes for a linear model, showing parametric correlation between parameters θ_1 and θ_2 . Region A represents a confidence interval; B represents an ellipsoid confidence region; and C a steep ellipsoid confidence region (adapted from ALBERTON, 2013).

Chapter IV – MATERIALS AND METHODS

This Chapter resumes all equipment, materials and methods used in order to measure carbon monoxide concentration in liquid phase and determining the overall volumetric mass transfer coefficient.

IV.1 – Equipment and Software

Experiments and analysis were conducted using:

- 1) Spectrophotometer UV-VIS Shimadzu UV-1800 – Shimadzu;
- 2) Software UV Probe 2.43– Shimadzu;
- 3) Software MATLAB® version 2015R– MathWorks;
- 4) Scale Shimadzu ATX224 – Shimadzu;
- 5) Polystyrene cuvette, 1,5 ml e optical path 10-mm ($340 \leq \lambda \leq 800$ nm);
- 6) Water purification system, Milli-Q, Simplicity® – Millipore Corporation;
- 7) Distillation machine model NT 425 – Novatecnica;
- 8) Beaker, glass stirring rod, test tube, automatic pipette and tips;
- 9) Laboratory pH meter, model DM 22 – Digimed;
- 10) Rubber septum;
- 11) Benchtop jacketed bioreactor, TEC-BIO-1.5 – Tecnal Scientific Equipments Co.;
 - a. Nominal volume: 1.5 L.
 - b. Working volume: 750 mL and 1.0 L.
 - c. Internal diameter: 9 cm.
 - d. Two radial impellers, six bladed, CD6 Smith-type (bottom) and Rushton-type (top). $D_i = 4.4\text{cm}$; $H_i^{\text{Smith}} = 4\text{cm}$; $H_i^{\text{Rushton}} = 11.5\text{cm}$; ID = 7.5 cm diameter.
 - e. Sparger, round, 3.5-cm diameter, 8 holes with 0.5-mm diameter each.

- f. Jacked filled with distilled water;
 - g. Temperature probe and control system;
- 12) High-performance dispersing instrument – Ika T 25 digital ULTRA-TURRAX®;
 - 13) Peristaltic pump, model LDP-101-3 – MS TECNOPON Instrumentação;
 - 14) Rotameter, model FM-1000VIH – Matheson.

IV.2 – Reagents and Solvents

- 1) Myoglobin 90% pure obtained from equine heart muscle ref M1882 – Sigma-Aldrich;
- 2) Potassium phosphate monobasic(KH_2PO_4) – VETEC;
- 3) Potassium phosphate dibasic (K_2HPO_4) – VETEC;
- 4) Potassium hydroxide (KOH) – VETEC;
- 5) Phosphoric acid (H_3PO_4) – ISO FAR;
- 6) Sodium dithionite, ref 71699 – Sigma-Aldrich;
- 7) Carbon monoxide 99.5% pure – White Martins Gases Industriais Ltda.;
- 8) TWEEN® 80, ref. 758 – ISO FAR;
- 9) Perfluorodecalin, 95% – Apollo Scientific Limited);

IV.3 – Experimental Conditions

Experimental data for overall volumetric mass transfer coefficient determination was based in the conditions described at Table IV.1. Three agitations speed (100, 300 and 500 rpm); two temperatures (25 and 37 °C); two volumes (0.75 and 1.0 L); four gas flow rates (0.5, 1.0, 2.0 and 2.5 L/min), which resulted in five specific gas flow rates (0.7, 1.3, 2.0, 2.5 and 2.7 vvm); and four

compositions of liquid phase (pure distilled water; distilled water + PFC; distilled water + Tween® 80; and distilled water + PFC + Tween® 80) were tested.

Table IV.1 Experimental conditions for overall volumetric mass transfer coefficient estimation.

N (rpm)	T (°C)	V (L)	F_{CO} (L/min)	Q_{CO} (vvm)	Liquid Phase
100	25	0.75	0.5	0.7	Distilled water
100	25	0.75	1.0	1.3	Distilled water
100	25	0.75	2.0	2.7	Distilled water
300	25	0.75	0.5	0.7	Distilled water
300	25	0.75	1.0	1.3	Distilled water
300	25	0.75	2.0	2.7	Distilled water
300	25	0.75	2.0	2.7	Distilled water + PFC
300	25	0.75	2.0	2.7	Distilled water + Tween® 80
300	25	0.75	2.0	2.7	Distilled water + PFC + Tween® 80
300	37	0.75	2.0	2.7	Distilled water
500	25	0.75	0.5	0.7	Distilled water
500	25	0.75	1.0	1.3	Distilled water
500	25	0.75	2.0	2.7	Distilled water
500	37	0.75	2.0	2.7	Distilled water
500	25	0.75	2.0	2.7	Distilled water + PFC
500	25	0.75	2.0	2.7	Distilled water + Tween® 80
500	25	0.75	2.0	2.7	Distilled water + PFC + Tween® 80
500	25	1.00	2.0	2.0	Distilled water
500	25	1.00	2.0	2.0	Distilled water + PFC
500	25	1.00	2.0	2.0	Distilled water + Tween® 80
500	25	1.00	2.0	2.0	Distilled water + PFC + Tween® 80
500	25	1.00	2.5	2.5	Distilled water
500	25	1.00	2.5	2.5	Distilled water + PFC
500	25	1.00	2.5	2.5	Distilled water + Tween® 80
500	25	1.00	2.5	2.5	Distilled water + PFC + Tween® 80

Where, N is the impeller agitation speed; T is the STR's temperature; V is the STR's volume; F_{CO} is the gas flow rate; and Q_{CO} is the specific gas flow rate.

Gas flow rate and agitation speed were chosen based in fermentation conditions and equipment limitations. Temperature was set at 25 °C since most works in literature determine k_{LA} for carbon monoxide at this temperature; and 37 °C because its *Clostridium* optimal temperature

for synthesis gas fermentation. The STR operated during these experiments have a dual impeller configuration. Therefore, in order to fully access both Smith (bottom) and Rushton (top) impellers, working volume was increased from 0.75 L to 1.0 L.

Four different liquid phase compositions were tested to evaluate its effect on carbon monoxide mass transfer to liquid phase. Tap water is mainly used in literature for CO concentration determination but distilled water was chosen due to its improved quality when compared to laboratory's tap water. PFC was mixed with distilled water due to its capacity to enhance O₂ transfer to the liquid phase and its considerable affinity to CO. However, since PFC have a poor solubility in water, Tween® 80 was also mixed to distilled water and PFC to improve gas dispersion and liquid phase homogenisation. The emulsions distilled water + Tween® 80 and distilled water + PFC + Tween® 80 were prepared using a high performance dispersing instrument (ULTRA-TURRAX®).

IV.3.1 – Reynolds and Froude numbers

Reynolds and Froude are two important dimensionless numbers concerning reactor hydrodynamics. Reynolds number determines the nature of the flow. It can be defined as the ratio of inertial force to viscous or friction force and interpreted as the ratio of dynamic pressure to shearing stress, as represented in Equation (14) (COULSON and RICHARDSON, 1999). For agitated vessels, Reynolds number below 10 indicates a laminar flow, while a number above 10⁴ indicates a turbulent flow (BORZANI et al., 2001). Froude number measures the ratio of inertia force on an element of fluid to the weight of the fluid element, or the inertial force divided by gravitational forces, as represented in Equation (15). It governs the extent of swirling and vortexing in an unbaffled stirred tank (NAUMAN, 2008). A critical flow will have a Froude number of 1,

and supercritical and subcritical flows will have Froude numbers above and below 1.0, respectively.

Reynolds and Froude numbers were calculated for pure distilled water at 25 and 37 °C. They were not determined for the other liquid phases due to the lack of information about these mixtures' densities and dynamic viscosities. Water density and dynamic viscosity at 25 °C were considered, respectively, 997 kg/m³ and dynamic viscosity 0.000889 N.s/m²; and at 37 °C, respectively, 993.3 kg/m³ and 0.0006922 N.s/m². Reynolds and Froude

$$Re = \frac{N \cdot D_i^2 \cdot \rho}{\mu} \quad (14)$$

$$Fr = \frac{N^2 \cdot D_i}{g} \quad (15)$$

Where, Re is the Reynolds number; N is the agitation speed; D_i is the impeller diameter; ρ is the fluid's density; μ is the fluid's dynamic viscosity; Fr is the Froude number. And g is the gravitational force (admitted 9.81 m/s²).

IV.4 – Myoglobin Bioassay Technique

Procedure to measure carbon monoxide concentration in liquid phases is very delicate and prone to many experimental deviations mainly due to low volume manipulation and the presence of oxygen. Therefore, important care must be taken during experimental samplings and analysis such as covering cuvettes edge with a rubber stopper in order to decrease oxygen interference in the test. The bioassay is based on carbon monoxide and oxygen affinity for myoglobin as well as sodium dithionite capacity as a reducing agent. The complexation of myoglobin with carbon monoxide occurs in a 1:1 ratio since myoglobin has only one heme (LIM et al., 1995). Sodium dithionite reacts with oxygen in water also in a 1:1 ratio (BAJPAL, 2005). The bioassay technique here described is based on Kundu et al. (2003) and Kadic and Heindel (2014).

IV.4.1 – Phosphate buffer solution (0.1 M, pH 7.0)

Potassium phosphate dibasic (3.3 g) and potassium phosphate monobasic (11.0 g) were mixed in 1.0 L of deionized water, resulting in a 0.1 M solution. The pH was adjusted to 7.0 using digital pH meter and 1 M solutions of potassium hydroxide and phosphoric acid.

IV.4.2 – Myoglobin solution

One gram of myoglobin (Mb), a dark red powder with strong iron smell, was dissolved in 25 mL of phosphate buffer (0.1 M and pH 7.0). Slow stirring is important in order to decrease foam formation. Mb solution total volume was separated in 24 centrifuge tubes (2 mL total volume) with 1 mL each. Tubes were stored in freezer at -20 °C soon after preparation since Mb solution is extremely sensitive to temperature. For the same reason, Mb solution should only be thawed just before usage in order to avoid myoglobin degradation.

The myoglobin solution is the base solution for this bioassay. It is used to prepare the test solution, which will be fundamental for sample analysis and base-spectra analysis. Therefore, it is very important to measure the myoglobin concentration. After a 2-mL centrifuge tube is thawed, 1 μ L of Mb solution is withdrawn and added to 1 mL of phosphate buffer 0.1M pH 7.0 present in a 1.5-mL polystyrene (PS) cuvette, which is covered with a rubber stopper. A spectrum is obtained in spectrophotometer between 400 and 700 nm wavelength with an absorbance peak at 409 nm. After scanning, 1 μ L of Mb solution is added to the solution and the PS cuvette is scanned. This procedure continues until an absorbance peak of approximately 1.5 is reached at 409 nm.

This spectrum represents the interaction between myoglobin and oxygen dissolved in solution and is one of the base-spectra, named “oxi” spectrum (MbO₂). It is used to obtain the myoglobin solution concentration (C_p) and dilution ratio (DR). Equation (16) and (17) represent

the mathematical expressions for C_p and DR evaluation and Figure IV.1 illustrates an “oxi” spectra scanned between 400-700 nm wavelength range.

$$C_p = \frac{Abs}{\lambda \cdot \epsilon_m} \quad (16)$$

$$DR = \frac{V_{Mb}(\mu l)}{V_B(ml)} \quad (17)$$

Where, C_p is the myoglobin solution concentration; Abs is the spectrum absorbance peak at 409 nm; λ is the cuvette optical path (1 cm); ϵ_m is the extinction coefficient ($188 \cdot 10^{-3} [\mu M \cdot cm]^{-1}$, ANTONINI and BRUNORI, 1971; CASTRO-FORERO et al. 2009); DR is the dilution ratio; V_{Mb} is the total volume of myoglobin solution added to PS cuvette (in μL); and V_B is volume of buffer added to the cuvette (1 mL).

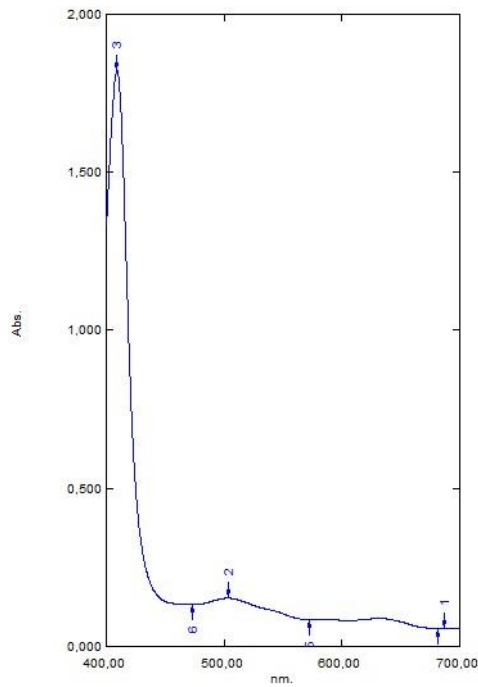


Figure IV.1 “Oxi” spectrum scanned using spectrophotometer at 400-700 nm wavelength.

IV.4.3 – Test solution

Test solution is a mix of buffer and myoglobin solution prepared to perform the assay. From data obtained through the “oxi” spectrum, a test solution is prepared depending on how many cuvettes will be needed during the assay (n samples withdrawn from the bioreactor) and 3 reference solutions or base-solutions. Therefore, the total amount of cuvettes used would be $n+3$. In each cuvette, a 1 ml of test solution should be added, so $(n+3)$ ml of buffer (V_B) should be mixed with myoglobin in a beaker. Considering DR obtained from “oxi” spectrum, the total volume of myoglobin to prepare the test solution will be $V_{Mb} = DR \cdot V_B = DR \cdot (n + 3)$. After the test solution is prepared, it is separated in the cuvettes which are covered with rubber stoppers.

IV.4.4 – Reference solution and spectra

Samples and reference solutions are prepared by adding 1 mL of test solution a 1.5 mL PS cuvettes. Reference solutions are scanned in spectrophotometer between 400-700 nm wavelength range and generate base-spectra or reference spectra. One of this cuvettes is a reference solution with myoglobin completely bounded to oxygen (MbO_2) and is represented by an “oxiTS” spectrum.

In order to eliminate any possible trace of oxygen in the other cuvettes and avoid affecting carbon monoxide concentration measurement, small quantities of sodium dithionite ($Na_2S_2O_4$) are added to all cuvettes except to the solution that generated the “oxiTS” spectrum. Other cuvette containing myoglobin, buffer and $Na_2S_2O_4$ represented the solution that generated the “deoxi” spectrum (Mb). This base-spectrum represents a solution with only myoglobin, free of oxygen and carbon monoxide, so is a zero CO concentration limit.

The other base-spectrum is obtained by purging pure CO into one of the cuvettes containing the test solution and $\text{Na}_2\text{S}_2\text{O}_4$. The excess of CO guarantees that all myoglobin will be bonded to the CO molecule. This is known as the “carboxi” spectrum (MbCO) and represents a solution saturated with CO, where all myoglobin are combined with carbon monoxide. The base-spectra are obtained in spectrophotometer at 400-700 wavelength. Figure IV.2 illustrate the three reference or base-spectra, each one with its specific absorbance peak at a specific wavelength.

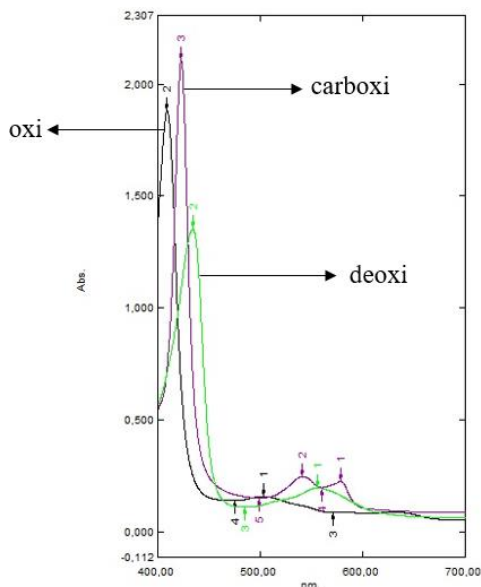


Figure IV.2 Reference or base-spectra used in the present work: deoxi (Mb), oxi (MbO_2), and carboxi (MbCO).

IV.4.5 – Sampling and sample spectra

Figure IV.3 illustrate the sampling process used in the present work. A winged infusion set (Wiltex, 0.64 x 19 mm) coupled with a 5.0 mL syringe (BD PlastipakTM) was placed in the STR’s recirculation line. Sample withdrawn was performed in regular intervals of 10 ± 3 s. A 10 μL Gas-Tight[®] syringe (Hamilton[®], model 1701) was used to transfer 10 μL samples from the 5.0 mL syringe to the tapped PS cuvettes containing test solution and $\text{Na}_2\text{S}_2\text{O}_4$. These solutions were

scanned in spectrophotometer at 400-700 nm wavelength range, originating the sample spectra. An example of all spectra obtained during one assay is presented in Figure IV.4.

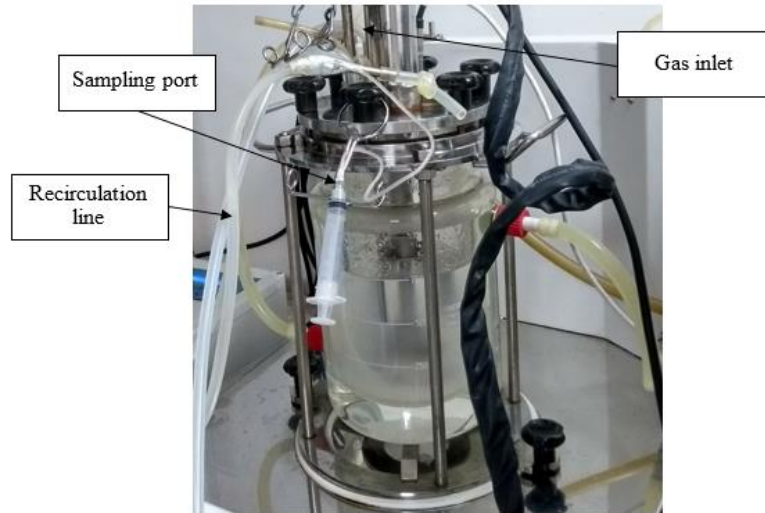


Figure IV.3 Equipment set-up used during mass transfer coefficient determination, representing sampling port, and recirculation line and gas inlet.

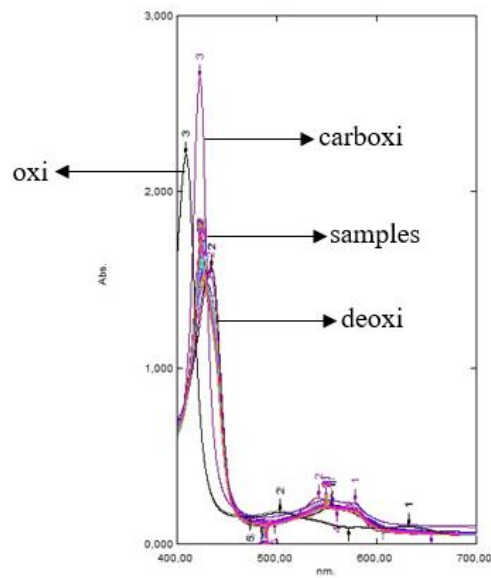


Figure IV.4 Sample and reference spectra obtained in spectrophotometer to determine dissolved carbon monoxide concentration.

IV.3.5 – Dissolved carbon monoxide concentration

All spectra data, reference and sample, were loaded in MATLAB as well as all time measurements. It is important that sample spectrum is placed between “deoxi” (zero carbon monoxide concentration limit) and “carboxi” (saturated carbon monoxide concentration limit) since these are, respectively, the minimum and maximum carbon monoxide concentration for the test (Figure IV.4). A least-square routine was created to interpolate sample spectra data between “deoxi” and “carboxi” spectra, resulting in a similarity to each spectra and a percentage of similarity (SS). The mathematical expression to obtain CO concentration is presented in Equation (18). Therefore, it is possible to calculate all CO concentration in liquid phase at specific sampling times.

$$C_{CO} = C_p SS \left(\frac{V_T}{V_S} \right) \quad (18)$$

Where, C_{CO} is the carbon monoxide concentration at the liquid phase; C_p is the myoglobin concentration; SS is the percentage of similarity; V_T is the total volume in the cuvette and V_S (10 μ l) is the sample volume of dissolved carbon monoxide.

IV.5 – Overall Volumetric Mass Transfer Coefficient (k_{LA})

Considering that the CO concentration in the liquid phase at gas-liquid interface is in equilibrium with the CO concentration in the gaseous phase, and that the resistance to mass transfer is in the stagnant liquid film, k_{LA} can be determined by Equation (19). The overall volumetric mass transfer coefficient (k_{LA}) is related to time and CO concentration gradient, which is the driving force for mass transfer. The gradient is formed between CO steady-state concentration (C_{CO}^S) and CO concentration in the liquid phase (C_{CO}) at any given time (t). In order to estimate k_{LA} and C_{CO}^S , a hybrid optimization method was performed in MATLAB R2015a combining PSO and Sequential

Quadratic Programming (SQP). Equation (19) was used as the gas-liquid mass transfer mathematical model and Maximum likelihood Method was chosen as objective function, represented in Equation (20).

$$\frac{dC_{CO}}{dt} = k_L a (C_{CO}^s - C_{CO}) \quad (19)$$

Where, $k_L a$ is the overall volumetric mass transfer; C_{CO}^s is the CO steady-state concentration; C_{CO} is the carbon monoxide concentration at liquid phase; t is sampling time.

$$F_{Obj} = \sum_{i=1}^{NE} \sum_{j=1}^{NY} \frac{(y_{ij}^e - y_{ij}^m(x_i, \theta))^2}{\sigma_{ij}^2} \quad (20)$$

Where, F_{Obj} represents the objective function; NE the number of experiments; NY the number of dependent variables; x_i the independent variables; θ the parameters; y_{ij}^e are the experimental values and y_{ij}^m are the predicted values; and σ_{ij}^2 experimental variance.

The optimization problem can be posed as Equation (21):

$$\min_{\theta} F_{Obj}(\mathbf{Y}^e, \mathbf{Y}^m, \mathbf{x}) \quad s. t. \quad \begin{cases} f(\mathbf{Y}^m, \mathbf{x}, \theta) = 0 \\ \theta_l < \theta < \theta_h \end{cases} \quad (21)$$

where, θ is a parameter vector defined by Equation(22); F_{Obj} is the objective function; \mathbf{Y}^e is an experimental values matrix for NE experiments and NY measurements defined by Equation (23); \mathbf{Y}^m is a predicted values matrix for NE experiments and NY measurements defined by Equation (24); \mathbf{x}_i is the independent variable matrix defined by Equation (25); θ_l is the lower bound parameter vector defined by Equation (26); and θ_h is the upper bound parameter vector defined by Equation (27). Table IV.2 summarize all lower and upper bound values used for the present optimization, since it depends on the experimental condition.

$$\theta = [k_L a \quad C_{CO}^s]^T \quad (22)$$

$$\mathbf{Y}^e = \begin{bmatrix} C_{CO,(1,1)}^e & \cdots & C_{CO,(1,NE)}^e \\ \vdots & \ddots & \vdots \\ C_{CO,(NY,1)}^e & \cdots & C_{CO,(NY,NE)}^e \end{bmatrix} \quad (23)$$

$$\mathbf{Y}^m = \begin{bmatrix} C_{CO,(1,1)}^m & \cdots & C_{CO,(1,NE)}^m \\ \vdots & \ddots & \vdots \\ C_{CO,(NY,1)}^m & \cdots & C_{CO,(NY,NE)}^m \end{bmatrix} \quad (24)$$

$$\mathbf{x} = [t_1 \quad \cdots \quad t_{NY}]^T \quad (25)$$

$$\boldsymbol{\theta}_l = [\theta_{l,1} \quad \theta_{l,2}]^T \quad (26)$$

$$\boldsymbol{\theta}_h = [\theta_{h,1} \quad \theta_{h,2}]^T \quad (27)$$

As highlighted before, experimental deviations lead to uncertainty in parameter estimation. Therefore, in order to better evaluate k_{LA} and C_{CO}^S , likelihood confidence regions, parametric correlation and confidence interval were also performed. Equations (11), (12) and (13) describe the mathematical structures used in order to evaluate these regions and correlation. A confidence level (α) of 90% was chosen due to experimental uncertainty and each experiment has its $(NE \cdot NY - NP)$ degrees of freedom. Estimation units for k_{LA} and C_{CO}^S are s^{-1} and μM , respectively.

Table IV.2 Upper and Lower Bound limits for optimization based on operational conditions, liquid phase and temperature (T, °C).

Liquid phase	T (°C)	Lower/Upper Bound
Distilled water	25	$\theta_l = [0 \quad \max(C_{CO}) \cdot 0.4]^T$ $\theta_h = [0.8 \quad 875.09]^T$
Distilled water	37	$\theta_l = [0 \quad \max(C_{CO}) \cdot 0.4]^T$ $\theta_h = [0.8 \quad 719.06]^T$
Water + PFC Water + Tween® 80 Water + PFC + Tween® 80	25	$\theta_l = [0 \quad \max(C_{CO}) \cdot 0.4]^T$ $\theta_h = [0.8 \quad \max(C_{CO})]^T$

Where, T is temperature (°C).

IV.5.1 – PSO algorithm

PSO algorithm is a non-deterministic optimization method developed by Kennedy and Eberhart in 1995 and is presented here according to Schwaab et al. (2008). As explained before, each individual particle will have a best solution for itself and all other particles along the search path. Particles move along the search and exchange information with other particles according to Equations (28) and (29).

$$v_{p,d}^{k+1} = wv_{p,d}^k + c_1r_1(x_{p,d}^{ind} - x_{p,d}^k) + c_2r_2(x_d^{glo} - x_{p,d}^k) \quad (28)$$

$$x_{p,d}^{k+1} = x_{p,d}^k + v_{p,d}^{k+1} \quad (29)$$

where, p denotes particles; d is the search direction; k is the iteration number; v is the velocity/pseudo velocity; x is the particle's position; x^{ind} and x^{glo} are points of the search space where F_{Obj} reaches an optimum value for each particle (ind) and for the whole swarm (glo); r_1 and r_2 are random numbers with uniform distribution in the range [0,1]; w, c_1 and c_2 are search parameters, which c_1 is a cognitial parameter, c_2 is a social parameter and w an inertial weight introduced by Shi and Eberhart (1998).

For the present estimation some parameter values were assumed based on Schwaab et al. (2008) and the current problem are presented below. The total number of experiments conducted and replicates varied for each condition, so each condition had its degrees of freedom.

- $c_1 = 2$;
- $c_2 = 2$;
- $w = 0.9$;
- Number of particles = $N_p = p = 80$;
- Number of iterations = 1000 (Niter);
- Number of parameters (search direction) = $d = 2$ (k_{La} and C_{CO}^S);

Particle Swarm Optimization Algorithm

1. Initialize search parameters:

- a. N_{iter} : number of interactions;
- b. N_p : number of particles;
- c. N_d : number of searched dimensions (number of parameters);
- d. x^{MIN} and x^{MAX} : searching limits vectors (size N_d)
- e. PSO searching parameters: c_1 , c_2 and w .

set $k = 0$

2. Calculate maximum particle velocity along search direction \underline{d} :

$$v_d^{max} = \frac{(x_d^{max} - x_d^{min})}{2} \quad (30)$$

3. Calculate initial particle positions and velocities:

$$x_{p,d}^k = x_d^{min} + r(x_d^{max} - x_d^{min}) \quad (31)$$

$$v_{p,d}^k = v_d^{max}(2r - 1) \quad (32)$$

4. Evaluate objective function for each particle.
5. Write particle positions and objective functions in a file to be used for construction of the confidence region.
6. Update x^{glo} , a vector with dimension N_d that contains the best position found by the world particle swarm.
7. When the maximum number of iteration is achieved, $k = N_{iter}$, the search is terminated.
8. Update x_p^{ind} , a N_p vector with dimension N_d that contains the best position found by each particle of the swarm.
9. Calculate the inertial weight value:

$$w = w_o + (w_f - w_o) \frac{k}{N_{iter}} \quad (33)$$

10. Update the particle velocities for $p = 1 \dots N_p$ and $d = 1 \dots N_d$ using Equation (28).

11. If the absolute particle velocity is higher than the maximum permitted value (v_d^{max}),

then:

$$v_{p,d}^{k+1} = v_d^{max} \text{sign}(v_{p,d}^{k+1}) \quad (34)$$

12. Update the particle position:

$$x_{p,d}^{k+1} = x_{p,d}^k + v_{p,d}^k \quad (35)$$

13. If the particle position is no inside the searching limits, the particle is placed at the violated searching limit.

14. Add an iteration to k ($k = k+1$) and return to step 4.

Chapter V. RESULTS AND DISCUSSION

In this chapter, results for the overall volumetric mass transfer coefficient ($k_{L,a}$) and carbon monoxide steady-state concentration (C_{CO}^S) estimated values will be presented for different agitation speeds, specific gas flow rates, and liquid phases composition: pure distilled water; distilled water and PFC; distilled water and Tween® 80; distilled water, PFC and Tween® 80. Relevant figures will be added in order to illustrate discussion but all graphic results are presented in Appendix chapter.

V.1 – The Myoglobin-Protein Bioassay

The determination of carbon monoxide concentration in liquid phase can be challenging due to the absence of probes (KADIC and HEINDEL, 2014). However, as stated before, carbon monoxide concentration has been determined by both myoglobin-protein bioassay and gas chromatography (GC) in literature, presenting equivalent results (MUNASINGHE and KHANAL, 2014). Therefore, since myoglobin bioassay is faster, cheaper and simpler than GC methodology, the method was performed in laboratory with some adaptations to the original reference (KUNDU et al., 2006; KADIC and HEINDEL, 2014) but without interference to the technique.

Experimental uncertainty is present in many steps during myoglobin bioassay and, consequently, care must be taken to assure the measurement is correct. Ensuring that oxygen cannot be bound to myoglobin molecule is extremely important during this assay and care must be taken concerning small gas bubbles that can be trapped inside the syringe and can influence measurement negatively (KADIC and HEINDEL, 2014). Temperature is also a very important factor in myoglobin solution preparation, and exposure to room temperature should be minimized as much as possible since myoglobin can be degraded at this condition (KADIC and HEINDEL,

2014). Consequently, it is extremely important to prepare the test solution as soon as the myoglobin solution is thawed. Moreover, due to small volumes used throughout the assay, care must be taken during pipetting in order to avoid mistakes during sample dilution or sampling, which can impact directly carbon monoxide determination (RIGGS and HEINDEL, 2006). This was especially observed during test solution preparation and “oxi” spectrum reading.

The complex myoglobin-oxygen (MbO_2) solution, represented by the “oxi” spectrum, is prepared through repetitive additions of myoglobin solution into phosphate buffer until an absorbance peak of approximately 1.5 is reached at 409 nm. The “oxi” spectrum maximum absorbance peak is used to determine myoglobin concentration in its stock solution. On the other hand, test solution preparation included a mixture of myoglobin solution with a certain volume previously determined in “oxi” spectrum” and phosphate buffer. Consequently, the myoglobin addition techniques were different for both solutions and this can impact the myoglobin concentration transferred to the solution.

In order to understand how this could affect carbon monoxide determination, two different MbO_2 solutions were prepared and a spectrum was obtained for each one. The results are illustrated in Figure V.1. The MbO_2 solution used to obtain the “oxi” spectrum was set using the classical technique explained in Chapter IV, item IV.4.2. The MbO_2 solution used to obtain the “oxiTS” spectrum was prepared by transferring to a PS cuvette 1.0 mL of phosphate buffer and 5.0 μL of myoglobin solution ($\text{DR} = 5$), which is the volume amount necessary to reach a maximum absorbance peak of 1.5 (Chapter IV, item IV.4.4).

Although both spectra account for a solution where all myoglobin are bounded to oxygen, there is a clear difference between absorbance peaks. Experimental error in pipetting is high due to operator and instrument error, which affects accuracy in the procedure. Since absorbance peaks

are different, myoglobin concentration is not the same for both solutions, even though both reached or passed the technique recommended absorbance peak (1.5). The maximum absorbance peaks were 2.025 for “oxi” spectrum solution and 1.718 for “oxiTS” spectrum solution, which represents a myoglobin concentration of 10.77 μM and 9.14 μM , respectively. As carbon monoxide concentration in liquid phase depends directly of myoglobin concentration, as demonstrated in Equation (18), this 15% difference between absorbance peaks can impact k_{LA} and C_{CO}^{S} estimation. As test solution is used to make “deoxi”, “carboxi” and “sample” spectra solutions, “oxiTS” spectrum was used to determine myoglobin concentration in test solution in order to decrease deviation impact in the estimation.

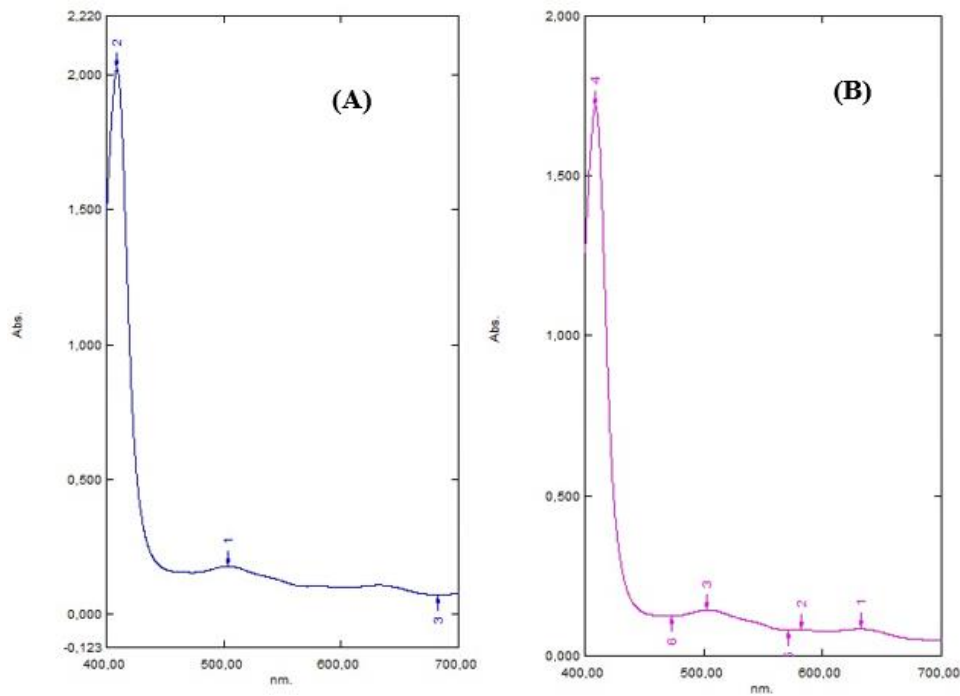


Figure V.1 Difference between two myoglobin-oxygen spectra: “oxi” (A) and “oxiTS” (B).

V.2 – Pure Distilled Water Liquid Phase in k_{LA} and C_{CO}^S Estimation

Most works presented in literature use tap water at 25 °C as liquid phase in order to calculate carbon monoxide concentration and determine k_{LA} and C_{CO}^S (KAPIC et al., 2006; MUNASINGHE and KHANAL, 2012; MUNASINGHE and KHANAL, 2014; RIGGS and HEINDEL, 2006; SHEN et al., 2014; UNGERMAN and HEINDEL, 2007). For the present work, distilled water was chosen since laboratory tap water's quality could compromise myoglobin structure. Therefore, in order to compare the estimated values obtained with literature and guarantee a good performance of the bioassay, this dissertation first approach involved different impeller agitation speed, specific gas flow rates and liquid volumes using pure distilled water as primary liquid phase at 25°C.

Table V.1 displays the estimated values for k_{LA} and C_{CO}^S in STR using 0.75 L pure distilled water as liquid phase at 25 °C. These values were used to evaluate how agitation speed (100, 300 and 500 rpm) and specific gas flow rate (0.7, 1.3 and 2.7 vvm) influenced the overall volumetric mass transfer coefficient and the carbon monoxide steady-state concentration. STR was operated with a water recirculation line at peristaltic pump maximum liquid pumping rate (65.26 mL/min), where the sampling port was placed (RIGGS and HEINDEL, 2006). This recirculation line promoted a better mixing in STR and also simplified sampling procedure. Reynolds and Froude number were calculated only for water at 25 °C and 37 °C. These dimensionless numbers were not calculated for the other liquid phases due to the lack of information about dynamic viscosity and density for these liquid mixtures. However, estimation of these physical properties are strongly encouraged for future work in order to complete hydrodynamics discussion for these systems.

Table V.1 Results of Re , Fr , k_{La} , C_{CO}^s , and its confidence intervals (CI) obtained at different agitation speed (N) and specific gas flow rate (Q_{CO}) for carbon monoxide in 0.75 L of pure distilled water at 25 °C and 65.26 mL/min recirculated liquid flow.

N (rpm)	Re	Fr	Q_{CO} (vvm)	k_{La} ± CI (h⁻¹)	C_{CO}^s ± CI (μM)
100	3.62x10 ³	0.01	0.7	18.87 ± 0.79	358.23 ± 11.60
100	3.62x10 ³	0.01	1.3	27.11 ± 4.38	693.41 ± 78.16
100	3.62x10 ³	0.01	2.7	56.07 ± 1.57	716.71 ± 10.05
300	1.09x10 ⁴	0.11	0.7	58.59 ± 1.79	473.29 ± 3.57
300	1.09x10 ⁴	0.11	1.3	80.90 ± 18.91	547.51 ± 43.98
300	1.09x10 ⁴	0.11	2.7	166.11 ± 16.37	647.08 ± 4.55
500	1.81x10 ⁴	0.31	0.7	59.04 ± 9.26	562.08 ± 29.71
500	1.81x10 ⁴	0.31	1.3	149.16 ± 12.46	602.28 ± 10.99
500	1.81x10 ⁴	0.31	2.7	399.06 ± 18.25	743.27 ± 3.62

Where, N is the agitation speed (in rpm); Re is the Reynolds number; Fr is the Froude number; Q_{CO} is the specific gas flow rate (in vvm); k_{La} is the overall volumetric mass transfer coefficient (in h⁻¹); CI is the confidence interval; and C_{CO}^s is the CO steady-state concentration (in μM).

Concerning 100 rpm agitation speed, it is not possible to affirm that the only resistance to mass transfer is in the liquid stagnant film. Reynolds number is below 10⁴ indicating a transient flow in agitated vessels (BORZANI et al., 2001). Therefore, resistance in liquid bulk cannot be overlooked and the model for mass transfer and its resistances should be revised. All Froude number indicate that the flow is subcritical ($Fr < 1$) at this temperature.

When operated at 0.75 L, the upper impeller (Rushton) was barely accessed since it stayed at the edge of the liquid phase. It is possible, however, to observe that the efficiency of Smith-type impeller in decreasing bubble size and increasing k_{La} (KADIC and HEINDEL, 2014). For a same agitation speed, k_{La} estimated values increased with specific gas flow rate increase. From 0.7 to 2.7 vvm, k_{La} enhanced 2.97 times, 2.83 times and 6.76 times comparing 100, 300 and 500 rpm, respectively. This is directly related to carbon monoxide molecule availability in liquid phase due to higher gas flow, which increases gas molecules in the system. Considering a same specific gas flow rate, k_{La} increased with agitation speed. From 300 to 500 rpm, k_{La} enhanced 1.84 times and

2.40 times for specific gas flow rates of 1.3 and 2.7 vvm, respectively. However, at a lower specific gas flow rate (0.7 vvm), k_{La} for 300 and 500 rpm were the same. Mass transfer efficiency is a balance between agitation speed and gas flow rate. Therefore, further increasing agitation speed at 0.7 vvm would probably lead to voids and recirculation loops in the reactor (Figure III.5-E), impairing gas dispersion and mass transfer (KADIC and HEINDEL, 2014) mass transfer coefficients for 300 and 500 rpm at 0.7 vvm were the same. Increasing impeller agitation speed promotes not only a better mixing in liquid phase but also an increase in gas superficial area, which enhances mass transfer directly.

Further increasing agitation speed could be tempting but not only power consumption would increase but impeller efficiency would decrease due to the formation of large cavities at the impeller back (KADIC and HEINDEL, 2014). Moreover, it should be noted that some agitation speeds can cause shear stress in microorganisms, decreasing cell viability and, consequently, productivity (BORZANI et al., 2001).

It should be considered that the estimated value for carbon monoxide steady-state concentration did not reach CO maximum solubility in water at 25 °C, 875.09 μM (PENNEY, 2002). During k_{La} experiments, gas saturation should be close to standard saturation values but, most of the time, these values are similar but not exactly the same. Figure V.2 display CO concentration variation with time in a 0.75 L pure distilled water at 25 °C, 300 rpm and 1.3 vvm. According to these results, CO concentration does not reach the steady-state during the assay. The same was observed for pure distilled water at 300 rpm and 500 rpm at lower specific gas flow rate (0.7 vvm). Therefore, these experiments should be conducted for longer periods of time until a steady-state is reached.

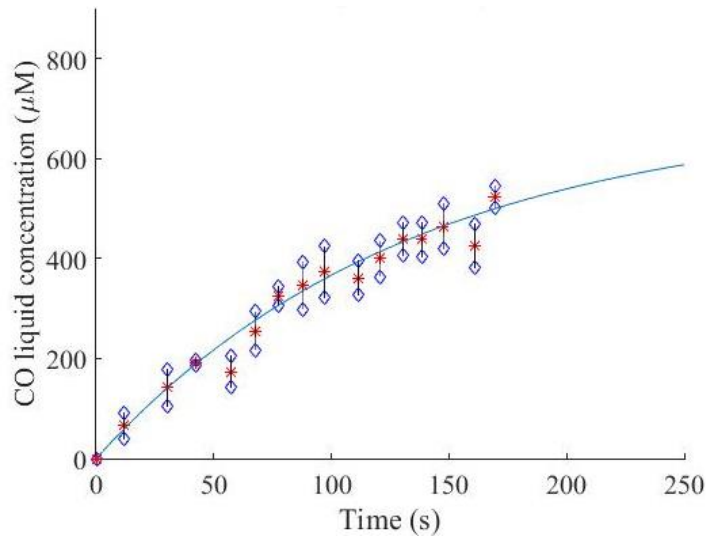


Figure V.2 Model prediction for pure distilled water at 25 °C, 100 rpm and 1.3 vvm.

It can be seen in Table V.1 that at lower specific gas flow rates, agitation speed alone cannot increase mass transfer, which indicated that flow behaviour is not only imposed by the impeller but also by gas velocity. As specific gas flow rate was increased, C_{CO}^S estimated value also increased, reaching closer to maximum solubility limit. Therefore, an increase in gas velocity promoted a better mixing in the liquid bulk, increasing mass transfer.

In order to fully access both Smith and Rushton impellers, the liquid volume was increased to 1.0 L and k_{LA} results for 500 rpm and different specific gas flow rates are shown in Table V.2. Due to a limitation in the rotameter it was not possible to produce results with a 2.7 vvm specific gas flow rate (2.7 L/min gas flow), therefore Q_{CO} used was 2.0 vvm (2.0 L/min gas flow) and 2.5 vvm (2.5 L/min gas flow, maximum limit in rotameter). The overall volumetric mass transfer coefficient for 500 rpm and 2.0 vvm is lower than 500 rpm and 2.7 vvm (Table V.1, 399.06 h⁻¹) due to the lower specific gas flow rate. Increasing liquid volume and maintaining gas flow rate reduces the amount of molecules per unit of volume or the specific gas flow rate, therefore reducing k_{LA} .

These results show that increasing specific gas flow rate from 0.7 to 2.7 vvm, at the same agitation speed (500 rpm), enhanced CO mass transfer to liquid bulk because gas velocity increase would enhance mixing in the bioreactor. This indicates that not only agitation speed but specific gas flow rate is important for mass transfer in liquid phase. However, the same behaviour was not observed for 500 rpm and 2.0 vvm, which presented a lower value compare to 500 rpm and 1.3 vvm (Table V.1, 149.16 h⁻¹). This experiment was conducted in duplicate, so number of experiments may have impacted the accurate estimation of parameter value.

Table V.2 Results of Re, Fr, k_{LA}, C_{CO}^S, and its confidence intervals (CI) obtained at different specific gas flow rate (Q_{CO}) for carbon monoxide in 1.0 L of pure distilled water at 25 °C, 500 rpm and 65.26 mL/min recirculated liquid flow.

N (rpm)	Re	Fr	Q_{CO} (vvm)	k_{LA} ± CI (h⁻¹)	C_{CO}^S ± CI (μM)
500	1.81x10 ⁴	0.31	2.0	111.48 ± 58.97	531.86 ± 50.53
500	1.81x10 ⁴	0.31	2.5	226.79 ± 26.86	609.96 ± 11.48

Where, N is the agitation speed (in rpm); Re is the Reynolds number; Fr is the Froude number; Q_{CO} is the specific gas flow rate (in vvm); k_{LA} is the overall volumetric mass transfer coefficient (in h⁻¹); CI is the confidence interval; and C_{CO}^S in the CO steady-state concentration (in μM).

Synthesis gas fermentation is conducted at bacteria optimum temperature, 37 °C, in which carbon monoxide solubility in water is decreased (719.06 μM). Therefore, k_{LA} and C_{CO}^S were estimated at this temperature, 300 and 500 rpm, and 2.7 vvm. Results are summarized in Table V.3. The overall volumetric mass transfer coefficient was 24% lower for 300 rpm, 37°C compared to 25°C; and 75% lower comparing 500 rpm, 25° C to 37° C. Although some experimental deviation should be considered, due to low gas solubility at 37 °C and high agitation speed (500 rpm), carbon monoxide bubbles would migrate more to the gas phase headspace (0.75 L), which would decrease carbon monoxide transfer to the liquid bulk.

Table V.3 Results of Re, Fr, k_{LA} , C_{CO}^S , and its confidence interval (CI) obtained at different agitation speed (N) for carbon monoxide in 0.75 L of pure distilled water at 37 °C, 2.7 vvm specific gas flow rate and 65.26 mL/min recirculated liquid flow.

N (rpm)	Re	Fr	Q_{co} (vvm)	k_{LA} ± CI (h⁻¹)	C_{CO}^S ± CI (μM)
300	1.09x10 ⁴	0.11	2.7	126.08 ± 9.44	609.55 ± 15.33
500	1.81x10 ⁴	0.31	2.7	98.15 ± 8.62	679.00 ± 14.09

Where, N is the agitation speed (in rpm); Re is the Reynolds number; and Fr is the Froude number; Q_{co} is the specific gas flow rate (in vvm); k_{LA} is the overall volumetric mass transfer coefficient (in h⁻¹); CI is the confidence interval; and C_{CO}^S is the CO steady-state concentration (in μM).

Another fact that leads to an increase in overall volumetric mass transfer coefficient is bioreactor configuration of the present work. This stirred tank reactor is operated with a dual impeller configuration: a six-bladed Smith-type and a six-bladed Rushton-type, both radial flow impellers. A dual impeller configuration already improved k_{LA} in a stirred tank reactor tested alternating two different axial flow impellers (Rushton-type and Philadelphia Mixing concave turbine) and six different radial flow impellers (Philadelphia Mixing pitched blade turbine, Lightnin A315 fluid foil, Lightnin A310 and Philadelphia Mixing LS hydrofoil) (UNGERMAN and HEINDEL, 2007).

Although Rushton-type impellers are the most used in gas-liquid system, standard Rushton-type can add a higher shear stress around the impeller, a power draw drop upon gassing, an energy dissipation not uniformly distributed and a low gas hold up near the bottom of the tank (BAKKER and VAN DER AKKER, 1994). Concave impeller, such as Smith-type, promotes a higher gas dispersion in comparison to Rushton-Type and can result in higher k_{LA} values at high gas flow rates (UNGERMAN and HEINDEL, 2007). Ungerman and Heindel (2017) concluded that mass transfer increases with gas flow rate but its magnitude depends on the impeller scheme. For a stirred tank with dual impeller Rushton-Type at 400 rpm agitation speed and 2.14 vvm

specific gas flow rate, the researchers achieved a k_{LA} of 153 h^{-1} (Table III.1, reference 2). A k_{LA} of 399.06 h^{-1} was obtained in the present study at 500 rpm agitation speed, 2.7 vvm specific gas flow rate and 0.75 L working volume (Table V.1) using a dual impeller configuration combining a Rushton-type and a Smith-type impellers. As the present data available in Table V.1 and Table V.2 show, the concave impeller has its mass transfer capability enhanced with the increase in gas flow rate (UNGERMAN and HEINDEL, 2007). Also, the diameter of the holes present in the topside of the perforated ring sparger produced small bubbles, which also increases the volumetric mass transfer.

V.3 – PFC Influence in Distilled Water for k_{LA} and C_{CO}^S Estimation

PFC was responsible for increasing oxygen uptake and mass transfer to liquid phases in aerobic systems (AMARAL et al., 2006; AMARAL et al., 2008; CHO and WANG, 1988; ELIBOL, 1996; ELIBOL, 1997; ELIBOL AND MAVITUNA, 1995; JU and LEE, 1991; JUNKER et al., 1990; MCMILLAN and WANG, 1987; TURICK and BULMER, 1998; WASANASATHIAN and PENG, 2001). Therefore, since carbon monoxide solubility to PFC is higher than to water (CABRALES et al., 2007), values for k_{LA} and carbon monoxide steady-state concentration were estimated for distilled water and PFC mixture. Results for 300 and 500 rpm agitation speeds, 25°C, 0.75 and 1.0 L working volume and different specific gas flow rate are summarized in Table V.4.

In comparison to pure distilled water (Table V.1 and Table V.2), k_{LA} for distilled water and PFC does not increase with specific gas flow rate and its values are lower than k_{LA} for pure distilled water at 500 and 300 rpm, 2.7 vvm. Overall volumetric mass transfer coefficient for distilled water and PFC is almost the same for 300 rpm and 500 rpm at 2.7 vvm. Moreover, values for these

conditions were below k_{LA} obtained for same agitation speeds and specific gas flow rate, considering pure distilled water as liquid phase. It was observed that distilled water and PFC mixture was not homogenous as it should be (detected visually), with PFC being at the bottom of the reactor. This probably offered a resistance for carbon monoxide transfer to the water phase due to its absorption in the PFC phase. Perfluorodecalin has a low solubility in water so, in order to increase carbon monoxide transfer to the liquid phase both PFC and water have to be well mixed (AMARAL et al., 2008).

Table V.4 Results of k_{LA} , C_{CO}^s and its confidence interval (CI) obtained for different reactor volume (V), agitation speed (N) and specific gas flow rate (Q_{CO}) for carbon monoxide in a liquid mixture distilled water and PFC at 25 °C and 65.26 mL/min recirculated liquid flow.

V (L)	N (rpm)	Q_{CO} (vvm)	$k_{LA} \pm CI$ (h^{-1})	$C_{CO}^s \pm CI$ (μM)
1.00	500	2.0	134.18 ± 12.18	502.36 ± 5.60
1.00	500	2.5	153.52 ± 13.08	493.79 ± 7.42
0.75	500	2.7	86.28 ± 8.86	583.97 ± 28.25
0.75	300	2.7	90.06 ± 24.90	470.36 ± 9.33

Where, V is the reactor volume (in L); N is the agitation speed (in rpm); Q_{CO} is the specific gas flow rate (in vvm); k_{LA} is the overall volumetric mass transfer coefficient (in h^{-1}); CI is the confidence interval; and C_{CO}^s is the CO steady-state concentration (in μM).

Therefore, in order to increase system mixing, bioreactor working volume was increased from 0.75 L to 1.00 L to cover the upper impeller, which was at the edge of the liquid when 0.75 L of working volume was used. The agitation speed was 500 rpm, for which a higher k_{LA} was obtained in comparison to 300 rpm in pure distilled water. According to Table V.4, however, k_{LA} did not improve with PFC and water mixture (2.0 and 2.5 vvm) in comparison to pure distilled water at the same conditions (Table V.2, 2.0 and 2.5 vvm at 500 rpm). Although the increase in working volume did not favour CO transfer to the liquid phase, it promoted a better dispersion of

PFC in water (detected visually), which is essential for the dissociation of molecules from the PFC to the aqueous phase.

The capture of gaseous molecules to the PFC is facilitated because it has a higher solubility for several molecules (ex. CO₂ and O₂) than water (LOWE et al., 1998). Nonetheless, the transfer from PFC to the aqueous phase needs a huge transfer area, which is accomplished when droplets of PFC are present in water rather than at the bottom of the reactor. Therefore, in the presence of PFC and at 500 rpm, an increase in k_{La} was observed when the working volume was increased, even at lower specific gas flow rate: comparing 0.75 L and 2.7 vvm to 1.0 L and 2.0 vvm (Table V.4), 64%; and comparing 0.75 L and 2.7 vvm to 1.0 L and 2.5 vvm, 56% (Table V.4).

Comparing to pure water at 500 rpm and 2.0 vvm (Table V.2), k_{La} for PFC and water mixture at the same conditions was slightly higher. The increase in bioreactor volume allowed a slightly increase of PFC mixing in distilled water, which marginally increased CO mass transfer from PFC to aqueous phase. However, when increasing specific gas flow rate (2.5 vvm), there was no expressive increase in volumetric mass transfer probably due to the interface area of large PFC droplets in water that, in this case (of higher specific gas flow rate) was not big enough to transfer more CO molecules.

V.4 – Tween® 80 Influence in k_{La} and C_{CO}^S Estimation for Mixtures with Distilled Water, and Distilled Water and PFC

Tween® 80 was added to liquid phase in order to increase PFC dispersion, reducing its droplets, and enhance carbon monoxide transfer to distilled water. Therefore, two approaches were performed. First, CO mass transfer was analysed in distilled water and Tween® 80 mixture and then in distilled water, PFC and Tween® 80 mixture. The experiments were conducted at 25 °C,

0.75 L and 1 L, and 300 rpm and 500 rpm in order to compare Tween® 80's effect in increasing k_{LA} , alone and in a mixture with PFC. Results are summarized in Table V.5 for distilled water and Tween® 80 mixture and Table V.6 for distilled water, PFC and Tween® 80 mixture.

Tween® 80 was responsible for increasing k_{LA} at all reactor volumes and specific gas flow rates, even without PFC. Compared to k_{LA} results from pure distilled water (Table V.1 and Table V.2), mixing Tween® 80 in water (Table V.5) increased k_{LA} in 59% (500 rpm, 2.0 vvm), 20% (500 rpm, 2.5 vvm), 28% (500 rpm, 2.7 vvm) and 2 times (300 rpm, 2.7 vvm). Tween® 80 has both hydrophobic and hydrophilic character, being able to reduce gas bubbles and avoid coalescence between them (WUELFING et al., 2006), which increases CO transfer area favouring k_{LA} . Moreover it was observed that Tween® 80 is not a resistance for CO mass transfer to water due to k_{LA} increase. Mass transfer increased with specific gas flow rate at 500 rpm and with agitation speed at 2.7 vvm, the same behaviour observed for pure distilled water at the same conditions. This pattern was also observed in distilled water mixed with PFC and Tween® 80, displayed in Table V.6.

Table V.5 Results of k_{LA} , C_{CO}^S and its confidence interval (CI) obtained at different reactor volume (V), agitation speed (N) and specific gas flow rate (Q_{CO}) for carbon monoxide in a mixture of distilled water and Tween® 80 at 25 °C and 65.26 mL/min recirculated liquid flow

V (L)	N (rpm)	Q_{CO} (vvm)	$k_{LA} \pm CI$ (h^{-1})	$C_{CO}^S \pm CI$ (μM)
1.00	500	2.0	177.43 ± 39.64	719.82 ± 28.12
1.00	500	2.5	272.56 ± 20.18	669.46 ± 4.72
0.75	500	2.7	512.59 ± 75.67	629.86 ± 14.88
0.75	300	2.7	370.25 ± 102.07	602.53 ± 11.16

Where, V is the reactor volume (in L); N is the agitation speed (in rpm); Q_{CO} is the specific gas flow rate (in vvm); k_{LA} is the overall volumetric mass transfer coefficient (in h^{-1}); CI is the confidence interval; and C_{CO}^S is the CO steady-state concentration (in μM).

When added to the mixture of distilled water and Tween® 80, PFC dispersion was increased forming a white coloured liquid, presented in Figure V.3. Comparing to water and PFC mixture at 500 rpm and 2.7 vvm, k_{La} was enhanced 7 times when Tween® 80 was added to the mixture, and carbon monoxide steady-state concentration enhanced 31%. Comparing to pure distilled water at 500 rpm and 2.7 vvm, k_{La} was enhanced 51% but carbon monoxide steady-state concentration did not change considerably (3%). Considering 500 rpm and 2.0 vvm, 1.0 mL working volume and PFC well dispersed by Tween® 80, a k_{La} 3 times higher than for pure distilled water was achieved, while Tween® 80 alone increased the transfer rate 59%.



Figure V.3 Water, PFC and Tween® 80 emulsion prepared with ULTRA-TURRAX® (left) and in the STR (right).

Carbon monoxide steady-state concentration for distilled water and PFC; distilled water and Tween® 80; and distilled water, PFC and Tween® 80, are not available in literature. Although values of C_{CO}^S for distilled water mixed with Tween® 80 and for distilled water mixed with PFC were close, the same was not true for distilled water mixed with PFC and Tween® 80, probably due to the high amount of experimental deviation. The following section will approach the data statistical analysis in order to demonstrate how this experimental deviation affects the estimation.

Table V.6 Results of k_{LA} , C_{CO}^s and its confidence interval (CI) obtained at different reactor volume (V), agitation speed (N) and specific gas flow rate (Q_{CO}) for carbon monoxide in a liquid mixture composed of distilled water, PFC and Tween® 80 liquid mixture at 25 °C and 65.26 mL/min recirculated liquid flow,

V (L)	N (rpm)	Q_{CO} (vvm)	$k_{LA} \pm CI$ (h^{-1})	$C_{CO}^s \pm CI$ (μM)
1.00	500	2.0	346.74 ± 73.63	465.65 ± 8.70
1.00	500	2.5	371.75 ± 91.06	831.66 ± 24.00
0.75	500	2.7	603.49 ± 445.07	767.36 ± 28.29
0.75	300	2.7	377.70 ± 69.67	531.68 ± 24.61

Where, V is the reactor volume (in L); N is the agitation speed (in rpm); Q_{CO} is the specific gas flow rate (in vvm); k_{LA} is the overall volumetric mass transfer coefficient (in h^{-1}); CI is the confidence interval; and C_{CO}^s is the CO steady-state concentration (in μM).

The highest overall volumetric mass transfer coefficient obtained in the present work for CO in distilled water at 25 °C at 500 rpm and 2.7 vvm was $399.06 \pm 18.07 h^{-1}$. Considering water as liquid phase, this k_{LA} is the higher obtained so far in literature for STR (BREDWELL et al., 1999; KAPIC et al., 2006; RIGGS and HEINDEL, 2006; UNGERMAN and HEINDEL, 2007; YOUNESI et al., 2008). Kapic et al. (2006) and the present work achieved a similar k_{LA} for 500 rpm and a similar specific gas flow rate (1.07 – KAPIC et al, 2006, and 1.3 – present work), $144.0 h^{-1}$ and $149.16 h^{-1}$, respectively. The main difference between both works are the bioreactor configuration, in which Kapic et al. (2006) used a Rushton-type impeller and four baffles. The STR in the present work does not have any baffles, which would promote an even better mixing and increase mass transfer (KADIC and HEINDEL, 2014). Moreover, the use of a distilled water, PFC and Tween® 80 mixture not only increased k_{LA} in comparison to pure distilled water ($603.49 h^{-1}$ compared to $399.06 h^{-1}$) but also achieved the highest k_{LA} for stirred tank bioreactors reported in literature. So far, only membrane bioreactors presented a higher overall volumetric mass transfer rate (MUNASINGHE and KHANAL, 2012; SHEN et al., 2014a).

V.5 – Statistical Analysis of Estimated Values

Although it is expressed emphatically in literature that myoglobin bioassay is a technique prone to many sources of experimental uncertainty (KADIC and HEINDEL, 2014), maximum likelihood was not considered as a parameter estimation method for k_{LA} and C_{CO}^S . Alongside MLE, the present work also performed a least squares routine to determine k_{LA} . However results were statistically irrelevant, as well as physically improbable, when compared to MLE results. Therefore, MLE method and a hybrid optimization were performed in order to obtain k_{LA} and C_{CO}^S as well as confidence regions and intervals. Parametric correlation was also calculated.

In order to appropriately estimate k_{LA} and C_{CO}^S some important remarks about the system behaviour were considered. For example, negative values for k_{LA} and carbon monoxide steady-state concentration are prohibitive since it is physically unfeasible. Therefore, zero is the lower limit for all parameters. The upper bound for CO steady-state concentration are not arbitrary, also. It is based on carbon monoxide maximum solubility in water at a given temperature. At 25 °C and 37 °C, carbon monoxide solubility in water is 24.5 mg/L and 20.15 mg/L respectively (PENNEY, 2002). This solubility corresponds to a steady-state concentration of 875.09 μ M (25 °C) and 719.06 μ M (37 °C). However, since carbon monoxide solubility in distilled water and PFC mixture, distilled water and Tween® 80 mixture; and distilled water, PFC and Tween® 80 mixtures are not available in literature, the maximum carbon monoxide concentration value for each experiment was considered the upper bound for carbon monoxide steady-state concentration in these liquid mixtures.

Table V.7 to Table V.11 summarizes all k_{LA} and C_{CO}^S estimated values for each condition studied, as well as the parametric correlation between k_{LA} and C_{CO}^S , its confidence intervals and minimum objective function value for PSO and Deterministic Optimization. In order to illustrate

this discussion, a few confidence regions and model prediction graphics were selected for explanation. All graphic obtained for the present work are present in the appendix chapter.

Hybrid optimization strategy consisted of performing a PSO method using Maximum Likelihood as objective function for 1000 iterations and 80 particles. The resulting k_{LA} and C_{CO}^S were used as initial guess for a derivative method, which resulted in the estimated parameters values presented in this work. Likelihood regions, confidence intervals and parametric correlation were obtained based on these methods. From Table V.7 to Table V.11, it can be observed the same or similar objective function values for PSO ($F_{Obj} - PSO$) and deterministic optimization ($F_{Obj} - D.O$). This happened due to the high number of iterations and particles chose for PSO, which increase the likelihood of finding a minimum.

Table V.7 Results of k_{LA} and C_{CO}^S alongside its confidence intervals, parametric correlation and objective function values at different agitation speed (N) and specific gas flow rate (Q_{CO}) for carbon monoxide in 0.75 L and 1.0 L of pure distilled water at 25 °C and 65.26 mL/min recirculated liquid flow.

N (rpm)	Q_{CO} (vvm)	$k_{LA} \pm CI$ (h^{-1})	$C_{CO}^S \pm CI$ (μM)	ρ	$F_{Obj-PSO}$	$F_{Obj-D.O}$
100	0.7	18.87±0.79	358.23±11.60	-0.9965	571.4370	571.2350
100	1.3	27.11±4.38	693.41±78.16	-0.9793	25.6312	25.6311
100	2.7	56.07±1.57	716.71±10.05	-0.8727	69.3040	69.3038
300	0.7	58.59±1.79	473.29±3.57	-0.8685	180.8064	180.7972
300	1.3	80.90±18.91	547.51±43.98	-0.8166	39.9407	39.9407
300	2.7	166.11±16.37	647.08±4.55	-0.4236	89.2647	89.2646
500	0.7	59.04±9.26	562.08±29.71	-0.9198	62.4673	62.4665
500	1.3	149.16±12.46	602.28±10.99	-0.5534	48.2534	48.2527
500	2.0	111.48±58.97	531.86±50.53	-0.6273	18.8608	18.8608
500	2.5	226.79±26.86	609.96±11.48	-0.2522	38.2703	38.2702
500	2.7	399.06±18.25	743.27±3.62	-0.3616	55.3834	55.3833

Where, N is the agitation speed (in rpm); Q_{CO} is the specific gas flow rate (in vvm); k_{LA} is the overall volumetric mass transfer coefficient with its confidence interval (in h^{-1}); C_{CO}^S is the CO steady-state concentration with its confidence interval (in μM); CI is the confidence interval; ρ is the parametric correlation; $F_{Obj-PSO}$ is the objective function minimum value obtained in PSO; and $F_{Obj-D.O}$ is the objective function minimum value obtained through deterministic optimization.

Table V.8 Results of $k_{L,a}$ and C_{CO}^s alongside its confidence intervals, parametric correlation and objective function values at different agitation speed (N) for carbon monoxide in 0.75 L pure distilled water at 37 °C, 2.7 vvm specific gas flow rate and 65.26 mL/min recirculated liquid flow.

N (rpm)	Q_{CO} (vvm)	k_{La}±CI (h⁻¹)	C_{CO}^s ± CI (μM)	ρ	F_{Obj} – PSO	F_{Obj} – D.O
300	2.7	126.08±9.44	609.55±15.33	-0.8292	38.5014	38.5013
500	2.7	98.15±8.62	679.00±14.09	-0.9694	52.0885	52.0873

Where, N is the agitation speed (in rpm); Q_{CO} is the specific gas flow rate (in vvm); k_{La} is the overall volumetric mass transfer coefficient with its confidence interval (in h⁻¹); C_{CO}^s is the CO steady-state concentration with its confidence interval (in μM); CI is the confidence interval; ρ is the parametric correlation; F_{Obj}-PSO is the objective function minimum value obtained in PSO; and F_{Obj}-D.O is the objective function minimum value obtained through deterministic optimization.

Table V.9 Results of $k_{L,a}$ and C_{CO}^s alongside its confidence intervals, parametric correlation and objective function values at different agitation speed (N) and specific gas flow rate (Q_{CO}) for carbon monoxide in liquid mixture composed of distilled water and PFC at 25 °C and 65.26 mL/min recirculated liquid flow.

N (rpm)	Q_{CO} (vvm)	k_{La}±CI (h⁻¹)	C_{CO}^s ± CI (μM)	ρ	F_{Obj} – PSO	F_{Obj} – D.O
500	2.0	134.18±12.18	502.36±5.60	-0.4988	57.8123	57.8121
500	2.5	153.52±13.08	493.79±7.42	-0.6294	51.6489	51.6482
500	2.7	86.28±8.86	583.97±28.25	-0.9982	96.0778	96.0733
300	2.7	90.06±24.90	470.36±9.33	-0.3598	34.1995	34.1993

Where, N is the agitation speed (in rpm); Q_{CO} is the specific gas flow rate (in vvm); k_{La} is the overall volumetric mass transfer coefficient with its confidence interval (in h⁻¹); C_{CO}^s is the CO steady-state concentration with its confidence interval (in μM); CI is the confidence interval; ρ is the parametric correlation; F_{Obj}-PSO is the objective function minimum value obtained in PSO; and F_{Obj}-D.O is the objective function minimum value obtained through deterministic optimization.

Table V.10 Results of k_{La} and C_{CO}^s alongside its confidence intervals, as well as parametric correlation and objective function values at different agitation speed (N) and specific gas flow rate (Q_{CO}) for carbon monoxide in a liquid mixture composed of distilled water and Tween® 80 at 25 °C and 65.26 mL/min recirculated liquid flow.

N (rpm)	Q_{CO} (vvm)	$k_{La} \pm CI$ (h^{-1})	$C_{CO}^s \pm CI$ (μM)	ρ	$F_{Obj} - PSO$	$F_{Obj} - D.O$
500	2.0	177.43±39.64	719.82±28.12	-0.8323	42.8305	42.8305
500	2.5	272.56±20.18	669.46±4.72	-0.1076	105.9809	105.9792
500	2.7	512.59±75.67	629.86±14.88	-0.5066	39.0300	39.0300
300	2.7	370.25±102.07	602.53±11.16	-0.3023	49.5023	49.5023

Where, N is the agitation speed (in rpm); Q_{CO} is the specific gas flow rate (in vvm); k_{La} is the overall volumetric mass transfer coefficient with its confidence interval (in h^{-1}); C_{CO}^s is the CO steady-state concentration with its confidence interval (in μM); CI is the confidence interval; ρ is the parametric correlation; $F_{Obj-PSO}$ is the objective function minimum value obtained in PSO; and $F_{Obj-D.O}$ is the objective function minimum value obtained through deterministic optimization.

Table V.11 Results of k_{La} and C_{CO}^s alongside its confidence intervals, as well as parametric correlation and objective function values at different agitation speed (N) and specific gas flow rate (Q_{CO}) for carbon monoxide in a liquid mixture composed of distilled water, PFC and Tween® 80 at 25 °C and 65.26 mL/min recirculated liquid flow.

N (rpm)	Q_{CO} (vvm)	$k_{La} \pm CI$ (h^{-1})	$C_{CO}^s \pm CI$ (μM)	ρ	$F_{Obj} - PSO$	$F_{Obj} - D.O$
500	2.0	346.74±73.63	465.65±8.70	-0.1929	158.0929	158.0927
500	2.5	371.75±91.06	831.66±24.00	-0.4516	52.0058	52.0058
500	2.7	603.49±445.07	767.36±28.29	-0.3634	45.6237	45.6237
300	2.7	377.70±69.67	531.68±24.61	-0.5848	43.4028	43.4027

Where, N is the agitation speed (in rpm); Q_{CO} is the specific gas flow rate (in vvm); k_{La} is the overall volumetric mass transfer coefficient with its confidence interval (in h^{-1}); C_{CO}^s is the CO steady-state concentration with its confidence interval (in μM); CI is the confidence interval; ρ is the parametric correlation; $F_{Obj-PSO}$ is the objective function minimum value obtained in PSO; and $F_{Obj-D.O}$ is the objective function minimum value obtained through deterministic optimization.

The degrees of freedom for estimation can be determined as $DF = NE \cdot NY - NP$, where NE is the number of experiments conducted (duplicate, triplicate, etc.), NY is the number of measured dependent variables and NP is the number of parameters to be estimated (SCHWAAB and PINTO, 2007). Generally, the statistical quality of parameter estimation enhances with the increase of its degrees of freedom (ALBERTON, 2013; SCHWAAB and PINTO, 2007). However, as it can be

seen in experiments conducted in triplicate and duplicate for pure distilled water at 500 rpm and 2.7 vvm (Table V.12), the increase in degrees of freedom did not reduce parameter (k_{La} or C_{CO}^S) relative variance because one of the triplicates increased parameter uncertainty due to outliers in the measured values of dependent variables (Figure V.4A and B). The increase in experimental and parameter uncertainty is also reflected in the confidence interval, which decreased by 72% from triplicate to duplicate.

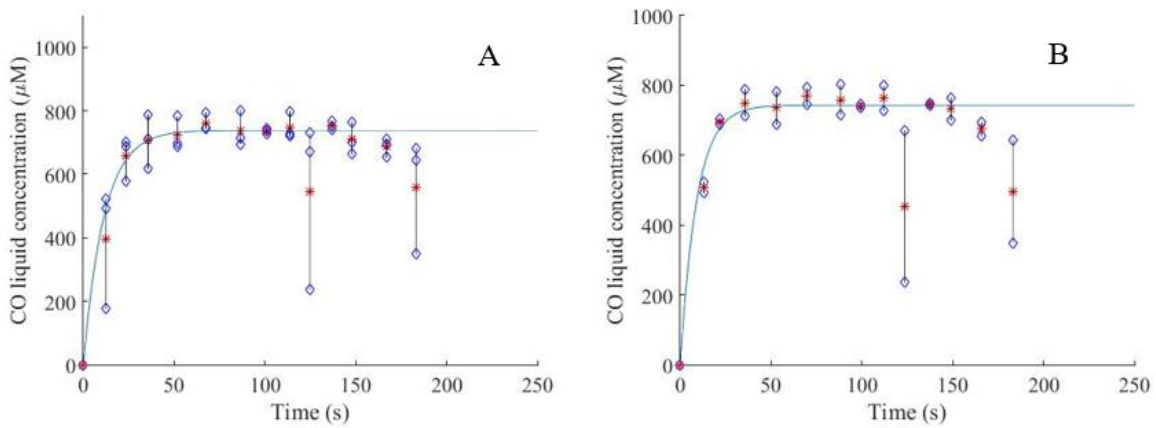


Figure V.4 Model prediction for pure distilled water at 500 rpm and 2.7 vvm performed in triplicate (A) and duplicate (B). \diamond represents the experimental data and * represents the sample mean.

Table V.12 Comparison between experiments conducted in triplicate and duplicate for pure distilled water at 500 rpm and 2.7 vvm.

	Triplicate pure distilled water at 500 rpm and 2.7 vvm	Duplicate pure distilled water at 500 rpm and 2.7 vvm
$k_{La} \pm CI$ (h^{-1})	316.99 \pm 64.95	399.06 \pm 18.25
$C_{CO}^S \pm CI$ (μM)	738.76 \pm 4.64	743.27 \pm 3.62
ρ	-0.1626	-0.3616
$\sigma_{k_{La}}/k_{La}$	0.0022	0.0001
$\sigma_{C_{CO}^S}/C_{CO}^S$	0.0172	0.0096

Where, k_{La} is the overall volumetric mass transfer coefficient (h^{-1}); C_{CO}^S is the steady-state carbon monoxide concentration (μM); ρ is the parametric correlation; $\sigma_{k_{La}}/k_{La}$ is the k_{La} relative variance; $\sigma_{C_{CO}^S}/C_{CO}^S$ is the C_{CO}^S relative variance.

It can be observed that all parametric correlation values are negative. Pearson's correlation usually varies between -1 and 1, where -1 means a perfect negative correlation between two variables. Values closed to -1 or 1 represent a strong correlation between parameters, while a parametric correlation of zero would mean no parametric correlation at all (SCHWAAB and PINTO, 2007). All estimated parameter values presented a negative parametric correlation, indicating that k_{LA} estimated values have influence in C_{CO}^S parameter values, and the contrary is also valid. Negative correlation values means that as k_{LA} values increase, C_{CO}^S values would decrease. This behaviour is well described in confidence regions present in Figure V.5, Figure V.6 and Figure V.7 (B). It is also possible to see how parametric correlation is visible in likelihood regions. For pure distilled water at 500 and 0.7 vvm, parametric correlation is -0.9198 and its likelihood region is thinner than likelihood region for pure distilled water at 500 rpm and 2.7 vvm ($\rho = -0.3616$). According to Figure V.6 for pure distilled water and 0.7 vvm k_{LA} would assume values from 38 to 82.5 h^{-1} but due to high parametric correlation, each value will assume different carbon monoxide steady-state concentration.

Figure V.7 illustrates the model adjustment (A) and likelihood region (B) for a distilled water, PFC and Tween® 80 mixture at 500 rpm and 2.7 vvm. Experimental uncertainty is high probably due to the mixture's viscosity, gas bubbles and emulsion scanning in spectrophotometer. A higher standard deviation means a higher confidence interval, therefore the calculated value of 445.07 h^{-1} , which represents 74% of the k_{LA} estimated value. Confidence region expressed in Figure V.5 (B) is very different from an elliptical confidence region, usually obtained for linear models. That is the main reason why elliptical confidence regions provide a poor approximation for non-linear model confidence region (SCHWAAB et al., 2008). The present likelihood region is non-convex and is unbounded since k_{LA} does not have an upper limit due to model structure.

Bates and Watts (1998) discussed a similar mass transfer model for oxygen demand along time (used for aerobic systems) and observed that as k_{La} value increased, the exponential term would be zero, and therefore, oxygen concentration in the liquid phase would be equal to steady-state oxygen concentration. This likelihood confidence region behaviour was also observed for other conditions in distilled water, PFC and Tween® 80 mixtures. Therefore, it can be said that the model is unable to discriminate high values of k_{La} , especially for a distilled water, PFC and Tween® 80 mixtures at 500 rpm, 2.0 and 2.7 vvm

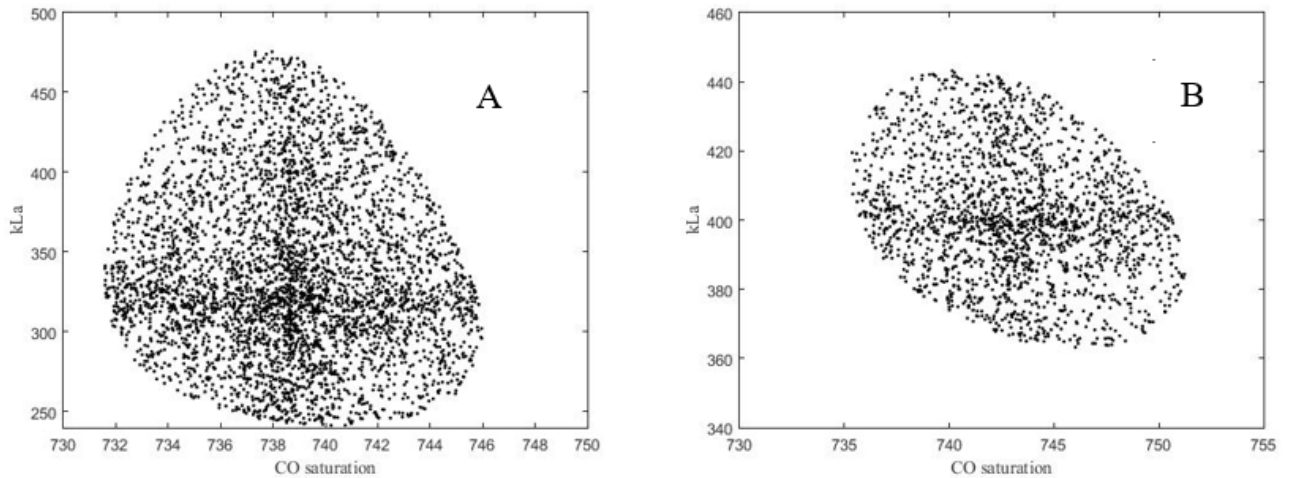


Figure V.5 Likelihood regions ($\alpha = 90\%$) for pure distilled water 500 rpm and 2.7 vvm performed in triplicate (A) and duplicate (B)

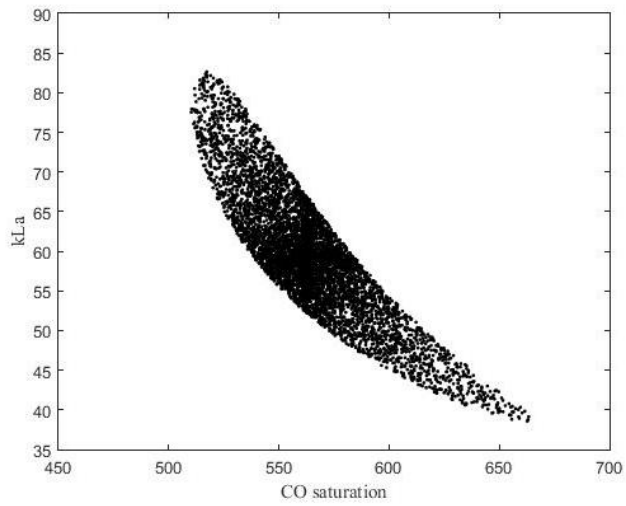


Figure V.6 Likelihood region ($\alpha = 90\%$) for pure distilled water at 500 rpm and 0.7 vvm.

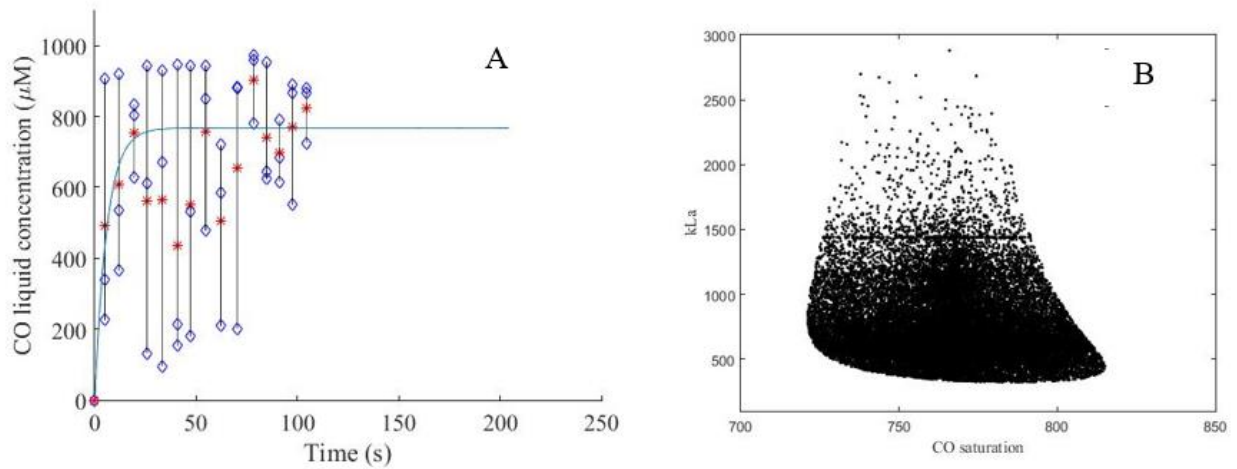


Figure V.7 Model prediction (A) and likelihood region ($\alpha=90\%$), (B) for distilled water, PFC and Tween® 80 mixture at 500 rpm and 2.7 vvm. \diamond represents the experimental data and * represents the sample mean.

CONCLUSION

The present work successfully implemented the myoglobin-protein bioassay in laboratory and obtained carbon monoxide concentration in liquid phase using this method. Therefore, it is a good and cheap method for carbon monoxide determination in lab-scale in comparison to gas chromatography. It should be noted that care must be taken during the preparation of the complex oxygen-myoglobin solution so the myoglobin concentration in the test solution would be properly quantified.

The highest k_{LA} for carbon monoxide in water at 25 °C was obtained in the present work, 399.06 h⁻¹ at 500 rpm and 2.7 vvm. PFC alone was not responsible for k_{LA} increase due to poor mixing of perfluorodecalin in distilled water. Tween® 80 increased PFC dispersion in distilled water and reduced bubble size, increasing carbon monoxide mass transfer to the liquid phase. A k_{LA} of 603.49 h⁻¹ was achieved. This is the highest overall volumetric mass transfer obtained for stirred tank bioreactors so far. It was demonstrated that perfluorocarbons can enhance the volumetric mass transfer coefficient when well mixed with distilled water in the liquid phase. This mixture can be improved by using surfactants such as Tween® 80. PFCs have already been used in the presence of cells and can be an interesting way to enhance mass transfer in synthesis gas fermentation.

Optimization was successfully performed and was a valuable tool to understand how experimental uncertainty impacted parameter uncertainty and parameter estimation. As far as we know, hybrid optimization and maximum likelihood were used for the first time to estimate carbon monoxide overall volumetric mass transfer coefficient and carbon monoxide steady-state concentration. The use of both methods increased the quality of the statistical analysis performed for the estimated parameter values.

RECOMMENDATIONS FOR FUTURE RESEARCH

Although the present work opened a new approach for overall volumetric mass transfer coefficient estimation in bioreactors, some details still need to be analysed. This chapter proposes recommendations for future work in order to deep the mass transfer analysis initialized with this dissertation.

- ✓ Determination of carbon monoxide concentration using Gas Chromatography to determine $k_{L}a$ and then evaluate myoglobin bioassay's precision and accuracy.
- ✓ Better evaluation of the mathematical model for $k_{L}a$ determination for carbon monoxide concentration.
- ✓ Change impeller configuration in the bioreactor, using a down-pumping axial flow impeller at the top and a radial flow impeller at the bottom (Rushton-Type or Smith-type) to see how it can affect $k_{L}a$.
- ✓ Determine gassed and ungassed power input for the systems described in this dissertation.
- ✓ Determining dynamic viscosity and density for distilled water and PFC mixture, distilled water and Tween® 80 mixture and distilled water, PFC and Tween® 80 mixture in order to better evaluate the bioreactor hydrodynamics for these systems.
- ✓ Apply the same methodology used in the present dissertation to evaluate mass transfer in a hollow fiber membrane bioreactor.

REFERENCES

- ABRELPE. Residue Solid Waste Panorama in Brazil, 2016.
- ALBERTON, K.P.F. Parameter Identifiability: Conceptual Aspects and Development of New Procedures. 2013. 192 p. Thesis (PhD in Chemical Engineering) – Universidade Federal do Rio de Janeiro, Rio de Janeiro, Brasil.
- AMARAL, P.F.F.; LEHOCKY, M.; BARROS-TIMMONS, A.M.V.; ROCHA-LEÃO, M.H.M.; COELHO, M.A.Z.; COUTINHO, J.A.P. Cell surface characterization of *Yarrowia lipolytica* IMUFRJ 50682. *Yeast*, v. 23, p. 867-877, 2006.
- AMARAL, P.F.F. Lipase production from *Yarrowia lipolytica* in a multiphase bioreactor. Blucher Acadêmico. 2007. 243 f. Thesis (PhD in Science) – Escola de Química, Universidade Federal do Rio de Janeiro, Rio de Janeiro, Brasil.
- AMARAL, P.F.F.; FREIRE, M.G.; ROCHA-LEÃO, M.H.; MARRUCHO, I.M.; COUTINHO, J.A.; COELHO, M.A. Optimization of oxygen mass transfer in a multiphase bioreactor with perfluorodecalin as a second liquid phase. *Biotechnology and Bioengineering*, v. 99, n. 3, p. 588-598, 2008.
- ANTONINI, E.; BRUNORI, M. Hemoglobin and Myoglobin in Their Interactions with Ligands. North Holland, Amsterdam, 1971.
- AYORINDE, F.O.; GELAIN, S.V.; JOHNSON JR., J.H.; WAN, L.W. Analysis of some commercial polysorbate formulations using matrix-assisted laser desorption/ionization time-of-flight mass spectrometry. *Rapid Communications in Mass Spectrometry*, v. 14, p. 2116-2124, 2000.
- BAJPAL. P. Environmentally Benign Approaches for Pulp Bleaching. New York and London: Elsevier Science, 2th Edition, 288 p. 2005.

- BATES, D.M.; WATTS, D.G. Nonlinear Regression Analysis and its Applications. Wiley and Sons, New York, 90 p., 1988
- BARD, Y. Nonlinear Parameter Estimation. Academic Press, New York and London, 1974, 341 p.
- BAKER, A.; VAN DER AKKER, H.E.A Gas-Liquid Contacting with Axial Flow Impellers. *Chemical Engineering Research and Design*, v. 72, p. 53-58, 1994.
- BEALE, R.M.L. Confidence-regions in non-linear estimation. *Journal of Royal Statistical Society B – Statistical Methodology*, v. 22, n. 1, p. 41-88, 1960.
- BELO, I.; GARCÍA-ABUÍN, A.; GÓMEZ-DÍAZ, D.; NAVAZA, J.M.; VIDAL-TATO, I. Effect of Tween 80 on Bubble Size and Mass Transfer in a Bubble Contactor. *Chemical Engineering Technology*, v. 34, n. 11, p. 1790-1796, 2011.
- BORZANI, W.; AQUARONE, W.; LIMA, U. de A.; SCHMIDELL, W. Industrial Biotechnology. Blucher, São Paulo, v. 2. 2001 (in Portuguese).
- BREDWELL, M.D.; WORDEN, M.R. Mass-transfer properties of microbubbles 1. Experimental studies. *Biotechnology Progress*, v. 14, n. 1, p. 31-38, 1998.
- BREDWELL, M.D.; SRIVASTAVA, P.; WORDEN, R.M. Reactor design issues for synthesis-gas fermentations. *Biotechnology Progress*, v. 15, n. 5, p. 834–844, 1999.
- CABARET, F.; FRADETTE, L.; TANGUY, P.A. Gas-Liquid Mass Transfer in unbaffled dual-impellers mixers. *Chemical Engineering Science*, v. 63, n. 6, p. 1636-1647, 2008.
- CABRALES, P.; VÁZQUEZ, B.Y.S.; NEGRETE, A.C.; INTAGLIETTA, M. Perfluorocarbons as gas transporters for O₂, NO, CO and volatile anesthetics. *Transfusion Alternatives in Transfusion Medicine*, v. 9, n. 4, p. 294-303, 2007.

- CASTRO-FORERO, A.; JIMÉNEZ, D.; LÓPEZ-GARRIGA, J.; TORRES-LUGO, M. Immobilization of Myoglobin from Horse Skeletal Muscle in Hydrophilic Polymer Networks. *Journal of Applied Polymer Science. Applied Polymer Symposium*, v. 107, n. 2, p. 881-890, 2009.
- CHANG, I.S.; KIM, B.H.; LOVITT, R.W.; BANG, J.S. Effect of CO partial pressure on cell-recycled continuous CO fermentation by *Eubacterium limosum* KIST612. *Process Biochemistry*, v. 37, p. 411-421, 2001.
- CHERUBINI, F. The biorefinery concept: Using biomass instead of oil for producing energy and chemicals. *Energy Conversion Management*, v. 51, n. 7, p. 1412-1421, 2010.
- CHRISTI, M.Y. Airlifts Bioreactors. New York and London: Elsevier Applied Science, 345 p. 1989.
- CHO, M.H.; WANG, S.S. Enhancement of oxygen transfer in hybridoma cell culture by using a perfluorocarbon as oxygen carrier. *Biotechnology Letters*, v. 10, n. 12, p. 855-860, 1988.
- CLARK, L.C.; GOLLAN, F. Survival of Mammals Breathing Organic Liquids Equilibrated with Oxygen at Atmospheric Pressure. *Science*, v. 152, n. 3730, p. 1755-1756, 1966.
- COOKE, M. HEGGS, P.J. Advantages of the hollow (concave) turbine for multi-phase agitation under intense operating conditions. *Chemical Engineering Science*, v. 60, n. 20, p. 5529-5543, 2005.
- CONAB. Thermoelectric generation with sugar cane bagasse thermal conversion in Brazil – performance analysis of 2009-2010 crop, 2011.
- COULSON, J.M.; RICHARDSON, J.F. Chemical Engineering Volume 1 – Fluid Flow, Heat Transfer and Mass Transfer. Oxford: Elsevier, 6th Edition, 824 p. 1999.

- COWGER, J.P.; KLASSON, K.T.; ACKERSON, M.D.; CLAUSEN, E.C.; GADDY, J.L. Mass-Transfer and Kinetic Aspects in Continuous Bioreactors Using *Rhodospirillum rubrum*. *Applied Biochemistry and Biotechnology*, v. 34/35, p. 613-624, 1992.
- DEVARAPALLI, M.; ATIYEH, H.K. A review of conversion processes for bioethanol production with a focus on syngas fermentation. *Biofuel Resources Journal*, v. 2, n. 3 p. 268-280, 2015.
- DORAN, P.M. Bioprocess Engineering Principles. Oxford: Academic Press, Elsevier, 2nd Edition, 919 p. 2013.
- DRAPER, N.R.; SMITH, H. Applied Regression Analysis. New York: Wiley & Sons, 3rd Edition, 760 p. 1998.
- ELIBOL, M. Use of perfluorocarbon in the culture of *Saccharomyces cerevisiae*. *Biotechnol Tech*, v. 10, p. 987-990, 1996.
- ELIBOL, M. Culture of yeast in a perfluorocarbon/water system. *Biotechnol Tech*, v. 11, p. 593-596, 1997.
- ELIBOL, M.; MAVITUNA, F. Effect of perfluorodecalin as an oxygen carrier on actinorhodin production by *Streptomyces coelicolor* A3(2). *Applied Microbiology Biotechnology*, v. 43, n. 2, p. 206-210, 1995.
- GOFF, H.D. Colloidal aspects of ice cream – A review. *International Dairy Journal*, v. 7, n. 6-7, p. 363-373, 1997.
- GOLDBER, D.E. Genetic Algorithm in Search, Optimization and Machine Learning. Addison-Wesley Professional, 1st Edition, 1989. 432 p.
- HALPERIN, M. Confidence interval estimation in non-linear regression. *Journal of Royal Statistical Society B – Statistical Methodology*, v. 25, n. 2, p. 330-333, 1963.

- HARTLEY, H.O. Exact confidence regions for the parameters in non-linear regression laws. *Biometrika*, v. 51, n. 3-4, p. 347-353, 1964.
- HIBBERT, H.D. Genetic algorithms in chemistry. *Chemometrics and Intelligent Laboratory Systems*, v. 19, n. 3, p. 277-293, 1993.
- HOFFMAN, R.A.; GARCIA, M.L.; VESKIVAR, M.; KARIM, K.; AL-DAHMAN, M.H.; ANGENENT, L.T. Effect of shear on performance and microbial ecology of continuously stirred anaerobic digesters treating animal manure. *Biotechnology and Bioengineering*, v. 100, n. 1, p. 38-48, 2008.
- JADE, A.M.; JAYARAMAN, V.K.; KULKARNI, B.D.; KHOPKAR, A.R.; RANADE, V.V.; SHARMA, A. A novel local singularity distribution based method for flow regime identification: Gas-liquid stirred vessel with Rushton turbine. *Chemical Engineering Science*, v. 61, n. 2, p. 688-697, 2006.
- JU, L.K; LEE, J.F. ARMINGER, W.B. Enhancing Oxygen Transfer in Bioreactors by Perfluorocarbon Emulsions. *Biotechnology Progress*, v. 7, n. 4, p. 323-329, 1991.
- JUNKER B.H.; HATTON, A.; WANG, D.I.C. Oxygen transfer enhancement in aqueous/perfluorocarbon fermentation systems II. Theoretical analysis. *Biotechnology and Bioengineering*, v. 35, p. 578-585, 1990.
- KADIC, E.; HEINDEL, T.J. An Introduction to Bioreactor Hydrodynamics and Gas-Liquid Mass Transfer. New Jersey: *John Wiley & Sons*, 2014, 314 p.
- KAPIC, A.; JONES, S.T.; HEINDEL, T.J. Carbon Monoxide Mass Transfer in a Syngas Mixture. *Industrial & Engineering Chemistry Research*, v. 45, p. 9150-9155, 2006.
- KENNEDY, J.; EBERHART, R. Particle swarm optimization. *Proceedings of the IEEE International Conference on Neural Networks*, v. 4, p. 1942-1948, 1995.

- KIM, J.K.; JUNG, J.Y.; KIM, J.H.; KIM, M.-G.; KASHIWAGI, T.; KANG, Y.T. The effect of chemical surfactants on the absorption performance during NH₃/H₂O bubble absorption process. *International Journal of Refrigeration*, v. 29, n. 2, p. 170-177, 2006.
- KIRKPATRICK, S.; GELATT JR., C.D.; VECCHI, M.P. Optimization by simulated annealing. *Science*, 220, n. 4598, p. 671-680, 1983.
- KLASSON, K.T.; ACKERSON, M.D.; CLAUSEN, E.C.; GADDY, J.L. Bioreactor design for synthesis gas fermentations. *FUEL*, v. 70, p. 605-614, 1991.
- KLASSON, K.T.; GUPTA, A.; CLAUSEN, E.C.; GADDY, J.L. Evaluation of Mass-Transfer and Kinetic Parameters for *Rhodospirillum rubrum* in a Continuous Stirred Tank Reactor. *Applied Biochemistry and Biotechnology*, v. 39/40, p. 549-557, 1993
- KOKALJ, F.; SAMEC, N. Combustion of Municipal Solid Waste for Power Production. In: NG, H.K. *Advances in Internal Combustion Engines and Fuel Technologies*, INTECH Open, 2013. p. 277-309.
- KUNDU, S.; PREMER, S.A.; HOY, J.A.; TRENT III, J.T.; HARGROSE, M.S. Direct Measurement of Equilibrium Constants for High-Affinity Hemoglobins. *Biophysical Journal*, v. 84, n. 6, p. 3931-3940, 2003.
- LATIF, H.; ZEIDAN, A.A.; NIELSEN, A.T.; ZENGLER, K. Trash to treasure: production of biofuels and commodity chemicals via syngas fermenting microorganisms, *Current Opinion in Biotechnology*, v. 27, p. 79-87, 2014.
- LEE, P.-H.; NI, S.-Q.; CHANG, S.-Y.; SUNG, S.; KIM, S.-H. Enhancement of carbon monoxide mass transfer using an innovative external hollow fiber membrane (HFM) diffuser for syngas fermentation: Experimental studies and model development. *Chemical Engineering Journal*, v. 184, p. 268-277, 2012.

- LIM, M.; JACKSON, T.A.; ANFINRUD, P.A. Binding of CO to Myoglobin from a Heme Pocket Docking Site to Form Nearly Linear Fe-C-O. *Science*, v. 269, n. 5226, p. 962-966, 1995.
- LIOU, J.S.C.; BALKWILL, D.L.; DRAKE, G. R.; TANNER, R. S. *Clostridium carboxidivorans* sp. nov., a solvent-producing isolated from an agricultural settling lagoon, and reclassification of the acetogen *Clostridium scatologenes* strains SL1 as *Clostridium drakei* sp. nov. *Int. J. Syst. Evol. Microbiol.*, vol. 55, p. 2085-2091, 2005.
- LOUBIÈRE, K.; HÉBRARD, G. Influence of liquid surface tension (surfactants) on bubble formation at rigid and flexible orifices. *Chemical Engineering Processing: Process Intensification*, v. 43, n. 11, p. 1361-1369, 2004.
- LOWE, K.C. Perfluorochemical respiratory gas carriers: benefits to cell culture systems. *Journal Fluorine Chemistry*, v. 118, p. 19-26, 2002.
- LOWE, K.C.; DAVEU, M.R.; POWER, J.B. Perfluorochemicals: their applications and benefits to cell culture. *Tibtech*, v. 16, n. 6, p. 272-277, 1998.
- MADIC, C.; BERTHON, L.; ZORZ, N.; COULOMBEAU, H.; TESTARD, F.; ZEMB, T.; GIBANEL, S.; LARPENT, C.; BACZKO, K. FR Pat. 2.829.493, 2003
- MCMILLAN, J.D.; WANG, D.I.C. Enhanced oxygen transfer using oil-in-water dispersions. In: ANN, N.I. *Biochemical Engineering V*. Academic Science, New York, v. 506, p. 569-582, 1987.
- MOHAMMADI, M.; NAJAFPOUR, G.D.; YOUNESI, H.; LAHIJANI, P.; UZIR, M.H.; MOHAMED, A.R. Bioconversion of synthesis gas to second generation biofuels: A review. *Renewable and Sustainable Energy Reviews*, v. 15, p. 4255-4273, 2011.

- MOHAMMADI, M.; YOUNESI, H.; NAJAFPOUR, G.; MAHAMED, A.R. Sustainable ethanol fermentation from synthesis gas by *Clostridium ljungdahlii* in a continuous stirred tank bioreactor. *Journal of Chemical Technology and Biotechnology*, 87 (6), 873-843, 2012.
- MOUCHA, T.; LINEK, V.; PROKOPOVA, E. Gas hold-up, mixing time and gas-liquid volumetric mass transfer coefficient of various multiple-impeller configurations: Rushton turbine, pitched blade and techmix impeller and their combinations. *Chemical Engineering Science*, v. 60, n. 6, p. 1465-1475, 2003.
- MUNASINGHE, P.C.; KHANAL, S.K. Syngas fermentation to biofuel: evaluation of monoxide mass transfer coefficient (K_{la}) in different reactor configurations. *Biotechnology*, v. 26; p. 1616-1621, 2010.
- MUNASINGHE, P. C.; KHANAL, S. K. Syngas fermentation to biofuel: Evaluation of carbon monoxide mass transfer and analytical modelling using a composite hollow fiber (CHF) membrane bioreactor. *Bioresour. Technol.*, v. 122, 130-136, 2012.
- MUNASINGHE, P.C.; KHANAL, S.K. Evaluation of hydrogen and carbon monoxide mass transfer and a correlation between the myoglobin-protein bioassay and gas chromatography method for carbon monoxide determination. *Royal Society of Chemistry Advances*, v. 4, p. 37575-37581, 2014.
- NAUMAN, E.B. *Chemical Reactor Design, Optimization, and Scale up*. New Jersey: John Wiley & Sons, Inc., 2nd Edition, 608 p. 2008.
- NIENOW, A.W.; WISDOM, D.J.; MIDDLETON, J.C. The effect of scale and geometry on flooding, recirculation, and power in gasses stirred vessels. In: STEPHENS, H.S.; CLARK, J.A. *Proceedings of the Second European Conference on Mixing*. BHRA Fluid Engineering, Cambridge, Cranfield, UK, 1977. p. 17-34.

- NISHIKAWA, M.; NISHIOKA, S.; KAYAMA, T. Gas absorption in an aerated mixing vessel with multi-stage impellers. *Journal of Chemical Engineering of Japan*, v. 17, n. 3, p. 227-232, 1984.
- OGUT, A.; HATCH, R.T. Oxygen transfer into Newtonian and non-Newtonian fluids in mechanically agitated vessels. *Canadian Journal of Chemical Engineering*, v. 66, n. 1, p. 79-85, 1988.
- OHYAMA, Y.; ENDOH, K. Power characteristics of gas-liquid contacting mixers. *Chemical Engineering (Japan)*, v. 19, p. 2-11, 1955.
- OLDSHUE, J.Y. Fluid Mixing Technology. New York: McGraw-Hill, 1983. 574p.
- OLDSHUE, J.Y. Agitation. In: VOGEL, H.C.; TODARO, C.L. *Fermentation and Biochemical Engineering Handbook: Principles, Process Design, and Equipment*. New Jersey, USA. Noyes Publications, 2nd Edition, 1997. p. 181-241.
- ORGILL, J.J.; ATIYEH, H.K.; DEVARAPALLI, M.; PHILLIPS, J.R., LEWIS, R.S.; HUHNKE, R.L. A comparison of mass transfer coefficients between trickle-bed, hollow fiber membrane and stirred tank reactor. *Bioresource Technology*, v. 133, p. 340-346, 2013.
- PAINMANAKUL, P.; LOUBIÈRE, K.; HÉBRARD, G.; MIETTON-PEUCHOT, M.; ROUSTAN, M. Effect of surfactants on liquid-side mass transfer coefficients. *Chemical Engineering Science*, v. 60, n. 22, p. 6480-6491, 2005.
- PANTALÉON, V.; BOUTTIER, S.; SOAVELOMANDROSO, A. P.; JANOIR, C.; CANDELA, T. Biofilms of *Clostridium* species. *Anaerobe*, v. xxx, p. 1-6, 2014.
- PENNEY, D.G. Carbon Monoxide and Introduction. 2012. Available at: <<http://www.coheadquarters.com/coproperties.htm>>. Accessed: 18/12/2017.

- REDDY, P.J. Energy Recovery from Municipal Solid Waste by Thermal Conversion Technologies. CRC Press, London, UK, 2016. 238 p.
- RIGGS, S.S.; HEINDEL, T.J. Measuring Carbon Monoxide Gas-Liquid Mass Transfer in a Stirred Tank Reactor for Syngas Fermentation. *Biotechnology Progress*, v. 22, n. 3, p. 903-906, 2006.
- ROMAGNOLI, J.A.; SANCHEZ, M.C. Data Processing and Reconciliation for Chemical Process Operations. Academic Press, New York, 1999. 270 p.
- RUSHTON, J.H.; COSTICH, E.W.; EVERETT, H.J. Power characteristics of mixing impellers – Part I. *Chemical Engineering Progress*, v. 46, n. 8, p. 395-404, 1950a.
- RUSHTON, J.H.; COSTICH, E.W.; EVERETT, H.J. Power characteristics of mixing impellers – Part II. *Chemical Engineering Progress*, v. 46, n. 9, p. 395-404, 1950b.
- RUZICKA, M.C.; VECER, M.M.; ORVALHO, S.; DRAHOŠ, J. Effect of surfactant on homogeneous regime stability in bubble column. *Chemical Engineering Science*, v. 63, p. 951-967, 2008.
- SANTOS, T.J.; PINTO, J.C. Taking variable correlation into consideration during parameter estimation. *Brazilian Journal of Chemical Engineering*, v. 15, n. 1, p. 1-20, 1998.
- SARDEING, R.; PAINMANAKUL, P.; HÉBRARD, G. Effect of surfactants on liquid-side mass transfer coefficients in gas-liquid systems: A first step to modelling. *Chemical Engineering Science*, v. 61, p. 6249-6260, 2006.
- SCHWAAB, M. Evaluation of heuristic optimization algorithms in parameter estimation problems. 2005. 149f. Dissertation (MSc in Chemical Engineering) – PEQ/COPPE, Universidade Federal do Rio de Janeiro, Rio de Janeiro, Brasil.

SCHWAAB, M. Development and Implementation of New Techniques for Parameter Estimation and Sequential Design of Experiments. 2007. 171 p. Thesis (PhD in Chemical Engineering) – PEQ/COPPE, Universidade do Rio de Janeiro, Rio de Janeiro, Brasil.

SCHWAAB, M.; BISCAIA JR., E.V.; MONTEIRO, J.L.; PINTO J.C. Nonlinear parameter estimation through particle swarm optimization. *Chemical Engineering Science*, v. 63, p. 1542-1552, 2008.

SCHWAAB, M.; PINTO, J.C. Experimental Data Analysis I: Fundamentals of Statistics and Parameter Estimation. Rio de Janeiro: e-papers, 2007. 461 p.

SHEN, Y.; BROWN, R.; WEN, Z. Syngas fermentation of *Clostridium carboxidivorans* P7 in a hollow fiber membrane biofilm reactor: Evaluating the mass transfer coefficient and ethanol production performance. *Biochem. Eng. J.*, v. 85, p. 21-29, 2014a.

SHEN, Y.; BROWN, R.; WEN, Z. Enhancing mass transfer and ethanol production in syngas fermentation of *Clostridium carboxidivorans* P7 through a monolithic biofilm reactor. *Applied Energy*, v. 136, p. 68-76, 2014b.

SHEN, Y.; JARBOE, L.; BROWN, R.; WEN, Z. A thermochemical-biochemical hybrid processing of lignocellulosic biomass for producing fuels and chemicals. *Biotechnology Advances*, v. 33, n. 8, p. 1799-1813, 2015.

SHI, Y.; EBERHART, R. A modified particle swarm optimizer. In: STEPHENS, H.S.; CLARK, J.A. *Proceedings of the IEEE International Conference on Evolutionary Computation*. ALTEC, Anchorage, Alaska, 1998. p. 69-73.

SIGMA-ALDRICH. Perfluorodecalin. Available at:
<<https://www.sigmaaldrich.com/catalog/product/aldrich/p9900?lang=pt®ion=BR>>.
Accessed: 30/01/2018.

SIGMA-ALDRICH. TWEEN® 80. Available at:

<<https://www.sigmaaldrich.com/catalog/substance/tween8012345900565611?lang=pt®ion=BR>>. Accessed: 30/01/2018.

SMITH, J.M.; VAN'T RIET, K.; MIDDLETON, J.C. Scale-up of agitated gas-liquid reactors for mass-transfer. In: STEPHENS, H.S.; CLARK, J.A. *Proceedings of the Second European Conference on Mixing*. BHRA Fluid Engineering, Cambridge, Cranfield, UK, 1977. p. 51-66.

TURICK, C.E.; BULMER, D.K. Enhanced reduction of nitrous oxide by *Pseudomonas denitrificans* with perfluorocarbons. *Biotechnology Letters*, v. 20, p. 123-125, 1998;

UNGERMAN, A.J.; HEINDEL, T.J. Carbon Monoxide Mass Transfer for Syngas Fermentation in a Stirred Tank Reactor with Dual Impeller Configurations. *Biotechnology Progress*, v. 23, n. 3, p. 613-620, 2007.

VASCONCELOS, J.M.T.; RODRIGUES, J.M.L.; ORVALHO, S.C.P.; ALVEZ, S.S.; MENDES, R.L; REIS, A. Effect of contaminants on mass transfer coefficients in bubble column and airlift contactors. *Chemical Engineering Science*, v. 58, n. 8, p. 1431–1440, 2003.

VEGA, J.L.; ANTORRENA, G.M.; CLAUSEN, E.C.; GADDY, J.L. Study of gaseous substrate fermentations: Carbon monoxide conversion to acetate. 2 Continuous culture. *Biotechnology and Bioengineering*, v. 34, n. 6, p. 785-793, 1989.

WARMOESKERKEN, M.M.C.G; SPEUR, J.; SMITH, J.M. Gas-Liquid Dispersion with Pitched Blade Turbines. *Chemical Engineering Communications*, v. 25m p. 11-29, 1984.

- WASANASATHIAN, A.; PENG, C.-A. Enhancement of microalgae growth by using perfluorocarbon as oxygen carrier. *Artificial Cells, Blood Substitutes and Immobilization Biotechnology*, v. 29, p. 47-55, 2001.
- WATTS, D.G. Estimating parameters in nonlinear rate equation. *Canadian Journal of Chemical Engineering*, v. 72, n. 4, p. 701-710, 1994.
- WILLIAMS, E.J. Exact fiducial limits in non-linear estimation. *Journal of Royal Statistical Society B – Statistical Methodology*, v. 24, n. 1, p. 125-139, 1962.
- WORDEN, R.M.; BREDWELL, M.D. Mass-transfer properties of microbubbles II. Analysis using a dynamic model. *Biotechnology Progress*, v. 14, n. 1, p. 39-46, 1998.
- WORLD ENERGY COUNCIL. World Energy Resources – Waste to Energy, 2016.
- WUELFING, W.P.; KOSUDA, K.; TEMPLETON, A.C.; HARMAN, A.; MOWERY, M.D.; REED, R.A. Polysorbate 80 UV/vis spectral and chromatographic characteristics – defining boundary conditions for use of the surfactant in dissolution analysis. *Journal of Pharmaceutical and Biomedical Analysis*, v. 41, p. 774-782, 2006.
- YASIN, M.; PARK, S.; JEONG, Y.; LEE, J.; CHANG, I. S. Effect of internal pressure and gas/liquid interface area on the CO mass transfer coefficient using hollow fibre membranes as high mass transfer gas diffusing system for microbial syngas fermentation. *Bioresource Technology*, v. 169, n. p. 637-643, 2014.
- YASIN, M.; JEONG, Y.; PARK, S.; JEONG, J.; LEE, E.Y.; LOVITT, R.W.; KIM, B.H.; LEE, J.; CHANG, I.C. Microbial synthesis gas utilization and ways to resolve kinetic and mass-transfer limitations. *Bioresource Technology*, v. 177, p. 361-374, 2015.
- YOUNESI, H.; NAJAFPOUR, G.; KU ISMAIL, K.S.; MOHAMED, A.R.; KAMARUDDIN, A.H. Biohydrogen production in continuous stirred tank bioreactor from synthesis gas by

anaerobic photosynthetic bacterium: *Rhodospirillum rubrum*. *Bioresource Technology*, v. 88, p. 2612-2619, 2008.

APPENDIX

This section include all graphic material obtained during parameter estimation of k_{La} and C_{CO}^s using a hybrid optimization strategy performed in MATLAB.

A.1 – Pure distilled water at 25 °C, 100 rpm and 0.7 vvm

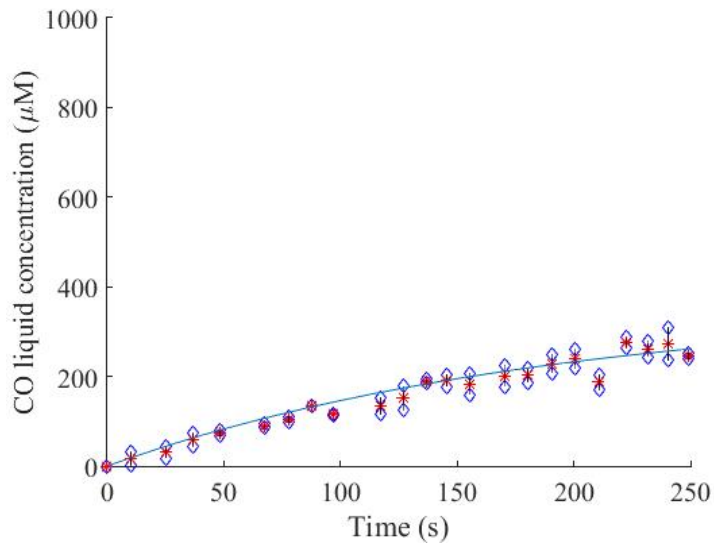


Figure A.1 Model prediction for pure distilled water at 25 °C, 100 rpm and 0.7 vvm.

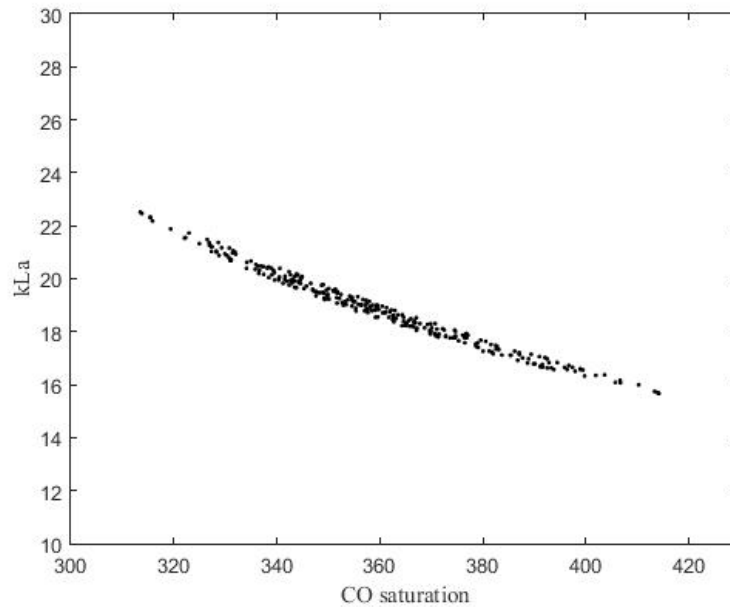


Figure A.2 Confidence region ($\alpha=90\%$) for pure distilled water at 25 °C, 100 rpm and 0.7 vvm.

A.2 – Pure distilled water at 25 °C, 100 rpm and 1.3 vvm

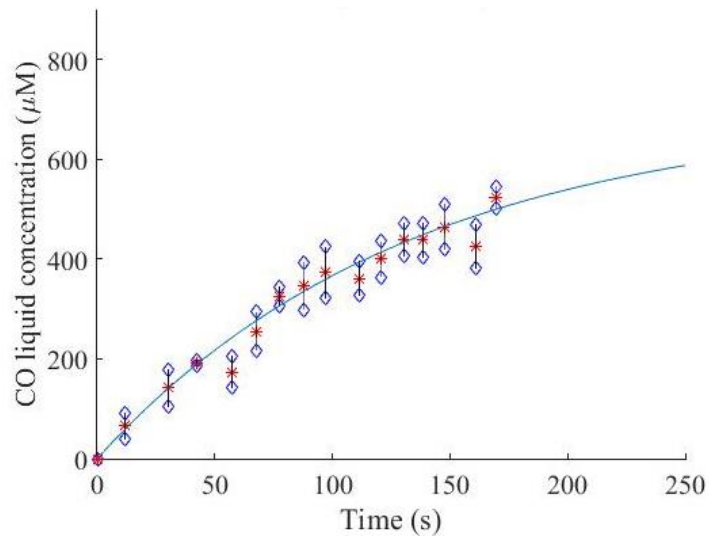


Figure A.3 Model prediction for pure distilled water at 25 °C, 100 rpm and 1.3 vvm.

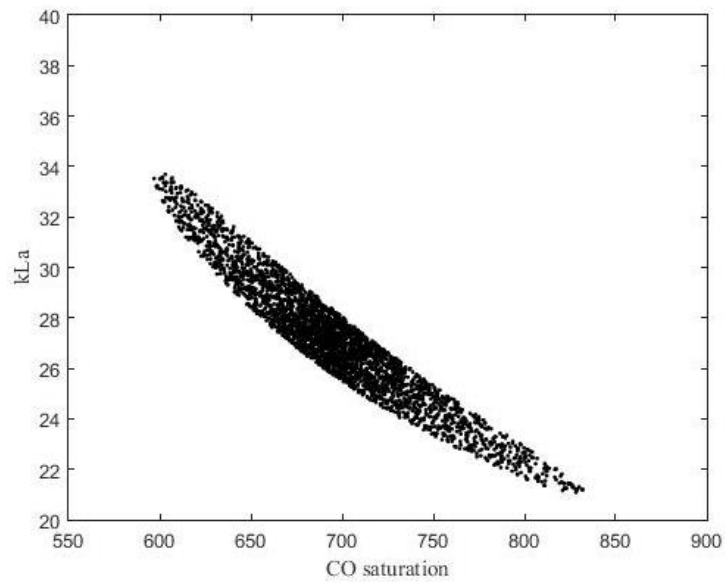


Figure A.4 Confidence region ($\alpha=90\%$) for pure distilled water at 25 °C, 100 rpm and 1.3 vvm.

A.3 – Pure distilled water at 25 °C, 100 rpm and 2.7 vvm

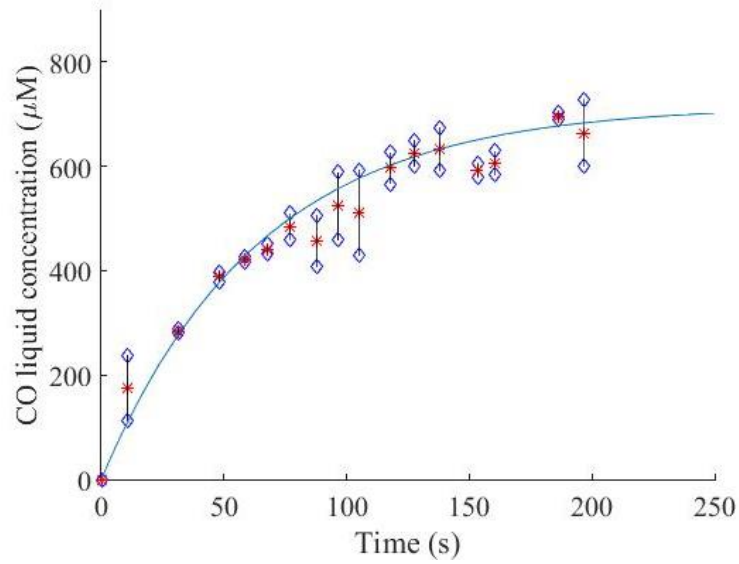


Figure A.5 Model prediction for pure distilled water at 25 °C, 100 rpm and 2.7 vvm.

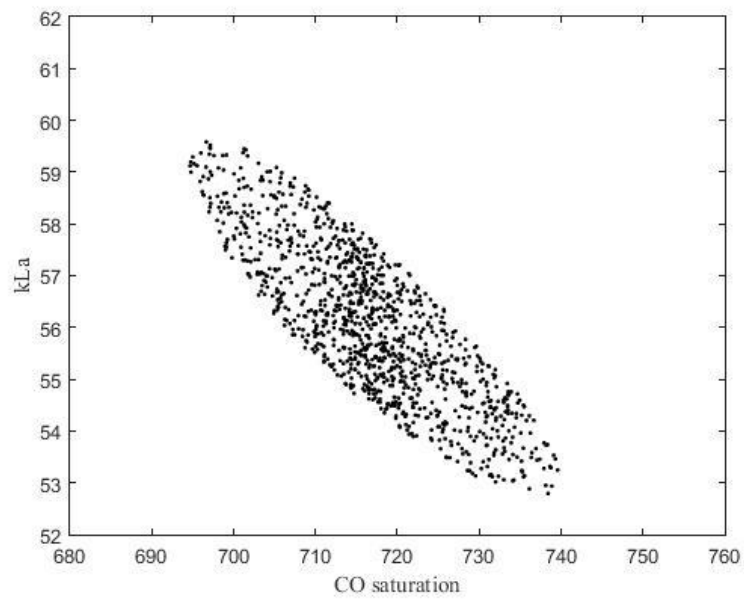


Figure A.6 Confidence region ($\alpha=90\%$) for pure distilled water at 25 °C, 100 rpm and 2.7 vvm.

A.4 – Pure distilled water at 25 °C, 300 rpm and 0.7 vvm

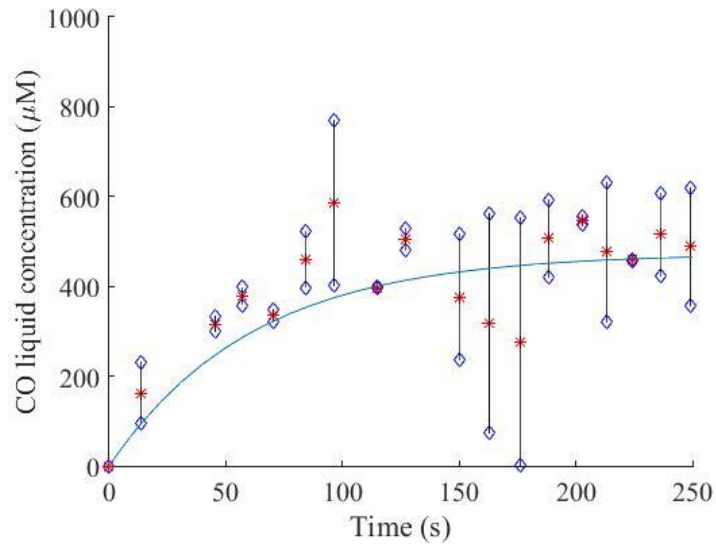


Figure A.7 Model prediction for pure distilled water at 25 °C, 300 rpm and 0.7 vvm.

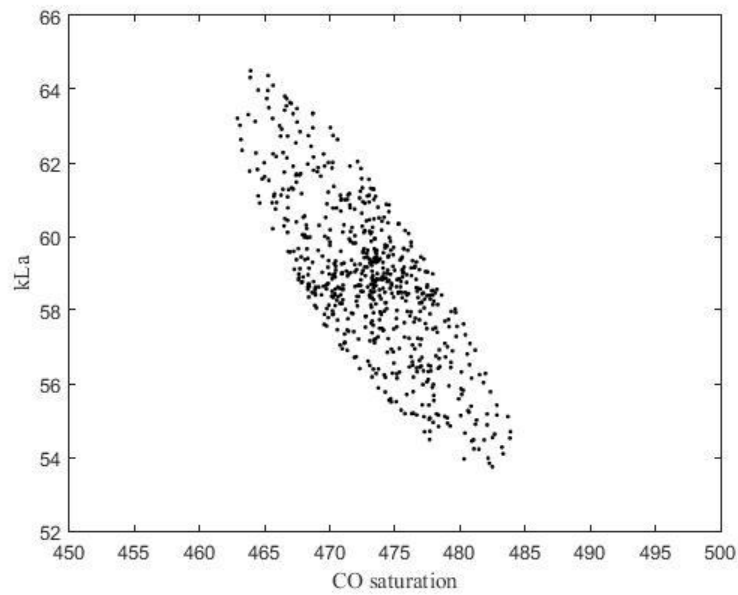


Figure A.8 Confidence region ($\alpha=90\%$) for pure distilled water at 25 °C, 300 rpm and 0.7 vvm.

A.5 – Pure distilled water at 25 °C, 300 rpm and 1.3 vvm

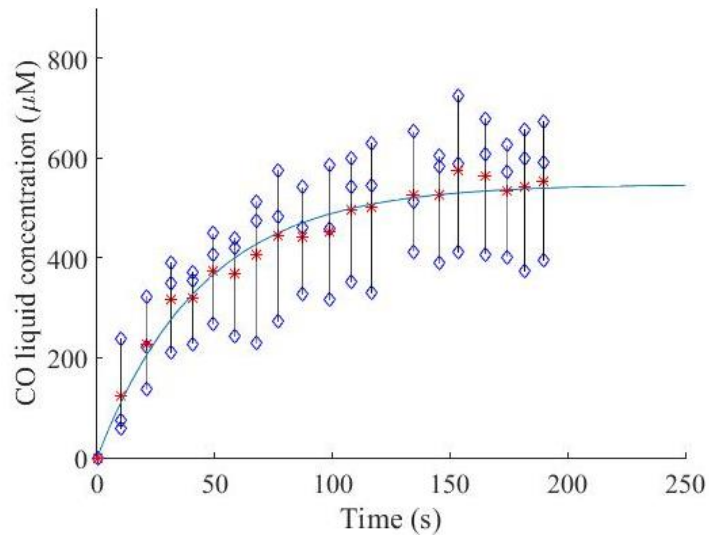


Figure A.9 Experimental data for pure distilled water at 25 °C, 300 rpm and 1.3 vvm.

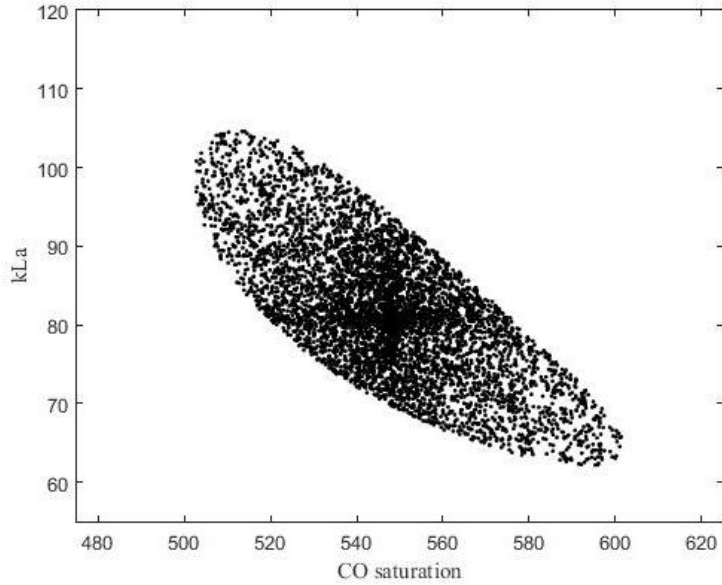


Figure A.10 Confidence region ($\alpha=90\%$) for pure distilled water at 25 °C, 300 rpm and 1.3 vvm.

A.6 – Pure distilled water at 25 °C, 300 rpm and 2.7 vvm

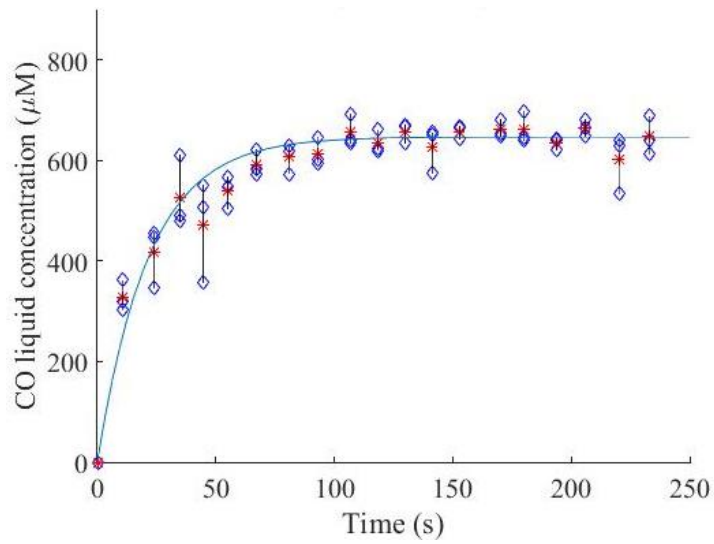


Figure A.11 Model prediction for pure distilled water at 25 °C, 300 rpm and 2.7 vvm.

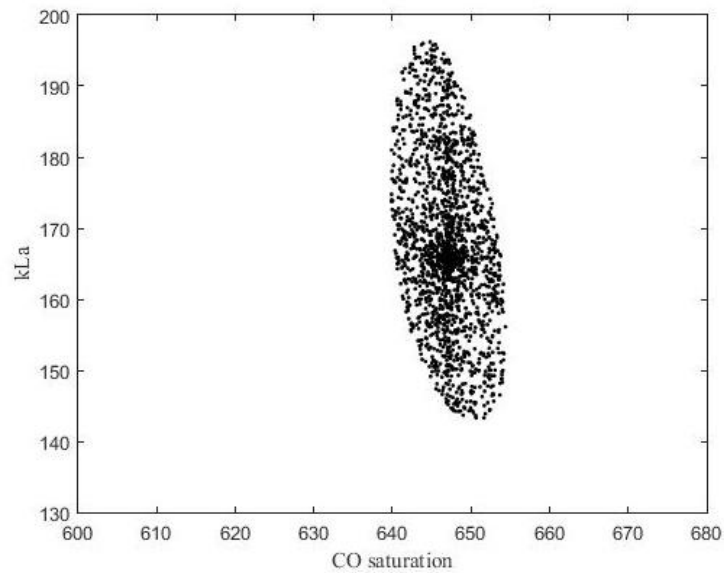


Figure A.12 Confidence region ($\alpha=90\%$) for pure distilled water at 25 °C, 300 rpm and 2.7 vvm.

A.7 – Pure distilled water at 25 °C, 500 rpm and 0.7 vvm

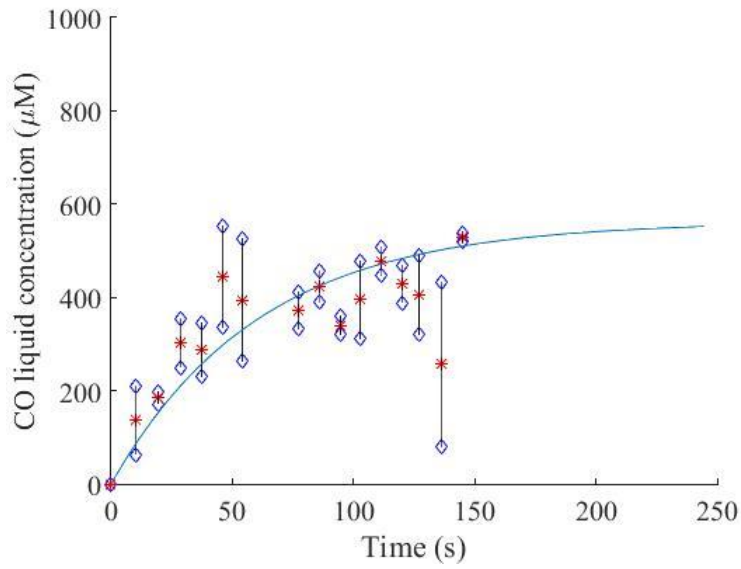


Figure A.13 Model prediction for pure distilled water at 25 °C, 500 rpm and 0.7 vvm.

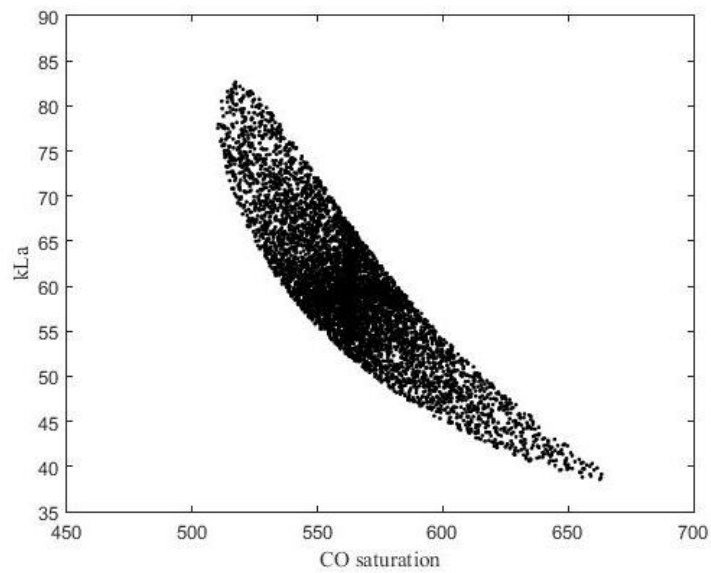


Figure A.14 Confidence region ($\alpha=90\%$) for pure distilled water at 25 °C, 500 rpm and 0.7 vvm.

A.8 – Pure distilled water at 25°C, 500 rpm and 1.3 vvm

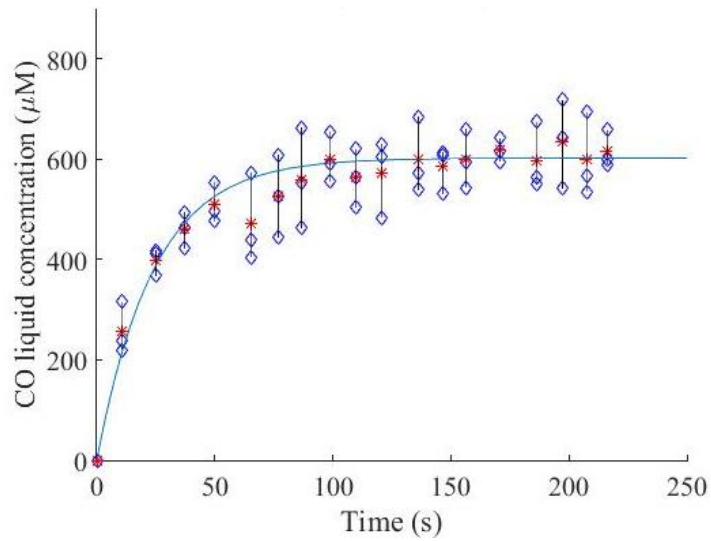


Figure A.15 Model prediction for pure distilled water at 25 °C, 500 rpm and 1.3 vvm.

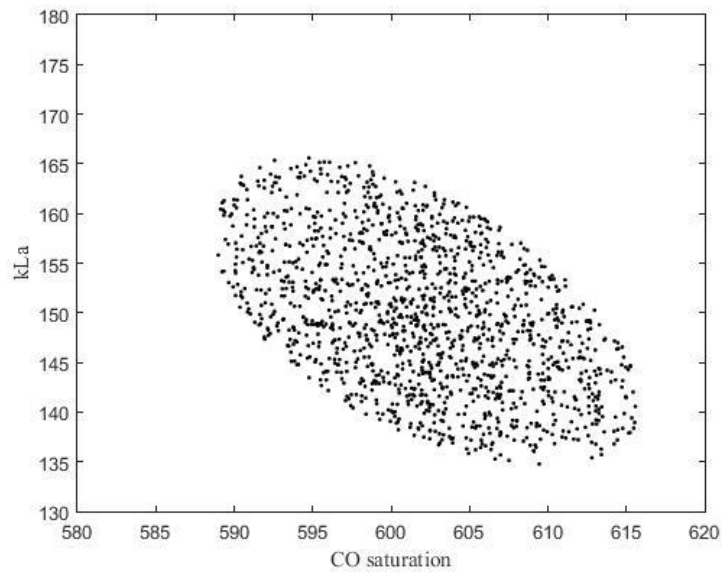


Figure A.16 Confidence region ($\alpha=90\%$) for pure distilled water at 25 °C, 500 rpm and 1.3 vvm.

A.9 – Pure distilled water at 25°C, 500 rpm and 2.0 vvm

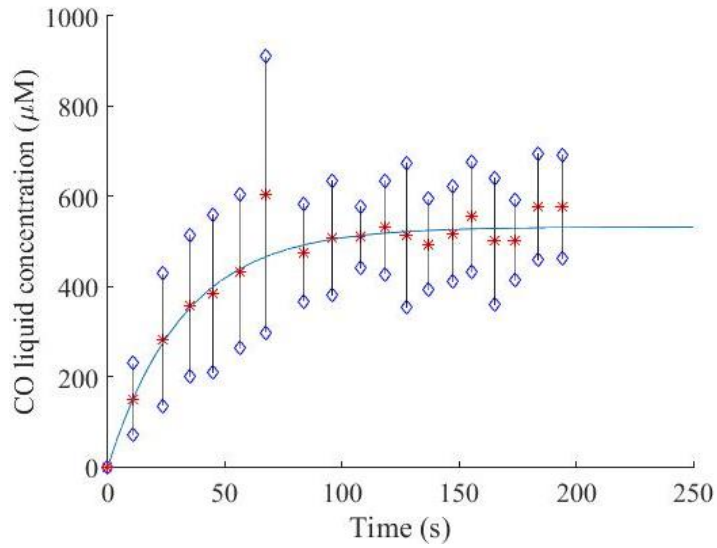


Figure A.17 Model prediction for pure distilled water at 25 °C, 500 rpm and 2.0 vvm.

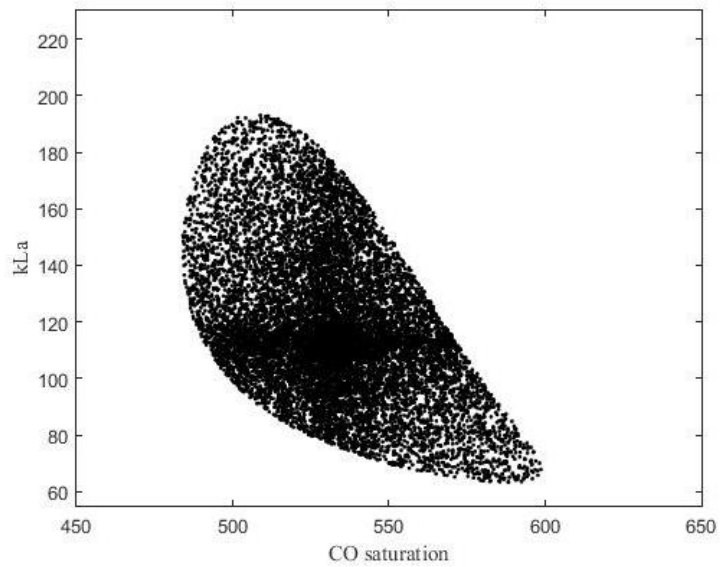


Figure A.18 Confidence region ($\alpha=90\%$) for pure distilled water at 25 °C, 500 rpm and 2.0 vvm.

A.10 – Pure distilled water at 25°C, 500 rpm and 2.5 vvm

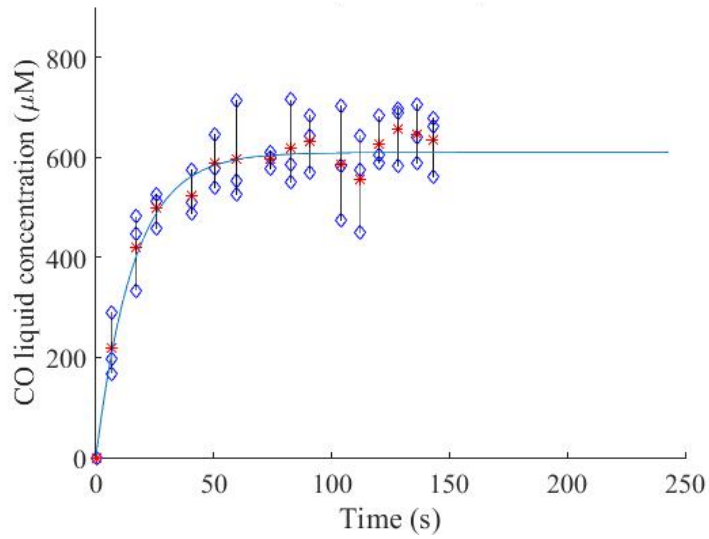


Figure A.19 Model prediction for pure distilled water at 25 °C, 500 rpm and 2.5 vvm.

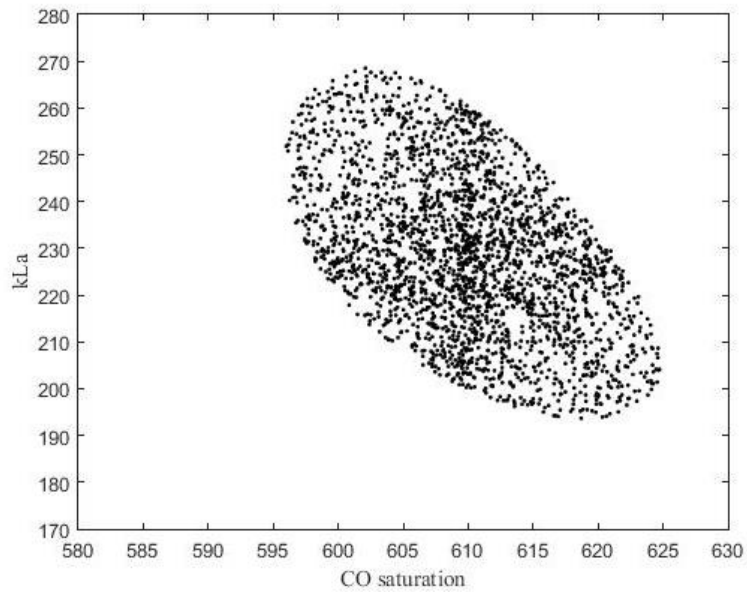


Figure A.20 Confidence region ($\alpha=90\%$) for pure distilled water at 25 °C, 500 rpm and 2.5 vvm.

A.11 – Pure distilled water at 25°C, 500 rpm and 2.7 vvm – triplicate

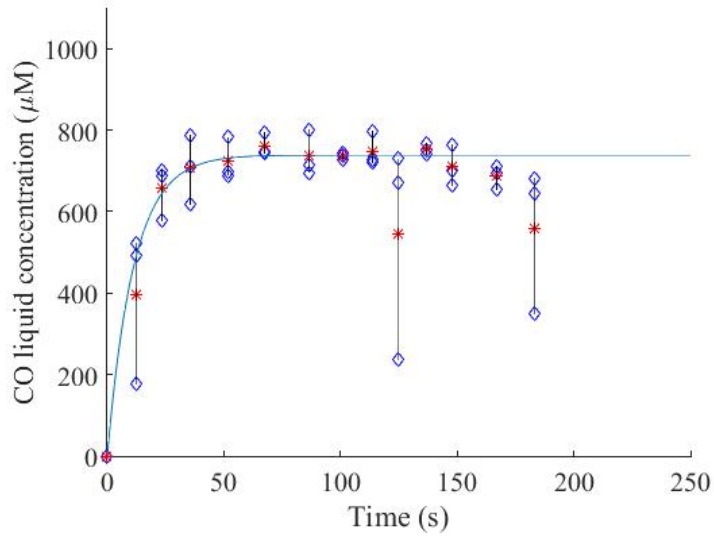


Figure A.21 Model prediction for pure distilled water at 25 °C, 100 rpm and 2.7 vvm, triplicate.

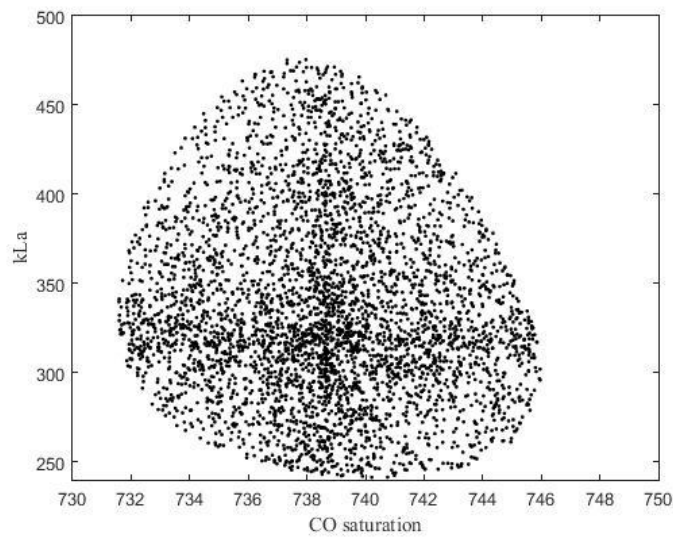


Figure A.22 Confidence region ($\alpha=90\%$) for pure distilled water at 25 °C, 100 rpm and 2.7 vvm, triplicate.

A.12 – Pure distilled water at 25°C, 500 rpm and 2.7 vvm – duplicate

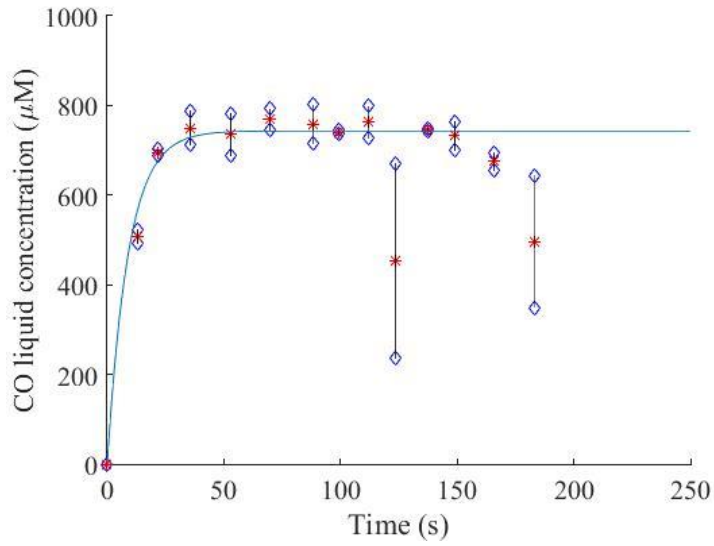


Figure A.23 Model prediction for pure distilled water at 25 °C, 100 rpm and 2.7 vvm, duplicate.

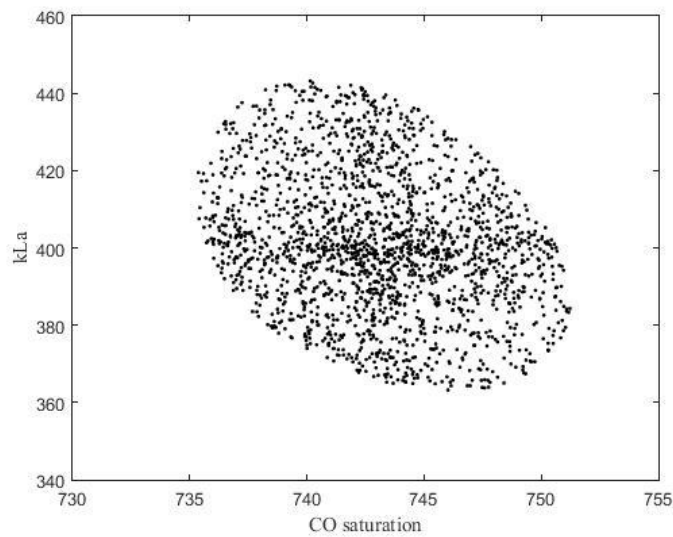


Figure A.24 Confidence region ($\alpha=90\%$) for pure distilled water at 25 °C, 100 rpm and 2.7 vvm, duplicate.

A.13 – Pure distilled water at 37 °C, 300 rpm and 2.7 vvm

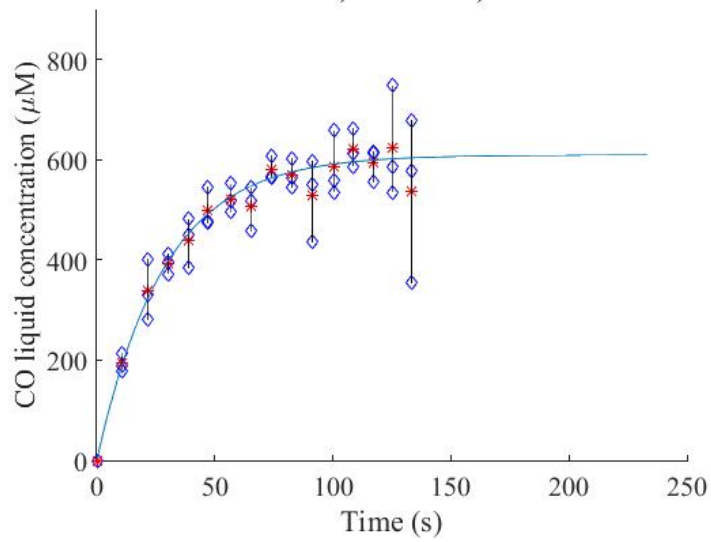


Figure A.25 Model prediction for pure distilled water at 37 °C, 300 rpm and 2.7 vvm.

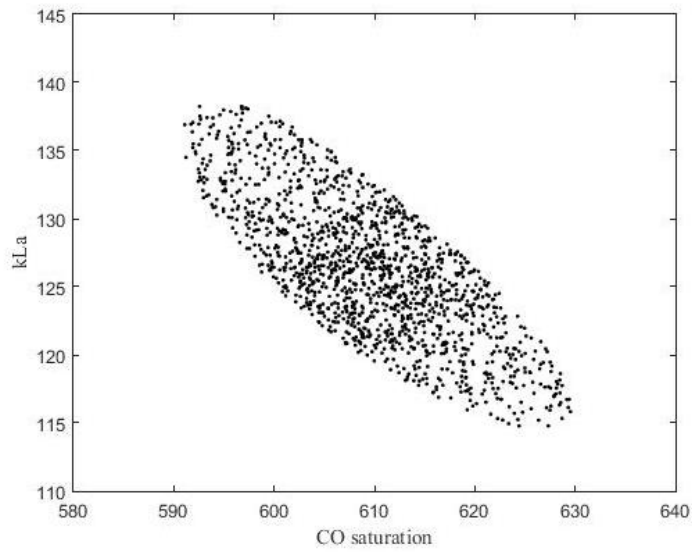


Figure A.26 Confidence region ($\alpha=90\%$) for pure distilled water at 37 °C, 300 rpm and 2.7 vvm.

A.14 – Pure distilled water at 37°C, 500 rpm and 2.7 vvm

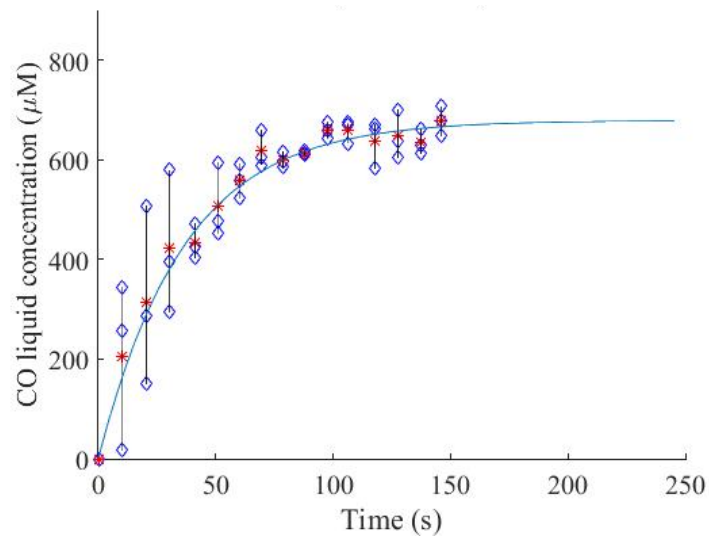


Figure A.27 Model prediction for pure distilled water at 37 °C, 500 rpm and 2.7 vvm.

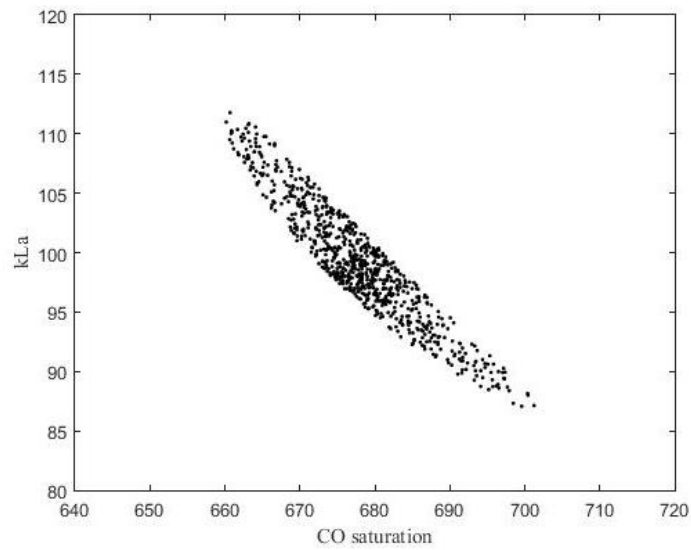


Figure A.28 Confidence region ($\alpha=90\%$) for pure distilled water at 37 °C, 500 rpm and 2.7 vvm.

A.15 – Distilled water and PFC mixture at 25°C, 500 rpm and 2.0 vvm

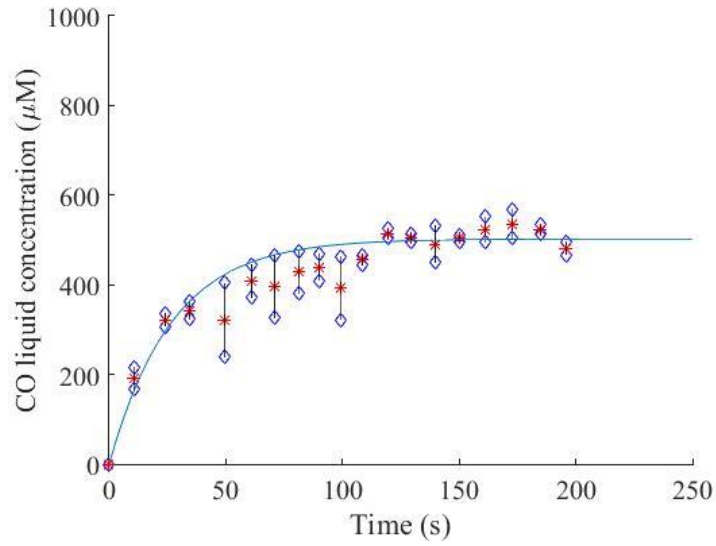


Figure A.29 Model prediction for distilled water and PFC mixture at 25 °C, 500 rpm and 2.0 vvm.

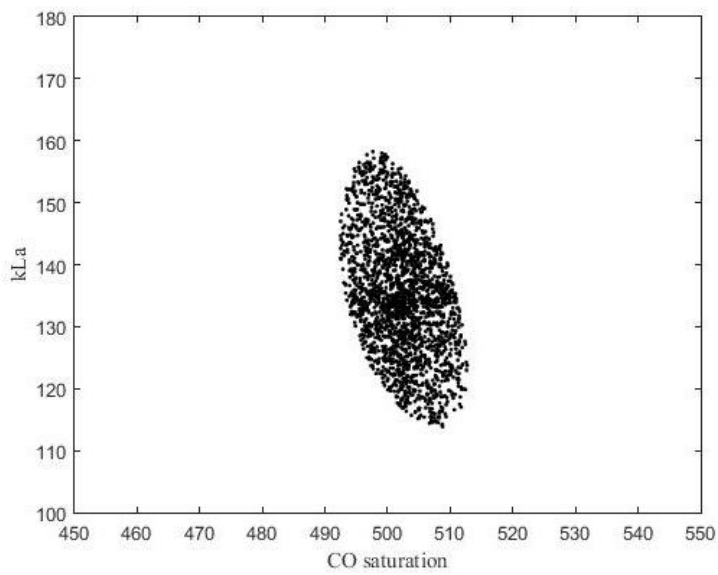


Figure A.30 Confidence region ($\alpha=90\%$) for distilled water and PFC mixture at 25 °C, 500 rpm and 2.0 vvm.

A.16 – Distilled water and PFC mixture at 25°C, 500 rpm and 2.5 vvm

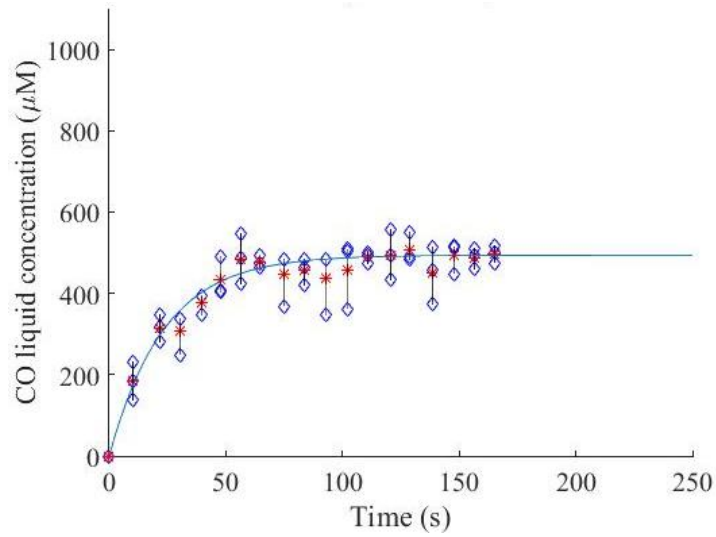


Figure A.31 Model prediction for distilled water and PFC mixture at 25 °C, 500 rpm and 2.5 vvm.

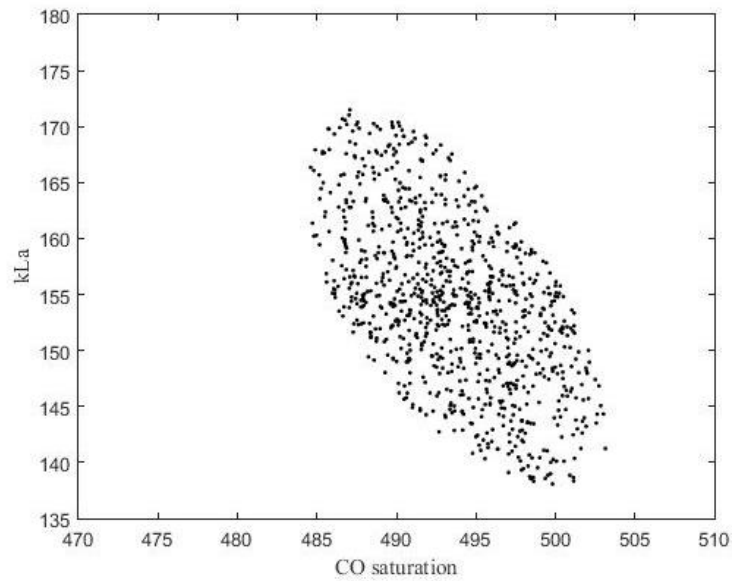


Figure A.32 Confidence region ($\alpha=90\%$) for distilled water and PFC mixture at 25 °C, 500 rpm and 2.5 vvm.

A.17 – Distilled water and PFC mixture at 25°C, 500 rpm and 2.7 vvm

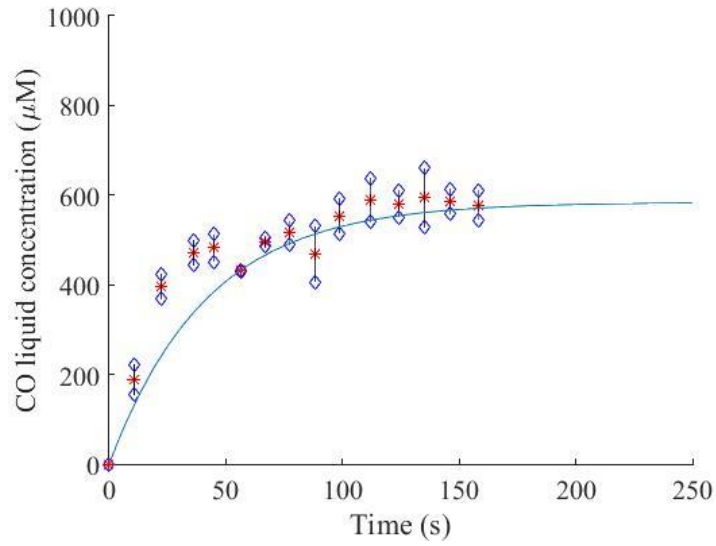


Figure A.33 Model prediction for distilled water and PFC mixture at 25 °C, 500 rpm and 2.7 vvm.

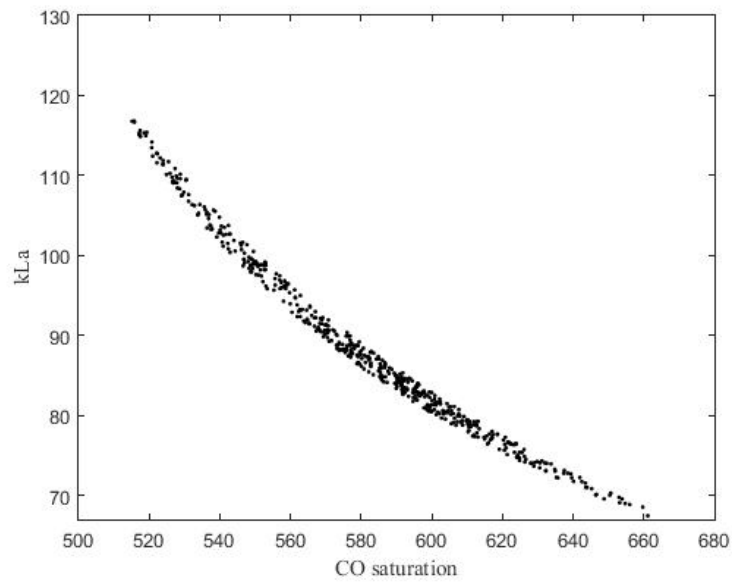


Figure A.34 Confidence region ($\alpha=90\%$) for distilled water and PFC mixture at 25 °C, 500 rpm and 2.7 vvm.

A.18 – Distilled water and PFC mixture at 25°C, 300 rpm and 2.7 vvm

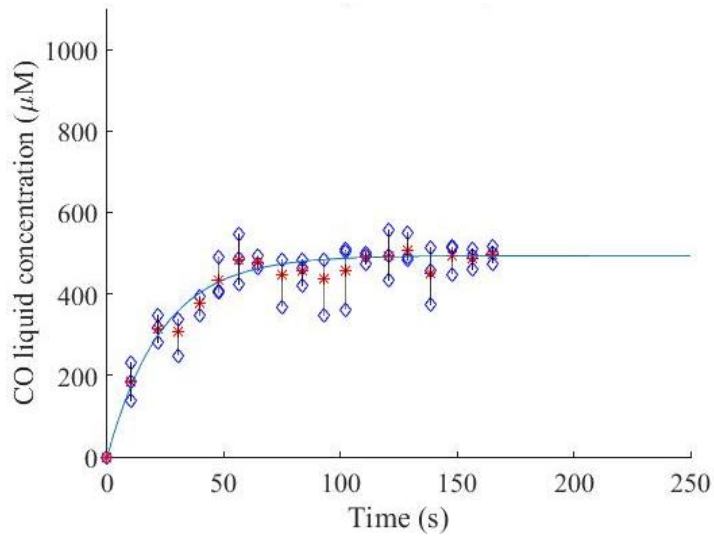


Figure A.35 Model prediction for distilled water and PFC mixture at 25 °C, 300 rpm and 2.7 vvm.

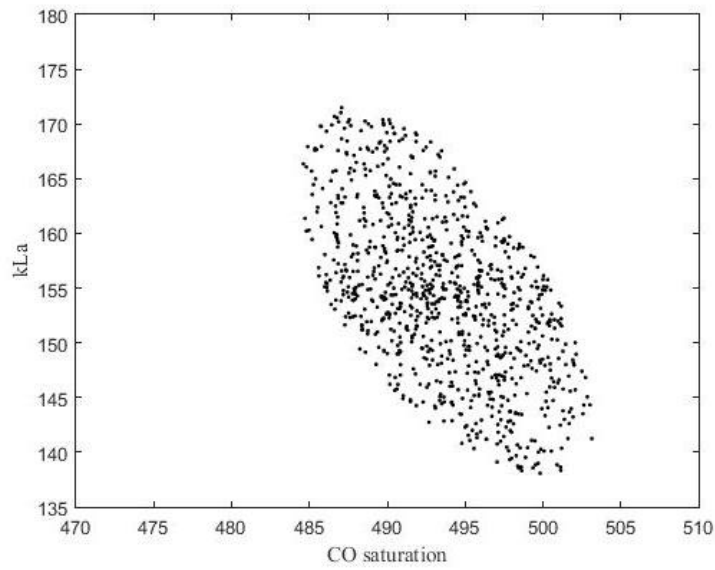


Figure A.36 Confidence region ($\alpha=90\%$) for distilled water and PFC mixture at 25 °C, 300 rpm and 2.7 vvm.

A.19 – Distilled water and Tween® 80 mixture at 25°C, 500 rpm and 2.0 vvm

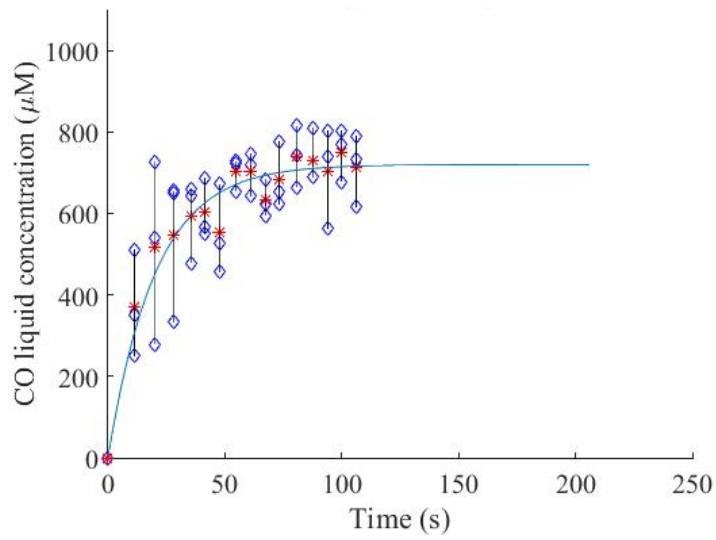


Figure A.37 Model prediction for distilled water and Tween® 80 mixture at 25 °C, 500 rpm and 2.0 vvm.

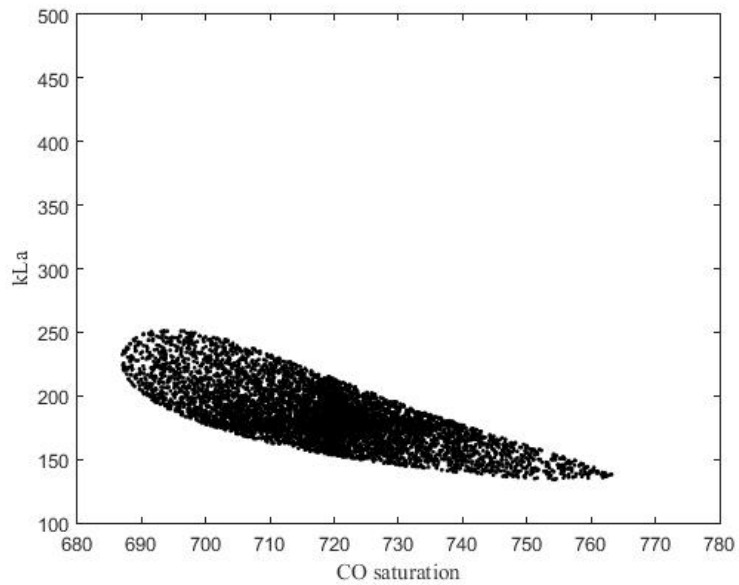


Figure A.38 Confidence region ($\alpha=90\%$) for distilled water and Tween® 80 mixture at 25 °C, 500 rpm and 2.0 vvm.

A.20 – Distilled water and Tween® 80 mixture at 25°C, 500 rpm and 2.5 vvm

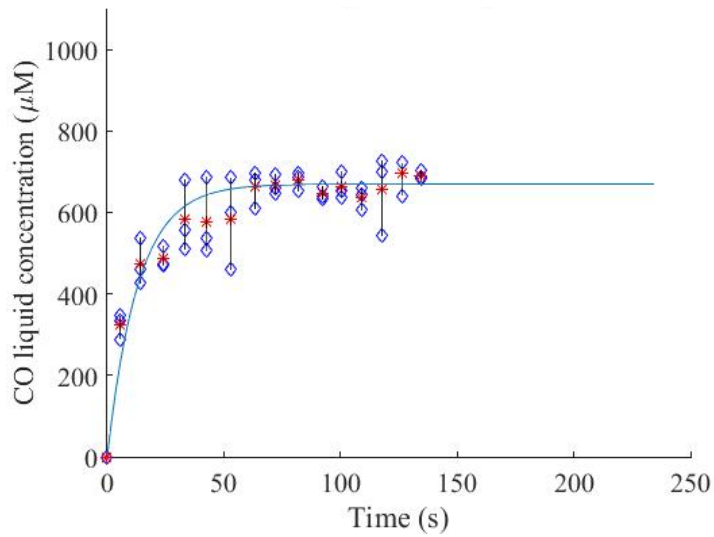


Figure A.39 Model prediction for distilled water and Tween® 80 mixture at 25 °C, 500 rpm and 2.5 vvm.

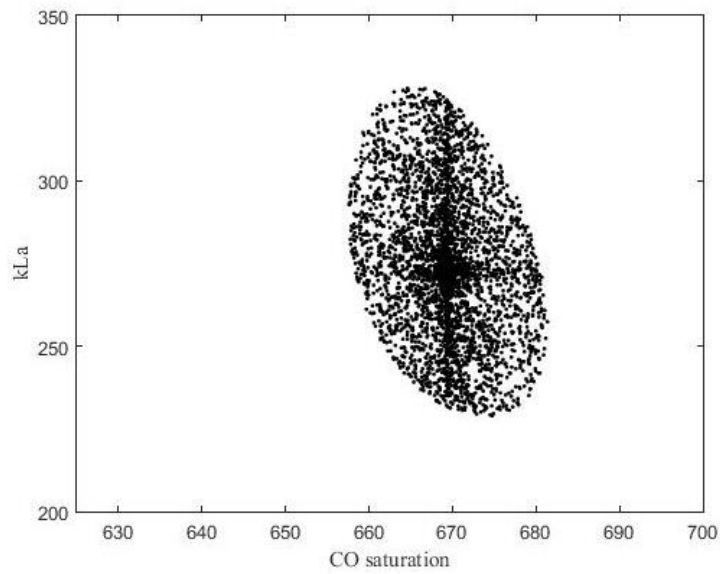


Figure A.40 Confidence region ($\alpha=90\%$) for distilled water and Tween® 80 mixture at 25 °C, 500 rpm and 2.5 vvm.

A.21 – Distilled water and Tween® 80 mixture at 25°C, 500 rpm and 2.7 vvm

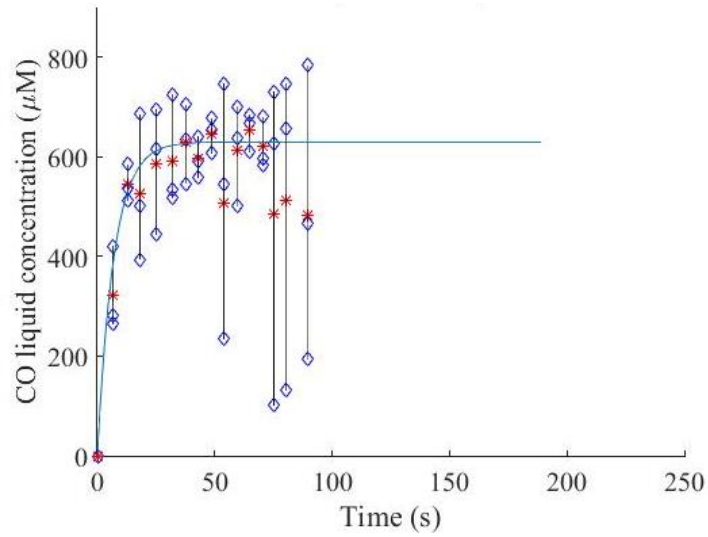


Figure A.41 Model prediction for distilled water and Tween® 80 mixture at 25 °C, 500 rpm and 2.7 vvm.

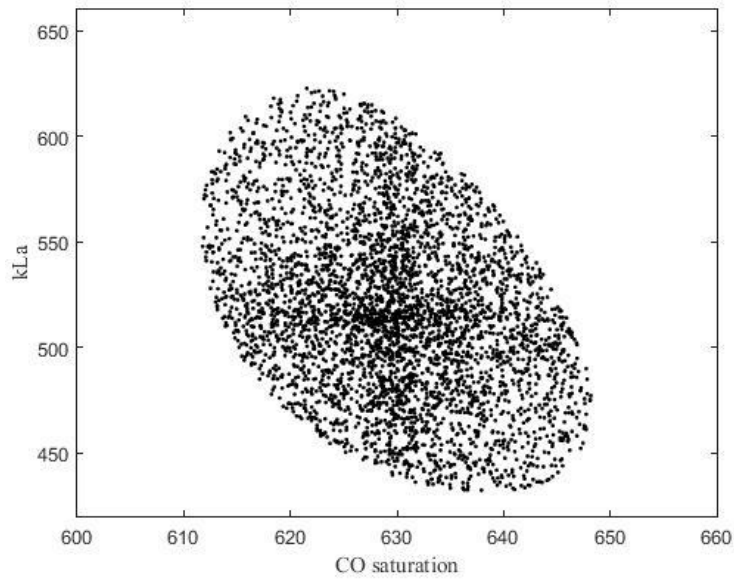


Figure A.42 Confidence region ($\alpha=90\%$) for distilled water and Tween® 80 mixture at 25 °C, 500 rpm and 2.7 vvm.

A.22 – Distilled water and Tween® 80 mixture at 25°C, 300 rpm and 2.7 vvm

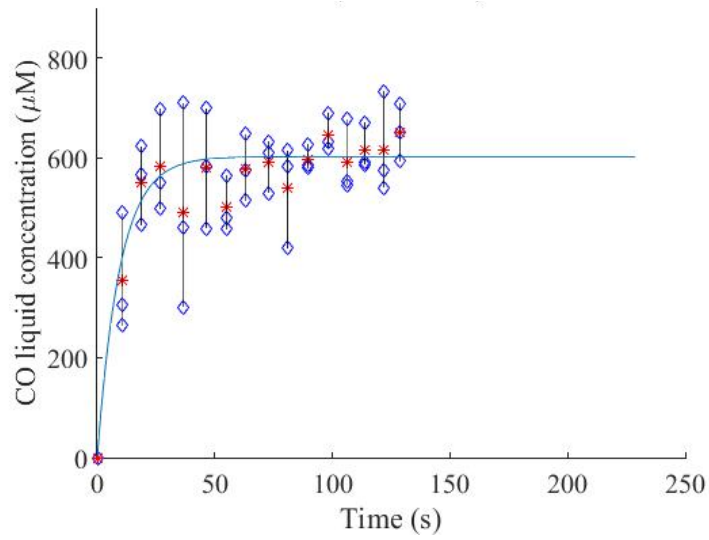


Figure A.43 Model prediction for distilled water and Tween® 80 mixture at 25 °C, 300 rpm and 2.7 vvm.

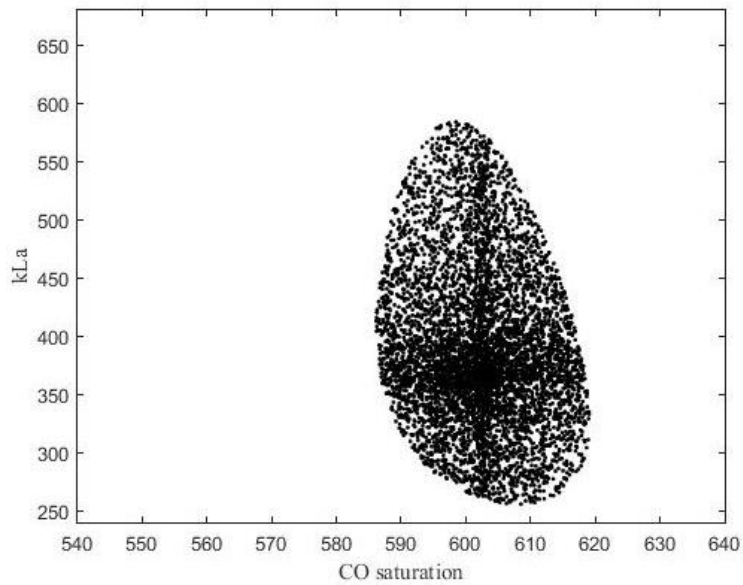


Figure A.44 Confidence region ($\alpha=90\%$) for distilled water and Tween® 80 mixture at 25 °C, 300 rpm and 2.7 vvm.

A.23 – Distilled water, PFC and Tween® 80 mixture at 25°C, 500 rpm and 2.0 vvm

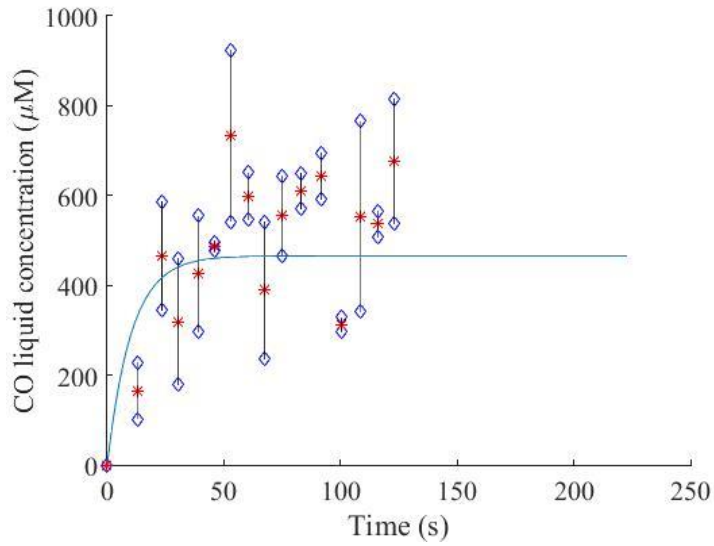


Figure A.45 Model prediction for distilled water, PFC and Tween® 80 mixture at 25 °C, 500 rpm and 2.0 vvm.

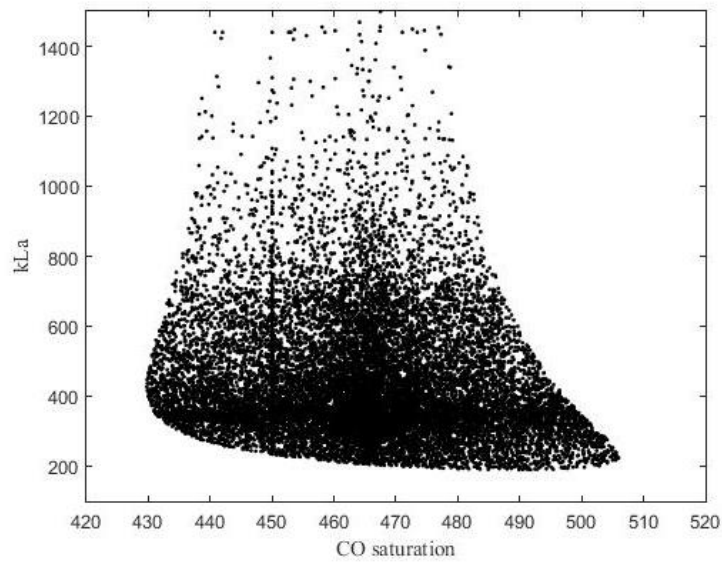


Figure A.46 Confidence region ($\alpha=90\%$) for distilled water, PFC and Tween® 80 mixture at 25 °C, 500 rpm and 2.0 vvm.

A.24 – Distilled water, PFC and Tween® 80 mixture at 25°C, 500 rpm and 2.5 vvm

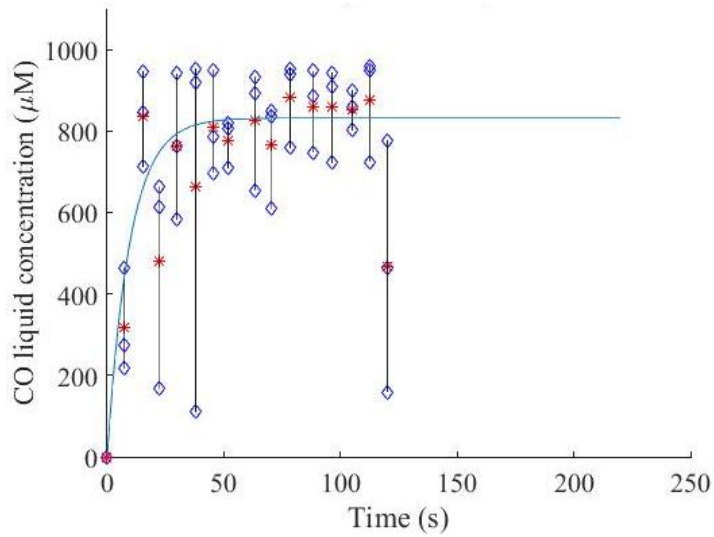


Figure A.47 Model prediction for distilled water, PFC and Tween® 80 mixture at 25 °C, 500 rpm and 2.5 vvm.

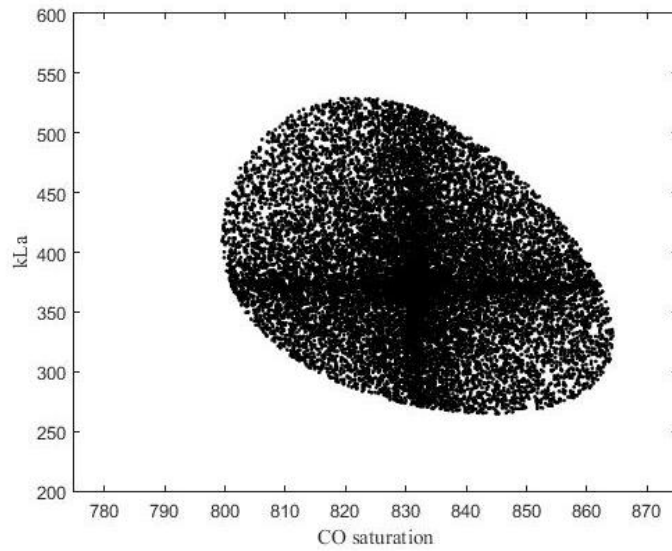


Figure A.48 Confidence region ($\alpha=90\%$) for distilled water, PFC and Tween® 80 mixture at 25 °C, 500 rpm and 2.5 vvm.

A.25 – Distilled water, PFC and Tween® 80 mixture at 25°C, 500 rpm and 2.7 vvm

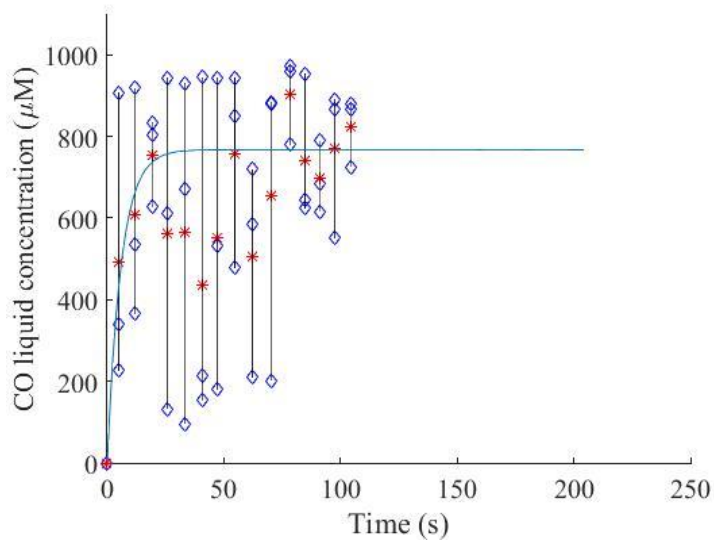


Figure A.49 Model prediction for distilled water, PFC and Tween® 80 mixture at 25 °C, 500 rpm and 2.7 vvm.

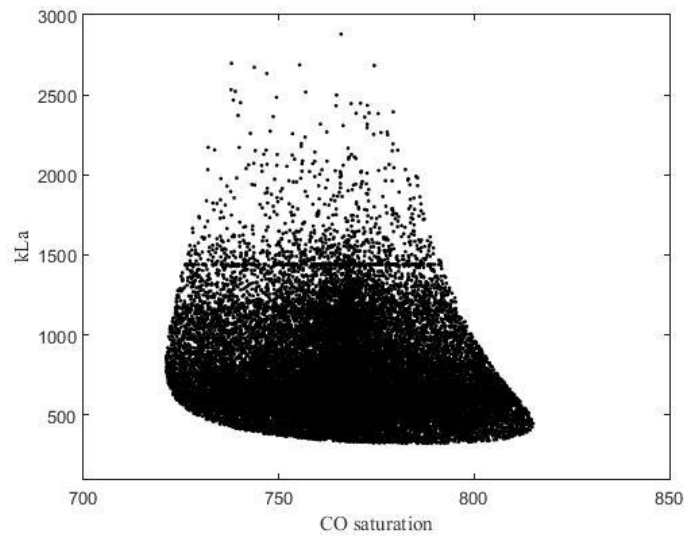


Figure A.50 Confidence region ($\alpha=90\%$) for distilled water, PFC and Tween® 80 mixture at 25 °C, 500 rpm and 2.7 vvm.

A.26 – Distilled water, PFC and Tween® 80 mixture at 25°C, 300 rpm and 2.7 vvm

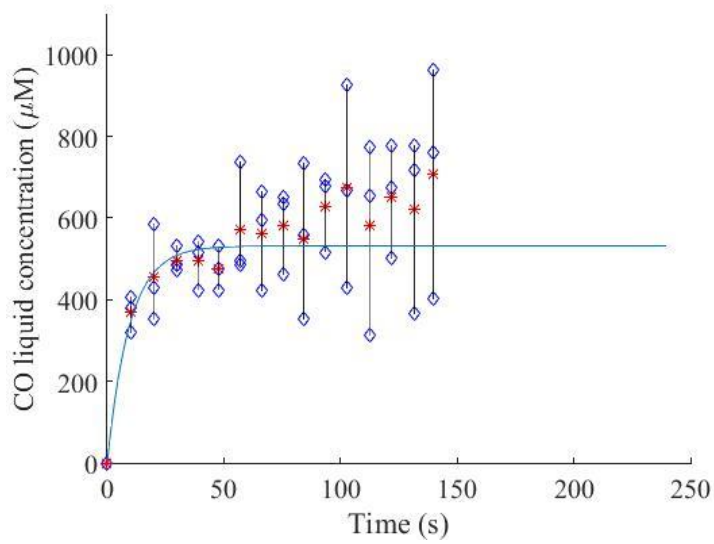


Figure A.51 Model prediction for distilled water, PFC and Tween® 80 mixture at 25 °C, 300 rpm and 2.7 vvm.

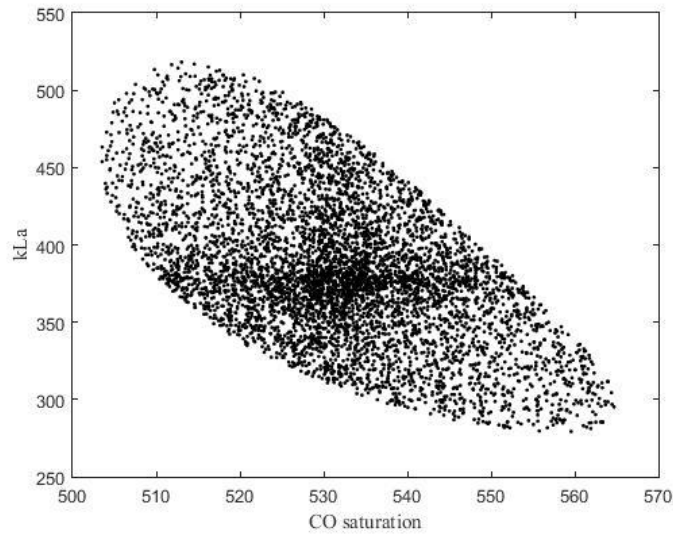


Figure A.52 Confidence region ($\alpha=90\%$) for distilled water, PFC and Tween® 80 mixture at 25 °C, 300 rpm and 2.7 vvm.